Overview of the physics and engineering design of NSTX upgrade

**J.E. Menard[1], S. Gerhardt[1], M. Bell[1], J. Bialek[2], A. Brooks[1],
J. Canik[3], J. Chrzanowski[1], M. Denault[1], L. Dudek[1], D.A. Gates[1],
N. Gorelenkov[1], W. Guttenfelder[1], R. Hatcher[1], J. Hosea[1],
R. Kaita[1], S. Kaye[1], C. Kessel[1], E. Kolemen[1], H. Kugel[1],
R. Maingi[3], M. Mardenfeld[1], D. Mueller[1], B. Nelson[4],
C. Neumeyer[1], M. Ono[1], E. Perry[1], R. Ramakrishnan[1],
R. Raman[4], Y. Ren[1], S. Sabbagh[1], M. Smith[1], V. Soukhanovskii[5],
T. Stevenson[1], R. Strykowsky[1], D. Stutman[6], G. Taylor[1], P. Titus[1],
K. Tresemer[1], K. Tritz[6], M. Viola[1], M. Williams[1], R. Woolley[1],
H. Yuh[7], H. Zhang[1], Y. Zhai[1], A. Zolfaghari[1] and the NSTX Team**

[1] Princeton Plasma Physics Laboratory, Princeton, NJ, USA
[2] Columbia University, New York, NY, USA
[3] Oak Ridge National Laboratory, Oak Ridge, TN, USA
[4] University of Washington, Seattle, WA, USA
[5] Lawrence Livermore National Laboratory, Livermore, CA, USA
[6] Johns Hopkins University, Baltimore, MD, USA
[7] Nova Photonics Incorporated, Princeton, NJ, USA

Abstract

The spherical tokamak (ST) is a leading candidate for a Fusion Nuclear Science Facility (FNSF) due to its compact size and modular configuration. The National Spherical Torus eXperiment (NSTX) is a MA-class ST facility in the US actively developing the physics basis for an ST-based FNSF. In plasma transport research, ST experiments exhibit a strong (nearly inverse) scaling of normalized confinement with collisionality, and if this trend holds at low collisionality, high fusion neutron fluences could be achievable in very compact ST devices. A major motivation for the NSTX Upgrade (NSTX-U) is to span the next factor of 3–6 reduction in collisionality. To achieve this collisionality reduction with equilibrated profiles, NSTX-U will double the toroidal field, plasma current, and NBI heating power and increase the pulse length from 1–1.5 s to 5–8 s. In the area of stability and advanced scenarios, plasmas with higher aspect ratio and elongation, high β_N, and broad current profiles approaching those of an ST-based FNSF have been produced in NSTX using active control of the plasma β and advanced resistive wall mode control. High non-inductive current fractions of 70% have been sustained for many current diffusion times, and the more tangential injection of the 2nd NBI of the Upgrade is projected to increase the NBI current drive by up to a factor of 2 and support 100% non-inductive operation. More tangential NBI injection is also projected to provide non-solenoidal current ramp-up as needed for an ST-based FNSF. In boundary physics, NSTX measures an inverse relationship between the scrape-off layer heat-flux width and plasma current that could unfavourably impact next-step devices. Recently, NSTX has successfully demonstrated substantial heat-flux reduction using a snowflake divertor configuration, and this type of divertor is incorporated in the NSTX-U design. The physics and engineering design supporting NSTX Upgrade is described.

(Some figures may appear in colour only in the online journal)

1. Introduction

The spherical tokamak (ST) [1, 2] is a leading candidate for a Fusion Nuclear Science Facility (FNSF) due to its compact size and modular configuration [3, 4]. The National Spherical Torus eXperiment (NSTX) [5, 6] is a MA-class ST facility in the US actively developing the physics basis for an ST-based FNSF. Access to low collisionality ν^* plasmas in the ST configuration is particularly important to more fully understand transport, stability and non-inductive start-up and sustainment in the ST. In particular, NSTX [7] and MAST [8, 9] observe a strong inverse scaling of normalized confinement with ν^*. An
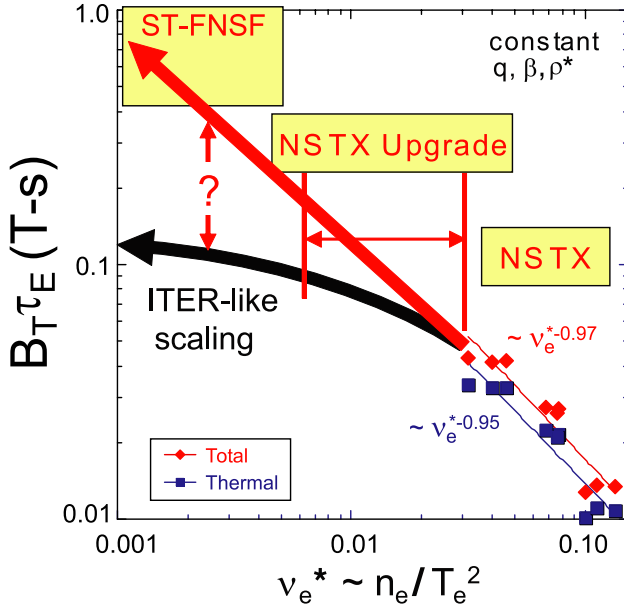
Figure 1. Product of toroidal field (B_T) and energy confinement time (τ_E) versus ν_e^* for NSTX and projections for NSTX Upgrade and ST-FNSF for ITER H-mode and ST confinement scalings.

example of this scaling is shown in figure 1 for NSTX neutral beam heated H-mode experiments in which the plasma q, β and ρ_* were approximately fixed as the electron collisionality ν_e^* was varied by a factor of 3. If the strong favourable scaling of increased dimensionless confinement $\Omega_i\tau_E \propto B_T\tau_E$ with reduced collisionality holds at low collisionality, high fusion neutron fluxes and fluences could be achievable in very compact ST devices only 30–50% larger in major radius than existing ST devices, thereby enabling a reduced size and cost ST-based Fusion Nuclear Science Facility (ST-FNSF). On the other hand, there is evidence from conventional aspect ratio tokamaks operating in H-mode that the collisionality exponent in the dimensionless confinement scaling may depend on the collisionality itself [10]. In particular, from figure 22 of [10], the collisionality exponent is near -0.75 for $\nu_i^* \approx 1$ in C-Mod, -0.25 for $\nu_i^* \approx 0.01$ in JET, and is nearly zero in the ITER IPB98(y,2) H-mode scaling [11, 12] which varies as $B_T\tau_E \propto \rho_*^{-0.70}\beta^{-0.90}\nu_*^{-0.01}q^{-3.0}\epsilon^{0.73}\kappa^{2.3}$. Further, while the range of ν_e^* available from scaling studies on NSTX is limited, the data in figure 1 (not the fit to the data) may be consistent with a weakening dependence of $B_T\tau_E$ on ν_e^* as ν_e^* is reduced. To more definitively determine the scaling of confinement with collisionality in regimes representative of next-step STs, an additional factor of 3–6 reduction in ν^* is needed to overlap with the upper-end of ν^* values for an ST-FNSF, and access to this reduced collisionality is a major motivation for the Upgrade of NSTX. It should be noted that the strong β dependence of the ITER H-mode confinement scaling is not observed in several single-machine and inter-machine confinement scaling studies [13, 14] but has been observed in other dedicated experiments [15] and may depend on plasma shaping. Given the strong dependence of the ITER confinement scaling on elongation κ and potentially uncertain dependence on β, continued access to high β and κ will also continue to be important to assess ST confinement dependence on these parameters.

For high-power ST H-mode plasmas, the electron and ion thermal diffusivities are found to have different scaling dependencies [16]. In particular, the ion confinement is typically near neoclassical values in the outer half of the plasma minor radius and has a nearly linear plasma current dependence. In contrast, the electron confinement is anomalous and has a nearly linear toroidal field dependence. Understanding electron energy confinement is far more challenging to understand and project than ion confinement as several instabilities potentially responsible for anomalous/turbulent electron thermal transport have been identified. The modes studied for NSTX include electron temperature gradient (ETG) modes [17–21], global Alfvén eigenmodes (GAE) [22–24], and micro-tearing modes [25–28]. Unraveling the simultaneous effects of these instabilities is a major research goal of NSTX Upgrade by extending the achievable collisionality, toroidal field and plasma current.

Isolating the effects of the different instabilities causing anomalous electron transport will require improved understanding and expanded variation of the drives for the instabilities. For example, linear and nonlinear simulations based on NSTX discharges show that micro-tearing growth rates and transport increase with increasing collisionality, β, s/q (for $s > 0$), and possibly even Z_{eff} [28–30]. Figure 2 shows recent nonlinear gyrokinetic simulations of micro-tearing-induced electron transport [28] that have shown reasonable agreement with experimentally inferred electron thermal diffusivities for the limited range of shots and minor radii tested and ignoring $E \times B$ shear. It should be noted that the inclusion of experimental values of $E \times B$ shear can reduce or suppress the predicted micro-tearing transport, but modest increases in temperature gradient can recover experimentally relevant transport. These simulations indicate that micro-tearing-induced electron transport should continue to scale nearly linearly with collisionality over approximately one order of magnitude in collisionality as the collisionality is reduced below present NSTX values.

In contrast, ETG turbulence is insensitive to collisionality [31], is often weakly dependent on or stabilized with increasing β [32, 33], and tends to be stabilized by increasing s/q (for $s > 0$) and Z_{eff} [34]. Both ETG and micro-tearing can be stabilized with sufficiently strong density gradient [21, 29, 34], although TEM can then become unstable (or even KBM modes at higher q towards outer radii, as the KBM drive corresponds roughly to the MHD alpha parameter $\alpha_{MHD} = q^2 R\nabla\beta$). Core drift wave instabilities are also susceptible to suppression via strong flow shear when the $E \times B$ shearing rate approaches the relevant maximum linear growth rate [30, 35–39]. Expanding the achievable range of I_P, B_T, P_{NBI}, and the flexibility of the neutral beam tangency radius will allow NSTX-U to test core transport theory and better distinguish between ETG and micro-tearing-induced transport by varying collisionality and β over a broader range and by more directly influencing profile variations in s, q and flow shear.

For GAE-induced electron transport, increased magnetic field is predicted to have a significant impact on GAE mode stability and the spectrum of unstable modes. For example, the driving factor for the GAE is dominated by beam fast-ions with $k_\perp\rho_{\perp b} = 2$–$4$ where $k_\perp$ is the GAE perpendicular wavenumber
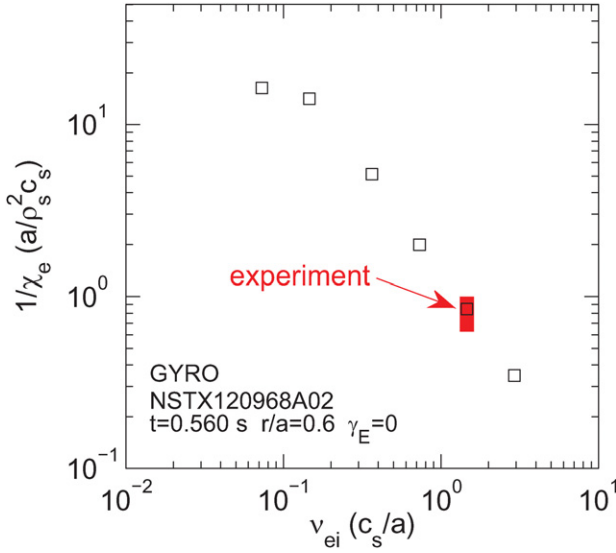
Figure 2. Nonlinear gyrokinetic simulations of the normalized inverse anomalous electron thermal diffusivity χ_e versus normalized collisionality for microtearing instabilities in NSTX.

and $\rho_{\perp b}$ is the beam fast-ion perpendicular Larmor radius $v_{\perp b}/\omega_{cb}$ [22]. Further, the trapped particle resonance condition is only met for those particles with $v_{||}/v_{Alfvén} > (1 + \omega_{cb}/\omega)$ where $\omega \approx k_{||}v_{Alfvén}$ [22]. At fixed density, $v_{Alfvén} \propto B$, and since the beam injection energy will not be increased in NSTX Upgrade, if the magnetic field is significantly increased, fewer beam particles will contribute to the drive which will decrease the mode growth rates and/or the number of unstable modes. The predicted GAE-induced electron thermal diffusivity is a strong function of the normalized GAE field amplitude $\delta B_r/B_0 \approx i\alpha k_\theta R_0$ and varies as α^3 at low amplitude to α^6 at larger amplitude possibly due to higher-order nonlinear resonances contributing to the diffusion [24]. Thus, the ability to increase B and decrease $k_\perp \rho_{\perp b}$ and $v_{fast-ion}/v_{Alfvén}$ could result in a significant reduction of the GAE-induced electron transport which would assist in understanding the relative importance of GAE, ETG and micto-tearing modes for causing electron transport.

Beyond impacting turbulent transport, reduced collisionality could also impact toroidal rotation damping [40–42], RWM stability [42, 43], error-field correction [44, 45], pedestal stability [46] and many other physics areas. To improve the understanding of ST confinement, stability, and other physics, a major upgrade to NSTX is planned to span the next factor of 3–6 reduction in collisionality while also extending regimes and capabilities including fully non-inductive current ramp-up and sustainment and the development of mitigation techniques for high heat flux. The physics and engineering design of NSTX Upgrade is described in detail in section 2 and is summarized in section 3.

2. Physics requirements and engineering design

2.1. Physics requirements

2.1.1. Overview. As described in section 1, access to reduced collisionality is a major research goal of NSTX Upgrade. Reduced normalized collisionality (ratio of collision

frequency to bounce frequency) $\nu^* \propto q R n/T^2 \epsilon^{3/2}$ [47] requires increased temperature T and/or reduced density n for fixed plasma major radius R, inverse aspect ratio $\epsilon = 1/A$ and safety factor q. Combining Troyon scaling [48–51] for the β limit: $nT \propto \beta_N I_P B/a$ with the Greenwald density limit [52, 53] scaling: $n \propto I_P/a^2$ implies $T \propto \beta_N a B/f_{GW}$ where β_N is the normalized β, a is the minor radius, B is the magnetic field strength and the Greenwald density fraction $f_{GW} \equiv \bar{n}_e(10^{20} \, \text{m}^{-3})\pi a^2/I_P(\text{MA})$. Thus, at fixed f_{GW} and β_N, increased T requires increased B and is the major motivation for increased magnetic field strength in NSTX Upgrade. Using these definitions and assuming fixed geometry, it follows that $\nu^* \propto f_{GW}^3/\beta_N^2 B_T$. Here the vacuum toroidal field B_T at the plasma geometric centre R_0 is used for B, $\beta_T \equiv 2\mu_0\langle p\rangle/B_T^2$, and $\beta_N \equiv \beta_T a B_T/I_P$ with units of $\%\text{m T MA}^{-1}$. This scaling for ν^* highlights the importance of access to low f_{GW} and high β_N and B_T for achieving low collisionality. To access similar safety factor q at higher B_T, I_P should be scaled linearly with B_T, sufficient auxiliary heating power P_{heat} should be provided to access the desired β_N and the required P_{heat} will depend on the confinement scaling.

The research goals of NSTX Upgrade extend beyond accessing reduced collisionality. In particular, it is also important to address non-inductive ramp-up and sustainment, the establishment of equilibrated integrated scenarios, ST confinement and stability scaling and understanding, high-power and particle exhaust understanding and mitigation and investigations of advanced operating scenarios, respectively. Scoping studies of NSTX-U operating scenarios are important for identifying and meeting the Upgrade performance requirements to achieve these physics research goals. To satisfy these performance requirements, five representative NSTX-U operating scenarios are investigated and motivate the Upgrade design: (1) 100% non-inductive current drive, (2) partially inductively driven long pulse, (3) high/maximum plasma current, (4) high current plus high heating power and divertor heat flux and (5) high bootstrap fraction with high confinement. Table 1 summarizes parameters of interest for these five NSTX-U scenarios projected from NSTX data using 0D scaling analysis supported by TRANSP [54] simulations. Table 1 also includes comparisons of TRANSP analysis for three NSTX experimental discharges to corresponding 0D scalings for benchmarking purposes, and also includes parameters for a computed NSTX reference scenario at two densities. A more comprehensive exploration of NSTX Upgrade equilibrium scenarios calculated using free-boundary TRANSP simulations can be found in [55].

2.1.2. Scenario projection methodology. Three representative NSTX discharges are analysed using TRANSP to form a 0D scaling model and to define a calculated NSTX reference scenario at fixed current, field, shape, NBI heating power and confinement scaling (ITER IPB98(y,2)) but with varied f_{GW}. The NSTX reference scenario is defined in order to provide a single reference condition from which to project to NSTX Upgrade performance for different confinement scaling models and f_{GW} values. The 0D scaling model used here is also consistent with confinement scaling results for NSTX advanced scenarios [56]. The NSTX NBI-heated H-mode discharges

Table 1. (Left) Comparison between NSTX 0D scaling model and TRANSP analysis of representative NSTX experimental discharges, (middle white columns) parameters for NSTX Reference scenario at two density values, and (right) projected parameters for NSTX Upgrade scenarios. Red numbers are specified input parameters, numbers coloured black or bold blue are computed from the scaling model (or from TRANSP), and the bold blue parameters represent important ratios or fractions.

	NSTX 0D scaling vs TRANSP								NSTX Upgrade Scenarios													
Device and scenario	NSTX 0.7MA f_{GW}=0.6, H_{98}=1		NSTX 0.9MA f_{GW}=0.95, H_{98}=1		NSTX 1.3MA f_{GW}=0.73, H_{98}=1		NSTX Reference		NSTX-U 100% NICD		NSTX-U Long-pulse		NSTX-U Max I_P		NSTX-U Max I_P, P_{heat}		NSTX-U 100% NICD		NSTX-U Max I_P		NSTX-U High f_{BS}	
Confinement scaling	0D scaling model	TRANSP 135440 S04	0D scaling model	TRANSP 133078 A01	0D scaling model	TRANSP 132911 A01	0D scaling model		H98y2		H98y2		H98y2		H98y2		ST		ST		ST	
Greenwald fraction	0.61	0.61	0.95	0.95	0.73	0.73	0.5	1.0	0.5	1.0	0.5	1.0	0.5	1.0	0.5	1.0	0.5	1.0	0.5	1.0	0.5	1.0
I_P (MA)	0.71	0.71	0.92	0.92	1.30	1.30	1.0	1.0	1.10	1.02	0.90	0.90	2.00	2.00	2.00	2.00	1.50	1.46	2.00	2.00	1.11	1.16
B_T (Tesla)	0.42	0.42	0.44	0.44	0.49	0.49	0.45	0.45	1.00	1.00	0.75	0.75	1.00	1.00	1.00	1.00	1.00	1.00	1.00	1.00	1.00	1.00
Aspect ratio A	1.49	1.49	1.50	1.50	1.45	1.45	1.5	1.5	1.7	1.7	1.7	1.7	1.7	1.7	1.7	1.7	1.7	1.7	1.7	1.7	1.7	1.7
R_0 (m)	0.83	0.83	0.86	0.86	0.86	0.86	0.86	0.86	0.93	0.93	0.93	0.93	0.93	0.93	0.93	0.93	0.93	0.93	0.93	0.93	0.93	0.93
Elongation κ	2.60	2.60	2.45	2.45	2.55	2.55	2.60	2.60	2.75	2.75	2.75	2.75	2.75	2.75	2.75	2.75	2.75	2.75	2.75	2.75	2.75	2.75
P_{NBI} (MW)	4.90	4.90	5.90	5.90	6.30	6.30	6.0	6.0	10.0	10.0	5.0	5.0	10.0	10.0	15.0	15.0	6.0	6.0	6.0	6.0	2.0	2.0
P_{RF} (MW)	0.00	0.00	0.00	0.00	0.00	0.00	0.0	0.0	0.0	0.0	0.0	0.0	0.0	0.0	4.0	4.0	0.0	0.0	0.0	0.0	2.0	2.0
P_{ind} (MW)	0.15	0.16	0.25	0.29	0.47	0.48	0.15	0.24	0.00	0.00	0.05	0.08	0.23	0.37	0.10	0.18	0.00	0.00	0.10	0.21	0.00	0.00
P_{heat} (MW)	5.05	5.06	6.15	6.19	6.77	6.78	6.15	6.24	10.0	10.0	5.05	5.08	10.2	10.4	19.1	19.2	6.00	6.00	6.10	6.21	4.00	4.00
n_e-bar (10^{20} m^{-3})	0.44	0.44	0.85	0.85	0.85	0.85	0.52	1.03	0.54	1.00	0.44	0.88	0.98	1.96	0.98	1.96	0.73	1.43	0.98	1.96	0.59	1.23
Volume avg. T_e (keV)	0.62	0.61	0.62	0.57	0.84	0.85	0.96	0.67	1.50	1.01	1.09	0.75	1.80	1.25	2.19	1.51	2.63	1.59	2.49	1.51	2.25	1.34
Volume avg. T_i (keV)	0.68	0.67	0.64	0.59	0.90	0.90	1.08	0.68	1.68	1.03	1.22	0.77	2.02	1.27	2.45	1.54	2.94	1.62	2.79	1.54	2.52	1.37
T_i peaking factor	1.47	1.46	1.47	1.55	1.47	1.38	1.47	1.47	1.47	1.47	1.47	1.47	1.47	1.47	1.47	1.47	1.47	1.47	1.47	1.47	1.47	1.47
T_e peaking factor	1.44	1.42	1.44	1.46	1.44	1.43	1.44	1.44	1.44	1.44	1.44	1.44	1.44	1.44	1.44	1.44	1.44	1.44	1.44	1.44	1.44	1.44
n_e peaking factor	1.35	1.26	1.35	1.48	1.35	1.31	1.35	1.35	1.35	1.35	1.35	1.35	1.35	1.35	1.35	1.35	1.35	1.35	1.35	1.35	1.35	1.35
$p_{thermal}$ peaking factor	1.83	1.70	1.83	2.08	1.83	1.72	1.83	1.83	1.83	1.83	1.83	1.83	1.83	1.83	1.83	1.83	1.83	1.83	1.83	1.83	1.83	1.83
p_{fast} peaking factor	4.57	4.82	4.57	4.40	4.57	4.49	4.57	4.57	4.57	4.57	4.57	4.57	4.57	4.57	4.57	4.57	4.57	4.57	4.57	4.57	4.57	4.57
p_{total} peaking factor	2.69	2.65	2.20	2.40	2.22	2.17	2.93	2.25	3.18	2.49	3.02	2.30	2.43	2.03	2.72	2.15	2.41	2.05	2.19	1.95	2.18	1.93
Normalized toroidal rotation	1.14	1.14	0.62	0.59	1.53	1.53	1.00	1.00	2.32	2.29	0.99	0.99	2.55	2.55	4.22	4.21	1.85	1.72	1.80	1.68	0.48	0.45
I_P flat-top time (s)	1.32	1.32	1.00	1.00	0.39	0.39	0.7	0.7	5.0	5.0	10.0	10.0	5.0	5.0	0.3	0.3	5.0	5.0	5.0	5.0	5.0	5.0
$\tau_{current\text{-}redistribution}$ (s)	0.26	0.26	0.28	0.24	0.47	0.48	0.51	0.29	1.04	0.57	0.65	0.37	1.37	0.79	1.83	1.05	2.41	1.13	2.23	1.05	1.76	0.81
# redistribution times	**5.1**	**5.1**	**3.5**	**4.1**	**0.8**	**0.8**	**1.4**	**2.4**	**4.8**	**8.7**	**15**	**27**	**3.6**	**6.3**	**0.2**	**0.3**	**2.1**	**4.4**	**2.2**	**4.8**	**2.8**	**6.2**
Stored energy (MJ)	0.19	0.19	0.28	0.27	0.39	0.41	0.36	0.33	0.68	0.54	0.36	0.33	0.96	1.08	1.35	1.37	1.04	1.00	1.20	1.26	0.65	0.70
β_N (%mT MA^{-1})	4.8	4.9	5.5	5.3	4.9	5.1	6.0	5.6	5.4	4.6	4.7	4.2	4.2	4.7	5.9	5.9	6.0	6.0	5.2	5.5	4.9	5.0
β_T (%)	14.5	14.9	20.1	19.7	22.0	22.9	21.6	20.2	10.3	8.2	9.8	8.8	14.7	16.4	20.5	20.8	15.8	15.3	18.3	19.1	9.9	10.7
q^*	4.3	4.3	3.2	3.2	2.9	2.9	3.5	3.5	6.8	7.3	6.2	6.2	3.7	3.7	3.7	3.7	5.0	5.1	3.7	3.7	6.2	5.9
Fast-ion β fraction	0.31	0.30	0.14	0.14	0.14	0.16	0.40	0.15	0.49	0.24	0.43	0.17	0.22	0.07	0.32	0.12	0.21	0.08	0.13	0.04	0.13	0.04
$v_{fast\text{-}ion}$ / $v_{Alfvén}$	3.0	3.0	4.0	4.0	3.7	3.7	2.6	3.7	1.3	1.8	1.6	2.2	1.8	2.5	2.0	2.8	1.5	2.1	1.8	2.5	1.4	2.0
$V_e^*[\times10^2]$ (q=2, ε=A^{-1})	6.4	6.5	10.7	13.0	7.7	7.4	2.8	11.6	1.4	5.7	2.1	9.0	1.7	7.3	1.2	5.0	0.6	3.3	0.9	5.0	0.7	4.2
$V_e^*[\times10^2]$ (q=q^*, ε=A^{-1})	13.6	13.8	17.0	20.7	11.1	10.7	4.8	20.1	4.7	20.9	6.7	28.0	3.3	13.6	2.2	9.3	1.5	8.5	1.7	9.4	2.2	12.6
Bootstrap fraction f_{BS}	0.44	0.41	0.48	0.50	0.38	0.37	0.40	0.53	0.61	0.85	0.55	0.72	0.41	0.54	0.49	0.65	0.79	0.94	0.56	0.65	0.89	0.97
NBI CD fraction $f_{NBI\text{-}CD}$	0.16	0.17	0.07	0.06	0.08	0.07	0.17	0.06	0.38	0.15	0.21	0.07	0.14	0.05	0.25	0.09	0.21	0.07	0.11	0.03	0.10	0.03
Non-inductive fraction f_{NICD}	**0.60**	**0.59**	**0.55**	**0.56**	**0.47**	**0.44**	**0.57**	**0.59**	**0.99**	**1.00**	**0.75**	**0.79**	**0.54**	**0.59**	**0.74**	**0.74**	**1.00**	**1.00**	**0.68**	**0.68**	**1.00**	**1.00**
I_P ramp-up time (s)	0.16	0.15	0.20	0.21	0.29	0.34	0.2	0.2	0.55	0.51	0.45	0.45	1.00	1.00	1.00	1.00	0.75	0.73	1.00	1.00	0.56	0.58
I_P ramp-down time (s)	0.08	0.04	0.10	0.02	0.14	0.09	0.1	0.1	0.28	0.26	0.23	0.23	0.50	0.50	0.50	0.50	0.38	0.37	0.50	0.50	0.28	0.29
Total I_P duration (s)	1.56	1.51	1.31	1.23	0.82	0.82	1.0	1.0	5.8	5.8	10.7	10.7	6.5	6.5	1.8	1.8	6.1	6.1	6.5	6.5	5.8	5.9
Max. TF flat-top time (s)	1.60	1.60	1.48	1.48	1.17	1.17	1.1	1.1	6.6	6.6	11.7	11.7	6.6	6.6	6.6	6.6	6.6	6.6	6.6	6.6	6.6	6.6
Fraction TF flat-top used	**0.97**	**0.94**	**0.88**	**0.83**	**0.70**	**0.70**	**0.96**	**0.96**	**0.88**	**0.87**	**0.91**	**0.91**	**0.98**	**0.98**	**0.27**	**0.27**	**0.93**	**0.92**	**0.98**	**0.98**	**0.88**	**0.89**
Total OH flux available (Wb)	0.75	0.75	0.75	0.75	0.75	0.75	0.75	0.75	2.10	2.10	2.10	2.10	2.10	2.10	2.10	2.10	2.10	2.10	2.10	2.10	2.10	2.10
I_P ramp-up flux (Wb)	0.25	0.25	0.34	0.34	0.48	0.48	0.37	0.37	0.44	0.41	0.36	0.36	0.80	0.80	0.80	0.80	0.60	0.58	0.80	0.80	0.44	0.46
Surface voltage (V)	0.21	0.23	0.28	0.31	0.36	0.37	0.15	0.24	0.00	0.00	0.06	0.09	0.12	0.18	0.05	0.09	0.00	0.00	0.05	0.11	0.00	0.00
Total flat-top flux (Wb)	0.50	0.50	0.41	0.41	0.27	0.27	0.38	0.38	1.66	1.69	1.74	1.74	1.30	1.30	1.30	1.30	1.50	1.52	1.30	1.30	1.66	1.64
Flat-top flux used (Wb)	0.28	0.32	0.28	0.31	0.14	0.14	0.10	0.17	0.0	0.0	0.60	0.88	0.58	0.92	0.01	0.03	0.0	0.0	0.26	0.53	0.00	0.00
Fraction OH flux used	**0.72**	**0.76**	**0.82**	**0.87**	**0.83**	**0.83**	**0.63**	**0.72**	**0.21**	**0.19**	**0.46**	**0.59**	**0.66**	**0.82**	**0.39**	**0.39**	**0.28**	**0.28**	**0.50**	**0.63**	**0.21**	**0.22**
Power fraction to divertor	0.50	0.50	0.50	0.50	0.50	0.50	0.5	0.5	0.50	0.50	0.50	0.50	0.50	0.50	0.50	0.50	0.50	0.50	0.50	0.50	0.50	0.50
$R_{strike\text{-}point}$ (m)	0.40	0.40	0.40	0.40	0.40	0.40	0.40	0.40	0.50	0.50	0.50	0.50	0.50	0.50	0.50	0.50	0.50	0.50	0.50	0.50	0.50	0.50
SOL heat-flux width (mm)	15.9	15.9	10.5	10.5	6.0	6.0	9.2	9.2	7.9	8.9	10.9	10.9	3.0	3.0	3.0	3.0	4.8	5.0	3.0	3.0	7.8	7.3
Poloidal flux expansion	22	22	22	22	22	22	22	22	22	22	22	22	62	62	62	62	22	22	38	38	22	22
Peak heat flux (MW m^{-2})	2.9	2.9	5.3	5.3	10.1	10.1			9.1	8.1	3.4	3.4	8.7	8.8	16.2	16.2	9.0	8.6	8.4	8.6	3.7	4.0
Time to T_{PFC} = 1200 °C (s)	61	60	18	18	4.9	4.9	13.7	13.3	6.1	7.6	44	44	6.7	6.5	1.9	1.9	6.1	6.7	7.1	6.8	36	31
Fraction of T_{PFC} limit	**0.03**	**0.02**	**0.07**	**0.07**	**0.17**	**0.17**	**0.08**	**0.08**	**0.96**	**0.76**	**0.24**	**0.24**	**0.97**	**1.00**	**0.94**	**0.95**	**1.00**	**0.91**	**0.92**	**0.96**	**0.16**	**0.19**

used here all have an ITER IPB98(y,2) confinement enhancement factor $H_{98} = 1.0$, span a range of f_{GW} from 0.6 to 0.95 and have $I_P = 0.7$–1.3 MA, $A = 1.45$–1.5 and $\kappa = 2.45$–2.6. Profile peaking factors for the temperature, density and pressure (thermal and fast) in the 0D model are taken from the average values from the three discharges, and the total pressure profile peaking factor includes the contribution from the model-estimated fast-ion pressure. As shown on the left-hand side of table 1, there is good agreement (as expected) between the 0D scaling model predictions and TRANSP calculations for the volume-average temperatures, profile peaking factors, thermal and fast stored energy and β values, bootstrap fraction and NBI current drive (NBICD). The middle (white columns) of table 1 show parameters for the NSTX reference scenario with $I_P = 1$ MA computed from the 0D model for density values $f_{GW} = 0.5$ and 1.0. These f_{GW} values span the lower and upper bounds of NSTX normalized density (see figure 3) and allow direct comparison with NSTX Upgrade scenario projections which use the same f_{GW} values as shown on the right-hand side of table 1.

An overview of the calculations and assumptions for the NSTX Upgrade scenarios in table 1 is as follows: the NSTX Upgrade aspect ratio A is fixed at 1.7 and the elongation κ is fixed at 2.75. These values are based on typical results obtained with free-boundary equilibrium calculations. The toroidal field values chosen are 0.75 T to access high β and/or long pulse, and 1.0 T for elevated q and/or access at least a factor of 2 reduction in ν^*. NSTX Upgrade scenarios are evaluated assuming two confinement scalings: ITER IPB98(y,2) H-mode scaling [11, 12] (with a confinement scaling multiplier of unity, i.e. $H_{98} = 1$) and an ST-specific confinement scaling based on combined NSTX and MAST scalings described in more detail in section 2.1.3. For the 0D scalings described here, the effects of toroidal rotation are ignored. However, estimates of the projected toroidal rotation normalized to the NSTX reference scenario are also provided in section 2.1.3 and in table 1.

One potential issue for operation at high density is a degradation of confinement. In particular, achieving $H_{98} = 1$ with $f_{GW} = 1$ may not be possible without sufficient boundary shaping [12]. However, high triangularity has been shown to enable access to $H_{98} = 1$ with f_{GW} approaching 1 [57, 58]. To address this issue, figure 3(a) shows the NSTX confinement multiplier H_{98} (obtained from TRANSP power balance analysis) versus Greenwald fraction using the confinement database from section 4.2 of [56]. As is evident from the figure, there is no obvious degradation of confinement multiplier with normalized density for this database of NSTX plasmas with a wide range of plasma parameters and where all shots use at least some lithium conditioning of the PFCs [56]. One possible explanation for this weak dependence of H_{98} on density is the high triangularity and strong boundary shaping already incorporated in most NSTX operating scenarios [56, 59]. Figure 3(a) also shows that $0.5 \leqslant f_{GW} \leqslant 1.05$ bounds nearly all of the NSTX data in this dataset, and figure 3(b) shows that f_{GW} in the range 0.6–0.9 is more representative of higher I_P operation in NSTX. Based on these results, $f_{GW} \approx 0.75$ is taken to be most representative of NSTX operation, and NSTX Upgrade scenarios are calculated at bounding values of $f_{GW} = 0.5$ and 1.0 in table 1. However,
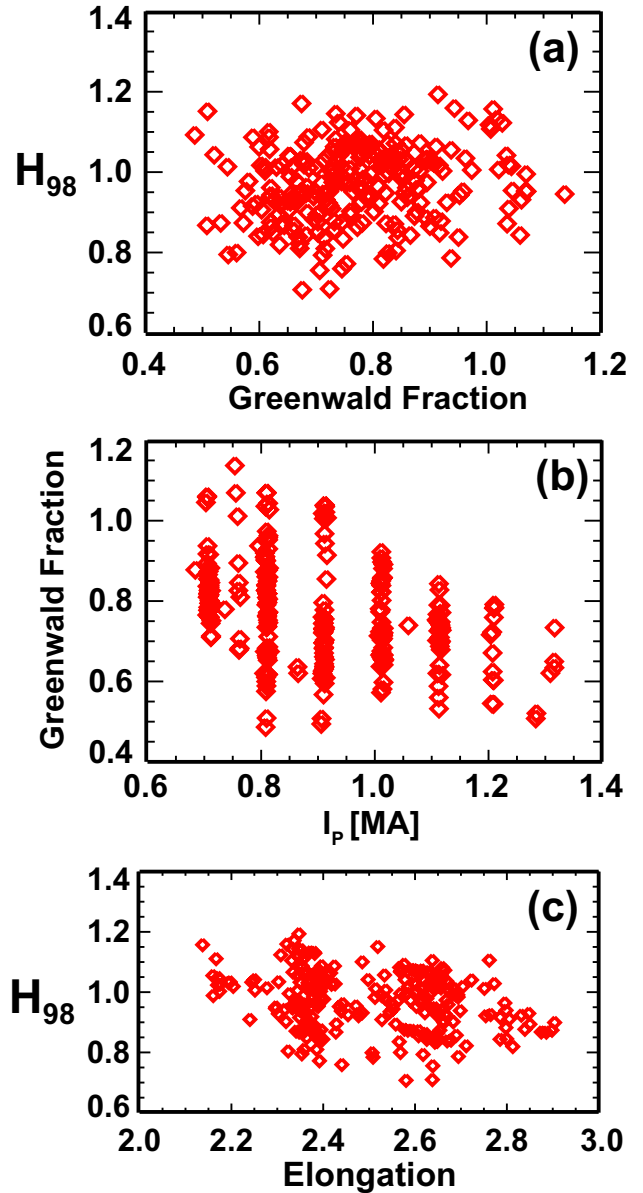
Figure 3. (*a*) NSTX H-mode thermal confinement multiplier H_{98} relative to the ITER H-98(y,2) confinement scaling versus Greenwald density fraction, (*b*) Greenwald fraction versus plasma current and (*c*) H_{98} versus elongation.

from figure 3(b) it is also evident that it is typically difficult to access high Greenwald fraction at high plasma current in NSTX. This is due in large part to the reduced flat-top duration (due to limited solenoid flux) at high current which does not provide sufficient time for the density to reach high f_{GW} or to approach equilibrated conditions. Thus, increased flat-top duration in NSTX Upgrade would significantly aid density limit studies at high current. Figure 3(c) shows H_{98} versus elongation and may indicate a weak degradation in normalized confinement with increased elongation. However, $H_{98} \geqslant 1$ has been achieved for $\kappa \leqslant 2.75$ in NSTX and supports using $H_{98} = 1$ and $\kappa = 2.75$ for NSTX Upgrade scenario projections as used in table 1.

Using the assumed toroidal field, confinement model, and normalized density fraction, it is straightforward to project the

thermal stored energy, volume-average temperatures (based on scaled NSTX profile shapes) and plasma resistivity and NBICD efficiency assuming a constant $Z_{eff} = 2.5$. To account for the fact that the electrons are typically the dominant energy loss channel in NSTX, and to approximate the effects of collisional coupling between electrons and ions as the density is varied, the ratio T_i/T_e is linearly reduced from 1.12 to 1.02 as the Greenwald fraction is increased from 0.5 to 1 in the NSTX Upgrade scenario projections. It should also be noted that for the 80–100 keV deuterium NBI heating of NSTX, the power to the electrons and ions is approximately equal when $T_e = 1.2$ keV, and more power goes to the ions for higher electron temperatures. With the toroidal field, plasma current, and electron temperature determined, the normalized electron collisionality ν_e^* in table 1 is calculated at fixed $\epsilon = A^{-1}$ at a representative q surface in the plasma core (taken to be $q = 2$) and also for the cylindrical safety factor $q^* \equiv \epsilon(1 + \kappa^2)\pi a B_T/\mu_0 I_P$ to better account for q variation from scenario to scenario.

The NSTX Upgrade scenario pulse durations are designed to utilize most or all of the TF flat-top and/or available OH solenoid flux. In particular, all of table 1 scenarios with heating powers of 10 MW or below have I_P flat-top values of 5 s or more to provide a number of current redistribution times comparable to or larger than the number in the NSTX reference scenario. For scenarios requiring flat-top inductive current drive, the pulse duration requirement, plasma resistivity and surface voltage required to support a given plasma current are used to determine the required OH solenoid flux and to ensure the flux used does not exceed the total available flux.

For the neutral beam heating and current drive calculations, an NBI full energy of injection $E_{NBI} = 80$ keV is typically used, except for the $P_{NBI} = 15$ MW scenario which has $E_{NBI} = 100$ keV. The fast-ion stored energy is assumed to be proportional to the product of P_{NBI} and the fast-ion thermalization time [60, 61] and is normalized to TRANSP fast-ion stored energy calculations for NSTX. The fast-ion and thermal stored energies are then used to compute the total stored energy, β_N and β_T values. The NBICD efficiency [62] is assumed to be proportional to $P_{NBI}T_e(1 - 1/Z_{eff})/n_e$ [63, 64] and is normalized to TRANSP NBICD calculations which have been previously shown good agreement with experimentally inferred values in NSTX [65, 66] when core MHD activity is sufficiently weak. The bootstrap current fraction [67–69] $f_{BS} = I_{BS}/I_P$ is assumed to scale as $C_{BS}\sqrt{\epsilon}\beta_{pol-th}$ where β_{pol-th} is the poloidal beta using the thermal pressure and $C_{BS} = 0.52$ is used based on NSTX bootstrap-current-fraction analysis from TRANSP. Once the bootstrap current and NBI current are calculated for a given scenario, these currents are subtracted from the total scenario target current, and the remaining current must be provided by inductive current drive. The plasma T_e and Z_{eff} are used to calculate a plasma resistance value and to compute the required surface voltage to drive any inductive current.

2.1.3. Energy and momentum confinement assumptions. The thermal energy confinement scalings used in the 0D scenario projections are assumed to vary as $\tau_{E,thermal} \propto I_P^{\alpha_I} B_T^{\alpha_B} n^{\alpha_n} P^{\alpha_P} R^{\alpha_R} \epsilon^{\alpha_\epsilon}$. The ST confinement scaling exponents from NSTX using OLS (ELMy) analysis [70] are $\alpha_I = 0.58$,

$\alpha_B = 1.01$, $\alpha_n = 0.43$, $\alpha_P = -0.70$. Similarly, the scaling exponents from MAST also using OLS analysis [8] and assuming the thermal stored energy is linearly proportional to the total stored energy are $\alpha_I = 0.59$, $\alpha_B = 1.4$, $\alpha_n = 0.0$, $\alpha_P = -0.73$. It should be noted that OLS and PCEIV analyses give similar but not identical exponents for the engineering variables in each of the NSTX and MAST scalings, and the differences in the exponents for the different analysis methods are comparable to the values of the uncertainties of the exponents themselves. Further, to account for the differences between the NSTX and MAST exponents, the ST-specific confinement scaling used in all subsequent analysis shown in table 1 uses the average value of the exponents from NSTX and MAST rounded to the nearest single decimal place, namely $\alpha_I = 0.6$, $\alpha_B = 1.2$, $\alpha_n = 0.2$, $\alpha_P = -0.7$. The major radius and inverse aspect ratio exponents are taken from the ITER IPB98(y,2) H-mode scaling: $\alpha_R = 2.0$, $\alpha_\epsilon = 0.6$. The elongation dependence is ignored here since a fixed value $\kappa = 2.75$ is used in the 0D analysis for NSTX Upgrade. The ST-specific confinement scaling coefficient is chosen based on matching the ITER scaling τ_E for the NSTX reference scenario in table 1 with $I_P = 1$ MA, $B_T = 0.45$ T, $A = 1.5$, $R_0 = 0.86$ m, $\kappa = 2.6$, $P_{NBI} = 6$ MW and $f_{GW} = 1$.

With respect to collisionality reduction relative to the NSTX reference scenario, a factor of 4–5 decrease in collisionality is projected to be achievable at fixed Greenwald fraction by operating at 1 T, 1.5 MA and 6 MW assuming ST confinement scaling (right-most green columns). This strong decrease in collisionality at current and power values similar to the present NSTX is the result of the strong toroidal field dependence of the ST confinement scaling. In contrast, if ITER H-mode confinement scaling is assumed, only a factor of 2–3 reduction in collisionality would be achieved even with two times higher current and/or power (red and left-most NSTX-U green columns) due to the weak toroidal field dependence of the ITER confinement scaling. Thus, the ability to double the toroidal field, plasma current and heating power is needed to reduce the uncertainty in the scaling of ST energy confinement as plasma temperatures are increased towards the values of next-step STs.

An important requirement for achieving reduced ion collisionality through increased ion temperature is to suppress ITG/TEM ion-gyro-scale turbulence. Previous confinement studies in NSTX have shown the ion thermal diffusivity in NBI-heated H-mode plasmas is near neoclassical values in the outer half of the minor radius [7] as predicted in early projections of ST energy confinement [71]. This is consistent with the likely suppression of low-k turbulence since the $E \times B$ shearing rate $\gamma_E = (r/q)\mathrm{d}(E_r/RB_P)/\mathrm{d}r \approx -(r/q)\partial\Omega_\phi/\partial r$ [72, 73] significantly exceeds the ITG/TEM maximum linear growth rate γ_{lin} [7]. Here $\Omega_\phi = v_\phi/R$ is the toroidal angular rotation frequency, v_ϕ is the toroidal rotation velocity, R is the major radius and the poloidal rotation and pressure gradient terms in the radial force balance equation used to determine E_r have been ignored. To estimate the approximate magnitude of the toroidal rotation velocity v_ϕ in NSTX Upgrade, we note that the angular momentum flux $\Gamma_\phi = -mnR\chi_\phi\partial v_\phi/\partial r + mnRv_{pinch}v_\phi$ has both a diffusive and a pinch contribution [74]. Here m and n are the ion mass and density respectively. The angular momentum diffusivity χ_ϕ is

anomalous and generally exceeds the neoclassical momentum diffusivity by a large factor, and a predictive capability for χ_ϕ does not yet exist. However, in the outer region of the plasma, the momentum pinch measured in NSTX is in reasonable agreement with a low-k turbulence-driven pinch term of the form $Rv_{\mathrm{pinch}} \approx -\chi_\phi(4 + R/L_n)$ where L_n is the density gradient scale-length [74, 75]. Using this expression for the pinch term, the momentum flux can be approximated as $\Gamma_\phi \approx -mn\chi_\phi[R\partial v_\phi/\partial r + (4 + R/L_n)v_\phi]$, and in steady-state, $\nabla \cdot \Gamma_\phi = S_\phi$ where S_ϕ is a source term for angular momentum (i.e. NBI). Assuming similar profile shapes between NSTX and NSTX Upgrade, then $v_\phi \propto S_\phi/n\chi_\phi$. The values of χ_ϕ in the outer region of the plasma in NSTX are observed to be roughly proportional to χ_i, and after accounting for the inward pinch term in the analysis, the Prandtl number $\chi_\phi/\chi_i \approx 0.5$–$0.8$ [74]. Assuming $\chi_\phi \propto \chi_i$, then $v_\phi \propto S_\phi/n\chi_i$, and if $\chi_i \approx \chi_{\mathrm{i\text{-}neo}}$, then $v_\phi \propto S_\phi T_i^{1/2} I_P^2/n^2$. The validity of this scaling for v_ϕ is clearly questionable, as it remains unclear if χ_ϕ in NSTX scales with either the turbulent or neoclassical χ_i, and this is a topic for future research.

Nevertheless, the above 0D scaling for v_ϕ can be applied to the scenarios in table 1 which tabulates the projected toroidal rotation normalized to the NSTX reference cases at the same Greenwald density fraction. The calculations indicate that the toroidal rotation could be up to 4 times larger in the Upgrade and approximately a factor of two higher on average considering all of the Upgrade scenarios in table 1. Finally, it is noted that the ITG/TEM linear growth rate γ_{lin} is proportional to $T_i^{1/2}$, and that for all the scenarios with strong NBI heating, $\gamma_E/\gamma_{\mathrm{lin}}$ in NSTX-U will be comparable to or will exceed the NSTX ratio. Thus, it is expected that ITG/TEM turbulence will remain largely suppressed. However, the low-NBI-power scenario with high bootstrap fraction has a ratio $\gamma_E/\gamma_{\mathrm{lin}} \approx 1/3$ of the NSTX reference value, so it is questionable whether the turbulent ion thermal diffusivity would remain sub-dominant to the neoclassical diffusivity in this scenario.

2.1.4. Pulse duration requirements. The required coil and plasma current pulse duration is another important consideration for the design of NSTX-U. The current redistribution time [76] τ_{CR} is generally the longest profile relaxation time-scale, and on NSTX, 3–4 current redistribution times are typically required to achieve an equilibrated q profile. If the confinement continues to scale nearly inversely with collisionality at low collisionality, the current redistribution time could increase as much as a factor of 5 (compare rightmost green columns in table 1 to NSTX reference values). Thus, to ensure similar profile relaxation in the Upgrade, the plasma current and TF flat-top durations must increase by a factor of five to 5 s and 6.6 s, respectively.

2.1.5. Ohmic heating solenoid flux requirements. To assess ST physics at 2 times higher TF and similar safety factor q, the plasma current must double from 1 to 2 MA. Sufficient loop voltage must also be provided for any needed inductive current drive. The operating scenario analysis indicates that 2 MA plasmas at intermediate power levels (10 MW) assuming ITER confinement scaling and Greenwald fraction of 1 require the highest surface voltage (0.2 V) for sustainment,

and these scenarios determine the required flat-top OH flux of approximately 1 Wb to sustain a 5 s plasma current flat-top.

In addition to the flat-top flux, plasma initiation and current ramp-up are also important considerations for specifying the OH flux requirement. For plasma initiation/breakdown, the magnetic null quality and/or toroidal electric field must be sufficiently high for the plasma electron avalanche to occur to form a closed flux-surface tokamak configuration. A key metric for plasma breakdown is the electron energy gained before loss to the surrounding walls via parallel transport along the total (toroidal + poloidal) background magnetic field, and this gain is proportional to the Lloyd parameter $E_\phi B_\phi/B_\perp$ [77]. The NSTX Lloyd parameter is typically $4.2\,\mathrm{kV\,m^{-1}}$ at the major radius of the centrestack (CS) where plasma breakdown is initiated ($R_{\mathrm{BD}} = 0.185\,\mathrm{m}$) for a stray poloidal field (PF) $B_\perp$ of 10 G in the field-null region and a nominal toroidal field $B_{\mathrm{T}} = 0.36\,\mathrm{T}$ (60% of maximum toroidal field) at the plasma geometric centre ($R_0 = 0.86\,\mathrm{m}$). This value of the Lloyd parameter provides reliable plasma breakdown in NSTX for all toroidal field values commonly used in the experiment, and the same specification is used for NSTX Upgrade ($R_{\mathrm{BD}} = 0.315\,\mathrm{m}$) for a nominal toroidal field $B_{\mathrm{T}} = 0.6\,\mathrm{T}$ (again 60% of maximum toroidal field) at the Upgrade plasma geometric centre ($R_0 = 0.93\,\mathrm{m}$). To achieve this in the Upgrade, the available breakdown loop voltage is increased from 2.9 to 4.7 V which requires an increase in the OH power supply voltage from 2.7 to 4.1 kV.

The ohmic flux required for plasma current ramp-up is a function of the plasma resistance which is a function of plasma temperature and Z_{eff}, and is therefore a function of auxiliary heating and current drive and confinement scenario (L-mode versus H-mode). NBI heating and an early H-mode transition [78, 79] during the current ramp-up are commonly used on NSTX to minimize OH flux consumption to maximize the current flat-top duration. To illustrate the impact of NBI heating and H-mode transition during the current ramp, figure 4 compares the ramp-up evolution of ohmic L-mode versus early NBI + H-mode plasmas with similar I_{P} ramp rate and other initial plasma parameters. Sufficient NBI heating power is required (typically 3–4 MW) to induce H-mode during the current ramp, and a brief 10–20 ms pause in the I_{P} ramp is also sometimes used to reduce the H-mode threshold power to induce H-mode. As shown in figure 4(*a*) for the NBI+H-mode case, 2 MW of NBI power is injected at $t = 50$ ms followed by an additional 2 MW of heating power at $t = 100$ ms, and the H-mode is induced (without a pause in the current ramp) at $t = 125$ ms. As shown in figure 4(*b*), the evolution of the surface voltages are similar for the ohmic L-mode and NBI + H-mode plasmas prior to the application of NBI heating at $t = 50$ ms. As shown in figure 4(*b*), following the application of NBI heating power at $t = 50$ ms, the resistive component [80, 81] (green) of the surface voltage decreases from 1.4 to 0.6 V by the time of H-mode onset while the inductive component (blue) decreases only slightly. Figure 4(*b*) also shows that following the H-mode transition, the resistive component decreases further, and that the inductive component decreases from 0.7 to 0.3–0.4 V compared with the ohmic L-mode value of 0.8 V. Thus, the largest reduction in surface voltage in the NBI + H-mode ramp-up is from the reduction in the resistive component, but both components are reduced by NBI + H-mode during the
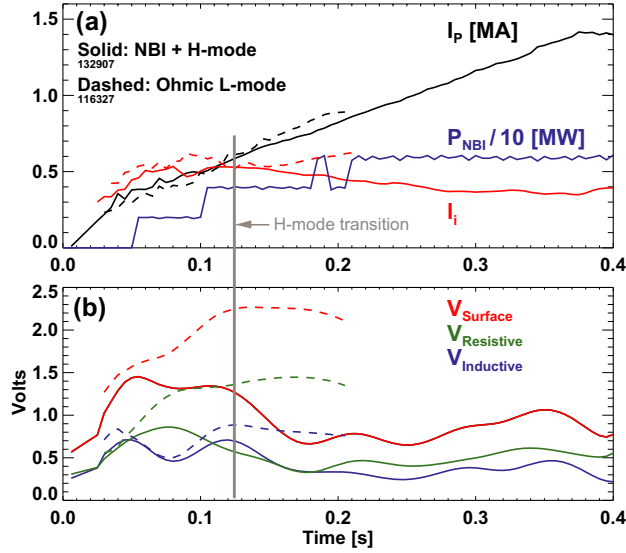
Figure 4. Comparison of plasma current ramp-up evolution for NSTX ohmic plasmas (dashed) versus early NBI-heated H-mode plasmas (solid) including: (*a*) plasma current (black), neutral beam injection power (blue) and internal inductance (red), and (*b*) surface voltage evolution (red) including the resistive (green) and inductive (blue) contributions.
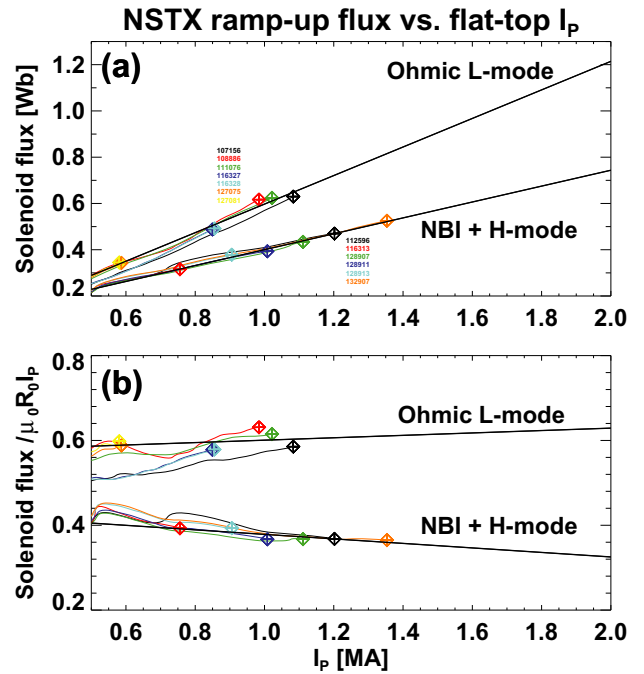

Figure 5. (*a*) Solenoid flux consumed for breakdown and ramp-up versus plasma current flat-top value and (*b*) normalized solenoid flux consumed versus current flat-top value for NSTX ohmic and early NBI-heated H-mode plasmas.

ramp-up. It should also be noted that any NBICD associated with the NBI heating during the ramp-up will also contribute to the reduction of the surface voltage required for current ramp-up. Overall, the combination of early NBI + H-mode reduces the required surface voltage by a factor of 2–2.5 following the H-mode transition, and this significantly reduces the solenoid flux consumed during the current ramp.

Given the difficulty of accurately modelling the flux consumption required for breakdown and ramp-up, figure 5 shows the flux used to achieve a given flat-top plasma current in NSTX for usage in extrapolating to NSTX Upgrade. As shown in figure 5(*a*), the total breakdown plus ramp-up flux consumption for NBI + H-mode extrapolates to 0.73 Wb for NSTX shapes, which corresponds to 0.8 Wb for NSTX Upgrade plasmas with larger major radius. Figure 5(*a*) also shows that the ohmic L-mode ramp-up extrapolates to a significantly higher solenoid flux requirement of 1.22 Wb for NSTX plasma shapes which corresponds to 1.4 Wb for NSTX Upgrade plasmas. As shown in figure 5(*b*), the major-radius-normalized total poloidal flux consumption (Ejima–Wesley coefficient [80, 82]) extrapolates to 0.3–0.35 for the NBI+H-mode ramp-up which is 50–55% of the ohmic L-mode value and approximately 60% of the ohmic plasma value reported previously in NSTX [81] for current ramp rates near 5 MA s^{-1}. Thus, including the breakdown + ramp-up flux required (0.8 Wb) assuming NBI+H-mode during the ramp-up in addition to the current flat-top flux (1 Wb), the total OH flux required is estimated to be 1.8–2 Wb to support 2 MA plasma current with 5 s flat-top.

If NBI heating + H-mode confinement was not utilized in the current ramp, the total solenoid flux requirement would increase by approximately 30% and require a 13–15% increase in the diameter of the CS. Such an increase would increase the minimum (i.e. limiter to limiter) aspect ratio of NSTX Upgrade from 1.5 to 1.6 and eliminate the ability to achieve diverted

plasmas with aspect ratios matching those of proposed future STs with $A \leqslant 1.6$ such as ARIES-ST. Further, such a diameter increase would also significantly reduce the remaining horizontal inboard divertor surface area and eliminate the space for additional divertor coils. Such considerations strongly influence the choice of diameter of the CS and OH solenoid and therefore motivate the usage of NBI heating + H-mode during the plasma current ramp of NSTX Upgrade.

2.1.6. Requirements for access to high beta. The ability to access normalized and toroidal beta values in NSTX-U comparable to those achieved in NSTX is also important for assessing the stability and transport as a function of beta and ν^* at reduced ν^*. As is evident from table 1, for the ST confinement scaling, access to high temperature and beta is achievable with heating power comparable to that in NSTX. However, for ITER H-mode scaling, substantially more power (factor of 2–3 times higher) is required to achieve similar beta values at similar safety factor q^* (see middle yellow and red NSTX-U columns in the table). The PF coil system must also be capable of providing sufficient field to maintain equilibrium force balance to access high β values at full toroidal field and plasma current. For NSTX, $\beta_T = 20$–25% and $\beta_N = 4.5$–6 have been sustained for many energy confinement times and at least a current redistribution time [56]. As is evident from table 1, access to similar performance values in NSTX Upgrade requires supporting plasmas with stored energy W_{TOT} up to 1.35 MJ. Access to the with-wall β_N limit $\leqslant 6.5$ and l_i up to 0.6 [56] requires additional PF capability for W_{TOT} up to 1.5–1.6 MJ.
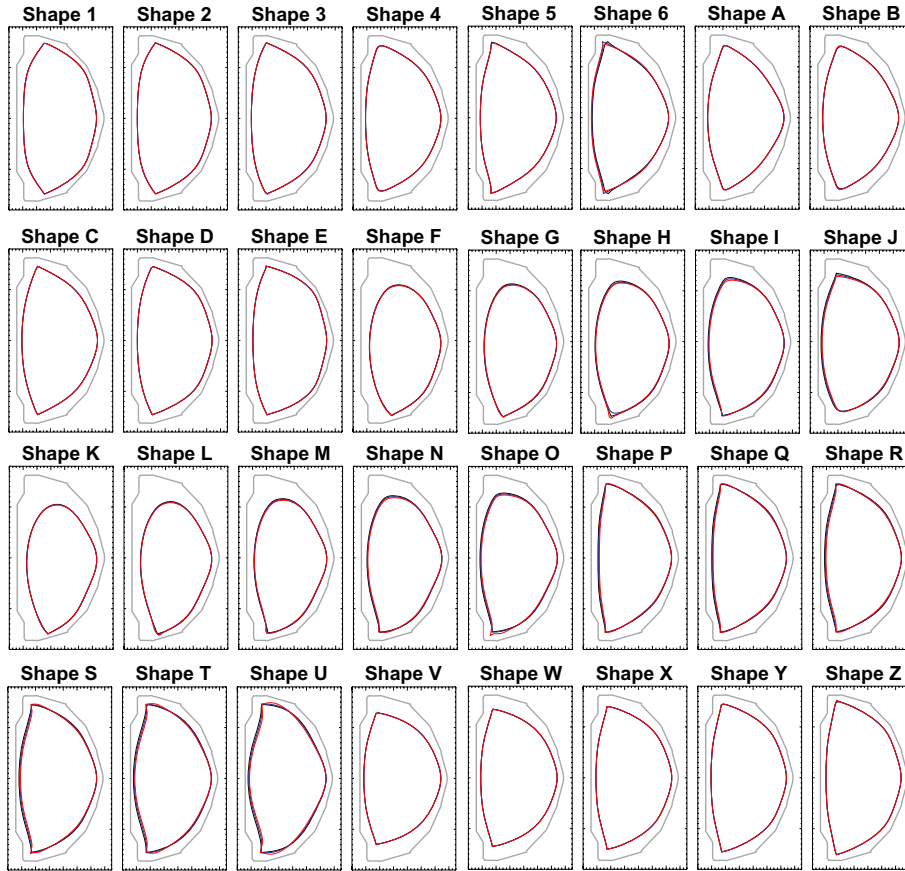
Figure 6. Plasma boundaries of free-boundary equilibria used for assessing PF coil current requirements in NSTX Upgrade. Each plot is a superposition of three boundary plots, i.e. one for each OH power supply current state assessed: 0 and ±24 kA.

2.1.7. PF requirements. To enable engineering design of the upgrade, systematic free-boundary equilibrium calculations have been performed to determine the Upgrade PF requirements. The design range spans aspect ratio $A = 1.6$–1.9, internal inductance $l_i = 0.4$–1.1, elongation $\kappa = 2.1$–2.9, triangularity $\delta = 0.2$–0.7, squareness $\zeta = -0.15$–0.12, magnetic balance $\delta_{Rsep} = -1.5$–0 cm, normalized beta $\beta_N = 1$, 5 and 8, and OH solenoid current $= 0$ and ±24 kA (i.e. the power supply limits) to determine the divertor PF needed for cancellation of OH leakage flux. Figure 6 shows the 32 plasma boundaries of free-boundary equilibria used for assessing the PF coil current requirements for 2 MA NSTX Upgrade plasmas. Each boundary shown is actually a plot of three plasma boundaries for each state of the OH coil current described above, and this set of 96 equilibria provides the set of configurations used for the detailed engineering design of the Upgrade. The PF coil currents for each configuration are shown in figure 7 for 2 MA plasmas with $\beta_N = 5$, and the PF coil locations and sizes and the minimum and maximum currents as a function of β_N are shown in figure 8. As is evident from figure 8, the most substantial changes in coil current for varied β_N are for the primary vertical field coil (PF5) and the inner-most divertor coil (PF1A).

In addition to accounting for variation in the plasma shape, the PF coil current requirements have also been assessed as a function of plasma current profile (internal inductance) and normalized beta for 2 MA, 1 T plasmas. The plasma inductance and beta primarily influence the required vertical

field (PF5) coil current, and as shown in figure 9, increased inductance and beta both increase the required vertical field. The Upgrade power supply system [83] is designed to increase the maximum PF5 current by 50% from 20 to 30 kA nominal maximum operating current. This enhancement will enable 2 MA equilibria with β_N up to 5 at $l_i = 1$, and β_N up to 8 at $l_i = 0.6$, and this increased vertical field capability supports all scenarios used for the Upgrade design, including access to the with-wall β_N limit. For reference, the NSTX Upgrade OH and PF coil turns-count and minimum and maximum currents used for the electromagnetic forces and structural analysis are summarized in table 2. It should be noted that the PF2 and PF4 power supplies are nominally unipolar in the present NSTX and in the NSTX Upgrade design but can be upgraded to bipolar operation.

2.1.8. Vertical control requirements. In addition to providing sufficient field for plasma equilibrium, the PF coil and power supply system must also provide robust vertical position control. NSTX uses the rt-EFIT real-time equilibrium reconstruction algorithm [84] for real-time shape and vertical position control [85–88] which has enabled the sustainment of high elongation $\kappa = 2.5$–2.8 plasmas with high performance [56, 59]. Very high $\kappa = 2.8$–3 has also been controlled for shorter durations in NSTX [79]. The vertical stability and controllability of the tokamak plasma is a function of the internal inductance, plasma pressure, distance between
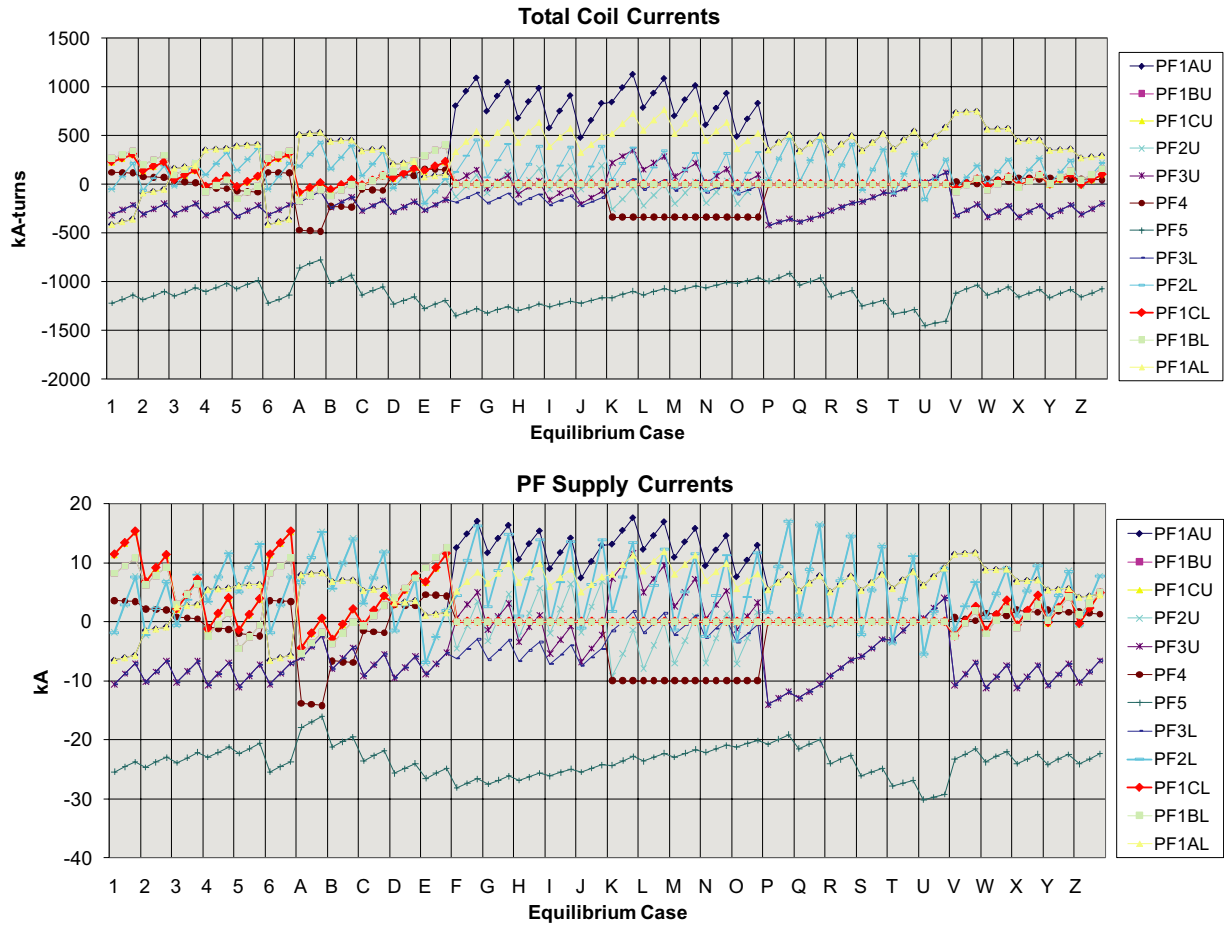
Figure 7. Total coil current (top) and power supply current (bottom) required for each of the 96 reference 2 MA Upgrade equilibria.
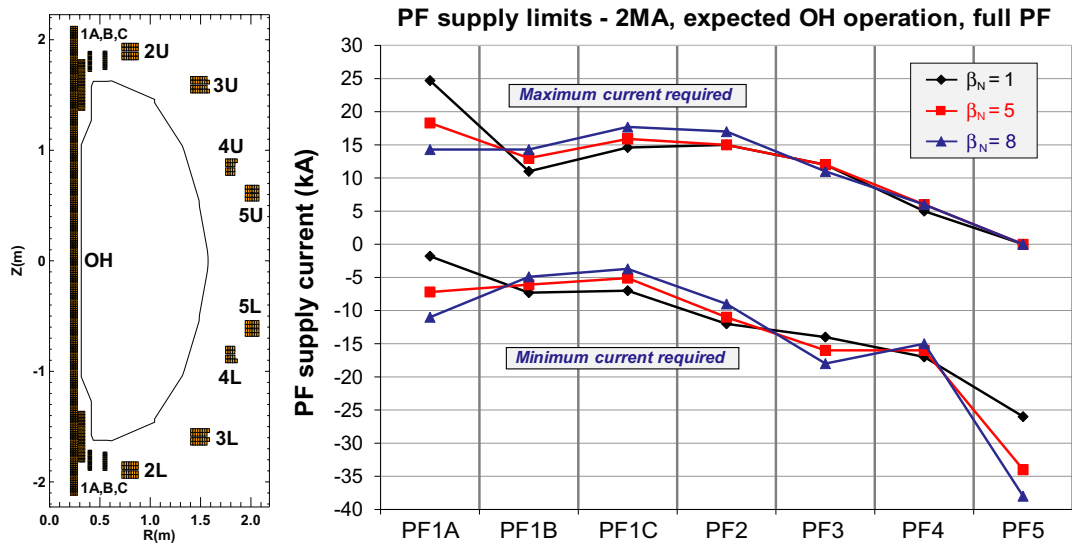
Figure 8. (Left) PF and OH coil current locations, sizes, and limiter boundary and (right) minimum and maximum PF coil current versus β_N.

the plasma and the conducting wall, the location and type of sensors used for measuring vertical position and the plasma aspect ratio and boundary shape [1, 89–95]. Assessing the impact of increased A and κ on ST confinement and stability is an important objective of NSTX Upgrade research. Increased A and κ are both destabilizing to the $n = 0$

mode, and this trend has motivated dedicated experiments in NSTX to simultaneously increase A and κ (by increasing the inboard plasma-wall gap) in order to determine the $n = 0$ controllability space for boundary shapes similar to those expected in NSTX Upgrade [56]. In these dedicated experiments, plasmas with $A = 1.65$–1.75 and $\kappa = 2.7$–2.9
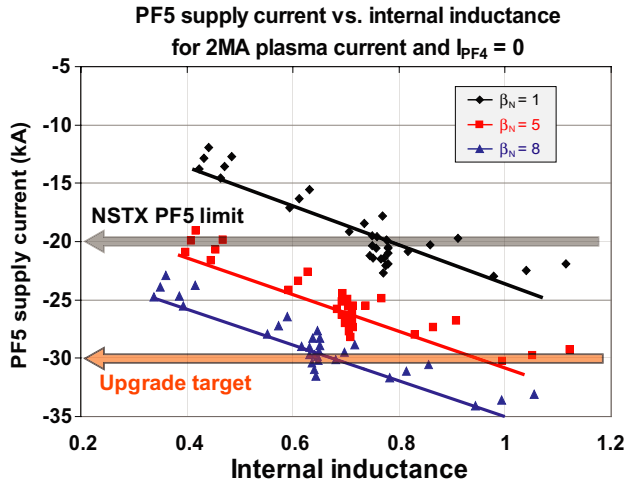
Figure 9. PF5 vertical field coil current required to support 2 MA plasmas as a function of internal inductance and normalized beta.

Table 2. NSTX Upgrade OH and PF coil number of radial layers (NR), vertical layers (NZ), total turns-count, power supply current multiplier with respect to the required equilibrium current, and minimum and maximum power supply and total coil currents.

Coil	NR	NZ	Turns	Equilibrium multiplier	Min power supply (kA)	Max power supply (kA)	Min coil (MA turns)	Max coil (MA turns)
OH	4.0	221	884	1.0	−24.0	24.0	−21.2	21.2
PF1AU,L	4.0	16	64	1.1	−7.2	18.3	−0.46	1.17
PF1BU,L	2.0	16	32	1.1	−6.0	13.0	−0.19	0.42
PF1CU,L	2.0	10	20	1.1	−5.0	15.9	−0.10	0.32
PF2U,L	7.0	4	28	1.1	−11.0	15.0	−0.31	0.42
PF3U,L	7.5	4	30	1.1	−16.0	12.0	−0.48	0.36
PF4	8.5	4	34	1.1	−16.0	6.0	−0.54	0.20
PF5	6.0	8	48	1.1	−34.0	0.0	−1.63	0.00

were formed and controlled and the natural evolution of the current profile provided variation (i.e. an increase) of l_i.

Figure 10(a) shows the NSTX experimental κ versus l_i operating space sorted by aspect ratio with the lowest $A = 1.2$–1.4 in red, typical NSTX $A = 1.4$–1.6 in blue, and the highest $A = 1.6$–1.8 in green from the experiments dedicated to producing NSTX Upgrade-like shapes. As is evident from figure 10(a), $\kappa \approx 2.7$–2.8 has been sustained for $l_i < 0.65$ for a range of aspect ratios $A = 1.4$–1.8 which includes aspect ratios $A = 1.6$–1.8 anticipated for NSTX Upgrade. However, for the cases with $A = 1.6$–1.8, loss of vertical control occurred for $l_i \geqslant 0.65$ indicating that control of higher κ and/or high κ at higher l_i will require vertical control improvements such as improved plasma vertical motion detection utilizing more magnetic sensors (recently implemented) and control gain optimization (planned) [88]. Typical l_i values for NSTX high-performance plasmas are 0.5–0.65 [56, 66]. Most importantly, the $A = 1.7$, $\kappa = 2.7$–2.8 plasmas obtained thus far have $l_i \leqslant 0.55$ [56], and these plasmas and parameters (indicated by the square black symbol in figure 10(a)) provide the basis for the 0D scalings in table 1. Further, these higher aspect ratio plasmas obtained in NSTX also provide the basis for free-boundary TRANSP projections to NSTX Upgrade
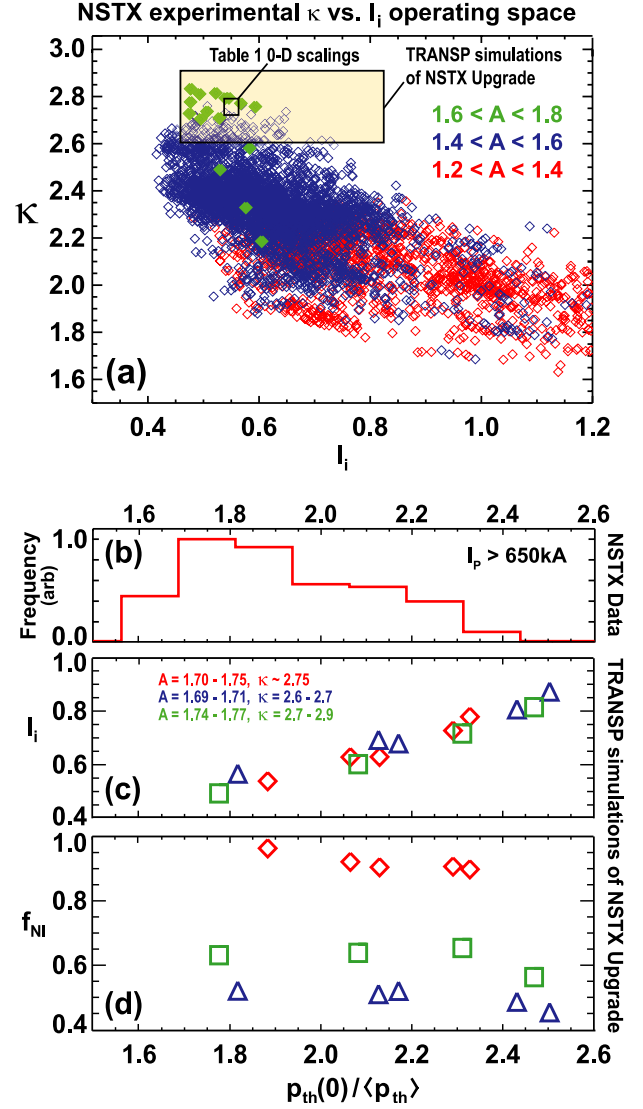
Figure 10. (*a*) NSTX experimental κ versus l_i operating space sorted by aspect ratio, (*b*) histogram of thermal pressure profile peaking factor in NSTX, (*c*) l_i and (*d*) non-inductive current drive fraction f_{NI} versus thermal pressure profile peaking factor for TRANSP simulations of NSTX Upgrade. The yellow shaded rectangle in (*a*) indicates the approximate range of κ and l_i values for the TRANSP simulations of NSTX Upgrade.

[55] including an assessment of the equilibrium and kink stability properties as a function of confinement and profile assumptions, gap between the plasma and outer limiter and conducting wall, anomalous fast-ion diffusivity, and impurity concentration.

A potentially important consideration for NSTX Upgrade vertical stability (and $n > 0$ stability) is the impact of reduced collisionality on pressure profile peaking [96, 97]. For example, increased density profile peaking would make the bootstrap current profile [98] more peaked and increase l_i. Assuming density profile peaking in NSTX Upgrade scales similarly to conventional aspect ratio tokamaks, and further assuming the collisionality decreases by a factor of 5 in NSTX Upgrade and the NBI power and temperature double, equation (3) of [97] can be used to estimate the increment in density peaking factor to be 0.2–0.3. Most of this projected
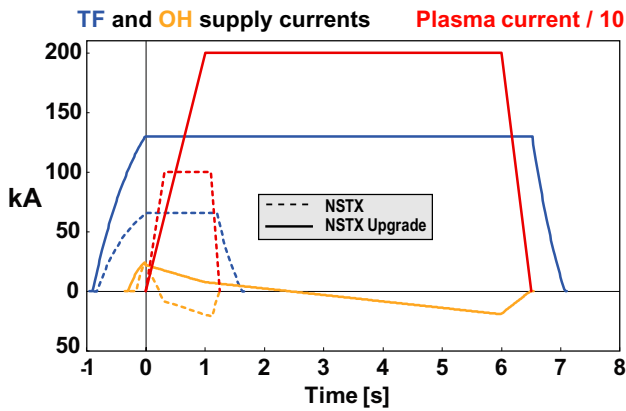
Figure 11. Comparison of toroidal field (TF), ohmic heating (OH) and plasma current waveforms for plasmas operated at the maximum toroidal field capabilities of NSTX (0.55 T) and NSTX Upgrade (1 T).

increment comes from the collisionality dependence of the density peaking factor since the projected normalized NBI particle source term $\Gamma^*_{NBI} \leqslant 0.1$. Figure 10(*b*) shows that the most probable thermal pressure profile peaking factor in NSTX is $p(0)/\langle p \rangle \approx 1.8$. If this value increases by 0.3 to 2.1 in NSTX Upgrade, figure 10(*c*) shows that the projected internal inductance from TRANSP simulations increases from 0.5 to 0.6–0.7 essentially independent of plasma scenario and spanning a range of non-inductive current fraction $f_{NI} = 0.5$–1 as shown in figure 10(*d*). Thus, if the pressure profile peaking factor increases by more than 0.2–0.3 in NSTX Upgrade, the vertical control improvements mentioned above may be required to operate stably with $\kappa \geqslant 2.7$. It is also possible that peaking of the pressure will not increase significantly in NSTX Upgrade, as there is evidence that the temperature profile can broaden with increased toroidal field [7]. Further, the application of lithium surface coatings has also been shown to lead to broadened electron temperature profiles and reduced internal inductance [99].

2.2. Upgrade engineering design

To summarize the combination of requirements above, the Upgraded NSTX device should: double B_T at $R = 0.93$ m from 0.5 to 1 T and increase the TF flat-top duration to 6–7 s, double I_P from 1 to 2 MA and provide a 5 s flat-top at full current, double the neutral beam injection (NBI) heating power from $P_{NBI} = 5$ MW to 10 MW and sustain it for 5 s, and nearly triple the OH flux from 0.75 Wb to 2 Wb. Representative waveforms for the NSTX and NSTX Upgrade currents are shown in figure 11 and illustrate the substantial increase in device performance to be achieved with the Upgrade.

2.2.1. New CS.

An important feature of the NSTX device design is the ability to remove the CS independent of the vacuum vessel and the external PF and TF magnets. Thus, Upgrade performance requirements can potentially be met by replacing the present CS with a new larger CS thereby providing more cross-sectional area and conductor to carry the TF current and also providing increased OH flux. The increased size of the new CS is shown graphically
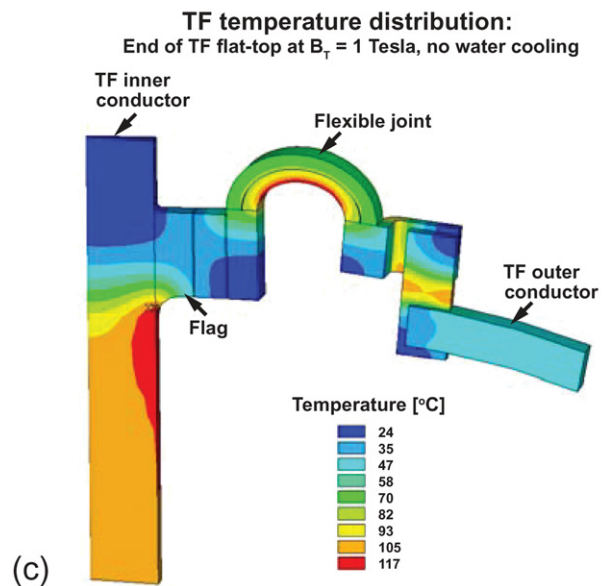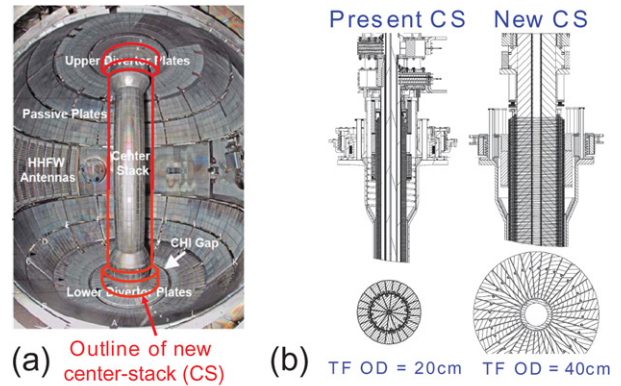
Figure 12. (*a*) Outlines and (*b*) cross-sections of the present and new CS for comparing the TF conductor diameters and (*c*) temperature distribution at end of TF flat-top for $B_T = 1$ T operation and no TF conductor cooling during the pulse.

in figure 12(*a*) by the red outline overdrawn on the present CS. Figure 12(*b*) shows the doubling of the TF conductor diameter which enables the doubling of TF current with 5 times longer pulses. The TF flat-top pulse length of 6.5 s at full current is limited by the temperature rise within the coil, and figure 12(*c*) shows the predicted temperature distribution within the conductor at the end of TF flat-top operating at the maximum toroidal field of 1 T [100]. Figure 12(*c*) shows that the maximum temperature reaches 117 °C without water cooling, and tends to peak near the region where the TF inner conductor interfaces with the flag extension and also on the inner diameter of the flexible joint arch. Both locations are regions of maximum current density. With water cooling, the maximum upper/lower temperatures of the inner TF conductor reach 111/113 °C which is within the allowable limits for the epoxy chosen to bond the insulation to the conductor [100]. The outer TF conductors are also water cooled, but only reach approximately 50 °C for the same full-current pulse. The flexible joints [101] connecting the inner and outer TF conductors and enabling the vertical growth of the inner TF bundle are cooled between shots by thermal conduction to the inner and outer TF conductors.
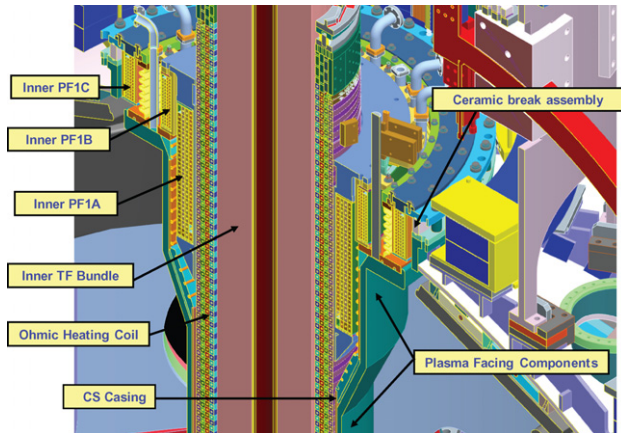
Figure 13. Detailed cross-section of the Upgrade CS showing the TF, OH and divertor PF coils, and the CHI insulator and PFC boundaries.

The OH coil diameter also nearly doubles in the new CS and can provide up to nearly 4 times higher solenoid flux-swing for sufficiently fast swing, and 3 times higher flux-swing for 5 s 2 MA flat-top plasmas. Coil self-forces and forces from electromagnetic interactions with other PF coils have been accounted for, and the maximum OH conductor temperature is designed to be limited to 100 °C [102]. The water cooling flow-rate will be controlled to limit the thermal stress induced by the water coolant 'wave' that propagates through the vertical height of the OH during the post-shot cool-down period. It should be noted that the number of OH coil windings in NSTX Upgrade has been reduced from the originally planned 1016 [102] to 884 to enable inter-shot cool-down times of 15 min or less (versus 19 min) to increase the number of possible full-performance shots per hour. For reference, the typical inter-shot period on NSTX is 10–12 min. As shown in figure 13, this larger CS incorporates the larger TF and OH while also including three upper and lower divertor PF coils PF1A,B,C (compared with two/one PF coils in the lower/upper divertor of NSTX) and also providing an insulating break for biasing the CS casing relative to the vessel for coaxial helicity injection (CHI) current start-up. This larger outer diameter (OD) CS increases the minimum aspect ratio of fully limited plasmas from $A = 1.3$ to $A = 1.5$. As a result, diverted plasmas will typically have $A \geqslant 1.6$. While this aspect ratio is larger than the present NSTX, it is comparable to the optimal aspect ratio identified in ST-FNSF [3, 4], ST Pilot Plant [103], and ARIES-ST reactor studies [104].

Lastly, another important design feature of the new CS is the relocation of the OH coil current leads from the top to the bottom of the CS to eliminate the stress on the leads arising from the vertical thermal expansion of the OH coil. Further, the OH coil lead area has been redesigned to utilize a coaxial current feed (shown in figure 14) to minimize the non-axisymmetric fields from, and forces on, the OH coil which play a significant role in generating the $n = 1$ error field in the present NSTX [44].

2.2.2. Structural enhancements. Doubling the TF and plasma current increases the forces on the coil supports and vacuum vessel (VV) up to a factor of 4, and substantial
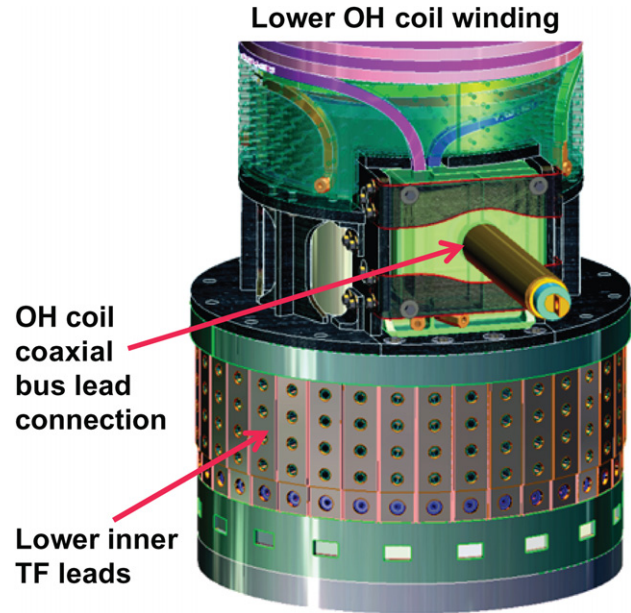
Figure 14. Design drawing of the lower OH coil winding area including the coaxial bus lead connection and lower inner TF leads.
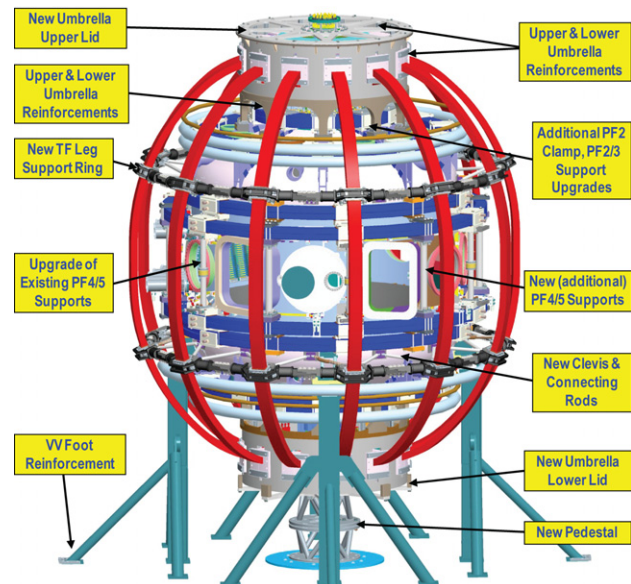
Figure 15. Vessel reinforcements and other modifications required for handling the increased forces associated with higher field and current of NSTX Upgrade.

analysis and design has been performed to provide structural reinforcement against these increased loads. A graphical summary of the external structural modifications for NSTX Upgrade is shown in figure 15. In figure 15, the PF coils are shown in blue, the outer TF coils are shown in red, and the TF coils are connected mechanically to the vacuum vessel through cylindrical 'umbrella' structures (grey) at the top and bottom of the vessel. The NSTX Upgrade structural modifications include a new flexible umbrella upper lid to allow OH/TF vertical thermal expansion while transferring torsional loads of the CS to the outer vessel, stronger connections of the TF coils

to the umbrella structure and strengthening of the umbrella legs and feet, new TF support rings and clevises to transfer torsional loads on the TF coils to the vacuum vessel, new and upgraded vertical field coil (PF4 and 5) separator struts to take increased inter-coil forces, improved PF2 and PF3 coil supports, a new pedestal on which the CS is supported, and improved vessel supports.

Particular emphasis has been placed on the increased torsional load applied to the outer TF legs from the Lorentz force of the poloidally directed TF coil current crossed with the radial and vertical field from the PF coils. Evaluation of the three components of the load in cylindrical coordinates finds the radial load is carried by the cylindrical umbrella and the near-midplane TF coil supports, and the vertical load and the out-of-plane (OOP) load are transferred through the umbrella structure producing high stress in the umbrella feet, the arches, and the VV ribs and dome. Analysis based on worst-case PF currents shows that some structures would be over-stressed with peak stresses >1 GPa for NSTX Upgrade parameters.

To eliminate such overloading, the load path will be modified in NSTX Upgrade. First, by adding structural support to transfer outer TF coil load to the VV at clevis connections above and below the midplane combined with upgraded clevises, maximum transfer of the OOP loads to the mid-section of the vessel can occur. Figure 16(*a*) shows the array of 12 supports above the midplane that will provide this load transfer, and an identical set is also used below the midplane. These connections reduce loads on the umbrella structure at the top and bottom of the vessel, but will increase loads in the mid-section of the vessel. Interferences with auxiliary systems and supports constrain the design options and limit the addition of trusses to help sustain the OOP load. Nevertheless, sufficient space exists to create a much sturdier support ring via connections between the TF outer coils as indicated by the toroidally continuous circle of new coil clamps shown in figure 16(*a*). This support ring reduces the pull-out (in-plane) loads, and in combination with the tie bars, transfers much of the in-plane and OOP load to the VV. The support ring also reduces the pull-out (in-plane) radial load at the umbrella structure. Details of the improved clamps and connections of the TF to the VV are shown in figure 16(*b*). These structures are effective at reacting loads from PF currents for both up-down symmetric and asymmetric equilibria. It should be noted that up-down asymmetric currents result in a net twist load which requires an attachment to the VV. The tie bars can take the net twist and also provided adequate OOP support for up-down symmetric equilibria.

The second modification to reduce peak stresses at the umbrella structure involves strengthening the umbrella itself. Figure 17(*a*) shows the outer TF coils (red) connecting to the upper umbrella structure, and figure 17(*b*) shows the reinforcement strips and bolt enhancements that will strengthen the aluminium block structures that connect the TF coils to the umbrella. Further, figure 17(*c*) shows the arch reinforcement ring that will be added to the umbrella, the new legs that will be installed and the improved attachments for the umbrella feet.

Of the 96 equilibrium scenarios used for the engineering design of NSTX Upgrade, the two that generate the largest
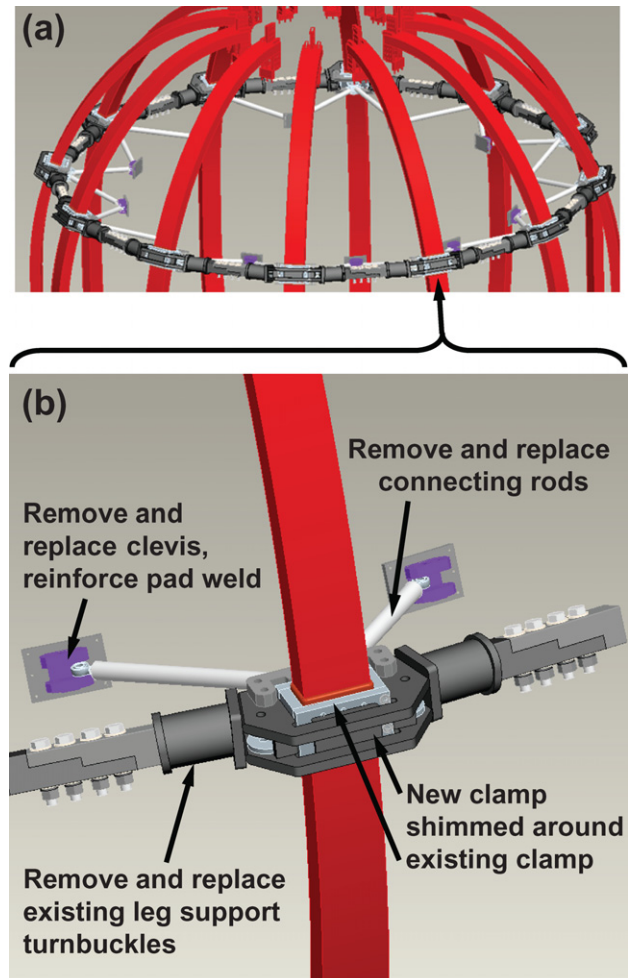
Figure 16. (*a*) Outer TF coils (red) and new upper attachment hardware (gray, silver, purple) and (*b*) new clevises, clevis pads, connecting rods, clamps and turnbuckle replacements used to strengthen the inter-coil support structure and the attachment of the outer TF coils to the NSTX Upgrade vacuum vessel.

OOP forces and torques on the TF outer legs are numbers 34 and 79. These cases correspond to equilibria F (up-down asymmetric) and U (up-down symmetric) in figure 6 with the OH coil supply current at -24 kA, i.e. at the end of the OH coil second swing. In the upper half of the outer TF, the worst-case toroidal forces and torques are 175/180 kN and 320/330 kN m for equilibria F/U, respectively. With the redesigned coil support configuration, the maximum predicted coil stress is 103 MPa and the insulation shear stress is within 11 MPa, and both values are within the allowable values. After reinforcement, the umbrella structure has a maximum stress of 130 MPa, and the peak umbrella arch stress is 85 MPa compared with 304 MPa prior to reinforcement. The stress in the VV is below 106 MPa (within allowable) and has a safety margin factor of 8.5 for nonlinear buckling for scenario 79. The TF support system also maintains the peak stress in the outer TF coil within allowable values for the VV bake-out (150 °C). Lastly, with the redesigned coil support configuration, figure 18 shows the maximum displacement over the entire coil/vessel/umbrella system is limited to 3.1 mm. This is more than 8 times smaller than the 27 mm maximum displacement that would have been
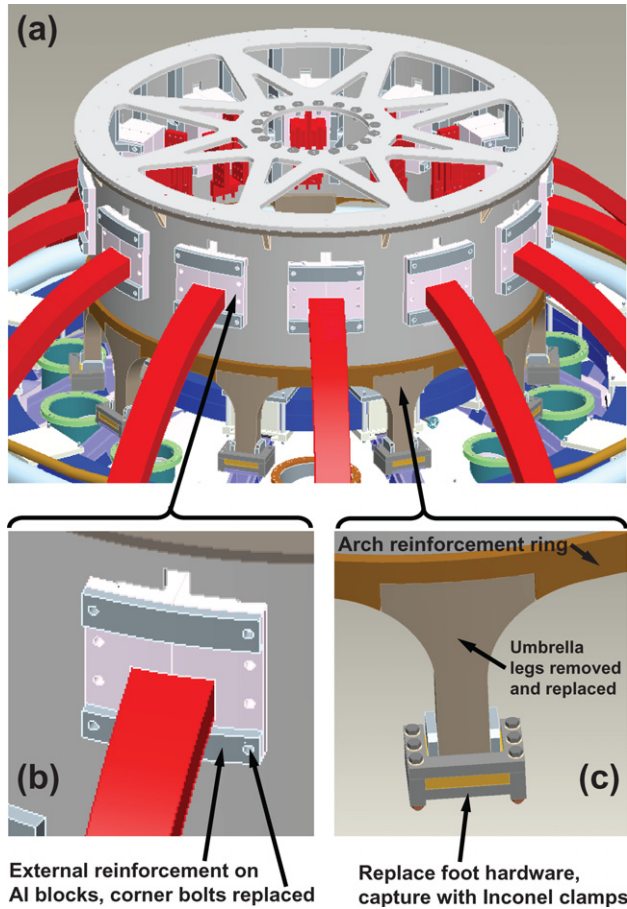
Figure 17. (*a*) Top of NSTX Upgrade showing the cylindrical 'umbrella' structure where the outer TF coils (red) connect to the top of the vacuum vessel, (*b*) reinforcement strips to be attached to the aluminium blocks which connect the TF coils to the umbrella cylinder and (*c*) the new umbrella arch reinforcement ring, new umbrella legs to be welded in place, and new attachments for connecting the umbrella feet to the vacuum vessel.

Figure 18. Exaggerated displacement of the outer TF coils, vacuum vessel, umbrella structure, and other components of NSTX Upgrade resulting from the highest force and torque equilibrium (scenario 79) of the 96 equilibria used for designing the enhancements of the support structures. The colour key in the upper right-hand corner of the figure indicates the displacement in millimetres, and the red arrows on the PF coils indicate the direction of current in the coil.

experienced with the original NSTX support system at full NSTX Upgrade parameters.

2.2.3. 2nd neutral beam injector. Beyond the new CS and ex-vessel structural enhancements, a 2nd neutral beam from TFTR has been chosen to provide the factor of 2 increase in auxiliary heating and current drive power for NSTX Upgrade, as this is presently the most mature and capable technology applicable to ST plasma parameters. The performance parameters of the NSTX neutral beams [105] are provided in figure 19 for reference. Of particular relevance is the decrease in achievable NBI pulse duration (set primarily by the thermal limits of the ion dumps) from 5 to 1.6 s as the beamline power is increased 50% from 5 to 7.5 MW. This decrease highlights the importance of the 2nd NBI for providing sufficient heating power for the pulse lengths expected in the Upgrade. If plasma scenarios with pulse-lengths substantially longer than 5 s become accessible in NSTX Upgrade, additional NBI pulse-length enhancements may be possible by using 'high-hat' ion dumps with two stacked plates (still inertially cooled) to spread the dumped beam ion footprint as originally proposed for the TPX NBI upgrade [106].

The 2nd NBI of NSTX Upgrade not only serves to increase the auxiliary heating power to access reduced ν^*, but also has increased tangency radius of injection R_{TAN}. As described in more detail in section 2.3, increased R_{TAN} is projected to increase the NBICD efficiency and also provide for NBICD profile control. The layout of the new more tangential 2nd NBI next to the present NBI is shown in figure 20(*a*). An important aspect of this layout is the sharing of the beam armor [107] by both NBI systems, as this minimizes the in-vessel surface area taken up by NBI. Achieving increased tangency radius of injection also requires a significant modification to the NSTX vacuum vessel with the cutting of a large opening in the vessel wall for the installation of a new NBI port cap as shown in figure 20(*b*). The NBI port cap required substantial structural analysis and several design iterations to make it compatible with both space constraints and the increased loads on the vessel described in section 2.2.2. The injection radius of the present NSTX NBI has been left unchanged due to space constraints in the NSTX test cell. The more tangential injection of the 2nd NBI on the horizontal midplane on NSTX Upgrade is complementary to the MAST Upgrade [108] approach of adding vertically shifted co-injection NBI sources [109] to achieve more off-axis current drive. Together, the two upgraded devices will thoroughly test off-axis NBICD predictions and will inform the optimal NBI injection geometry for next-step ST devices.

Acceleration Voltage [kV]	MW per Source	MW per Beamline	Pulse Length [s]
65	1.1	3.2	8
70	1.3	3.8	7
75	1.5	4.5	6
80	1.7	5.1	5
85	1.9	5.8	4
90	2.1	6.4	3
95	2.4	7.1	2
100	2.6	7.7	1.5
105	2.8	8.4	1.25
110	3.0	9.0	1
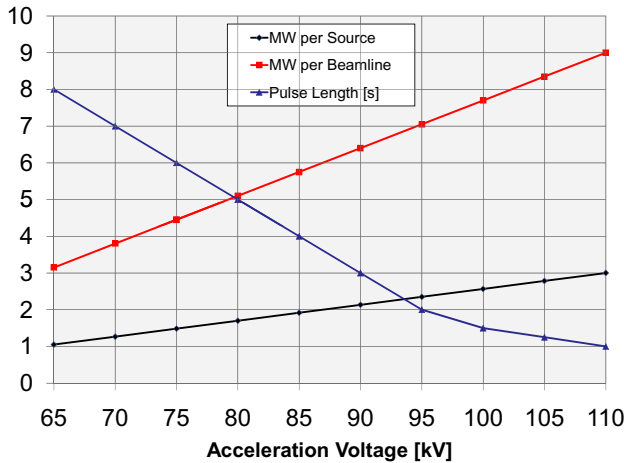
Figure 19. NSTX NBI power per source, power per beamline and nominal maximum pulse-length versus NBI acceleration voltage.

Figure 20. (*a*) Injection geometry of present and new 2nd NBI, and (*b*) modification of the present NBI port to a new NBI port cap to enable the more tangential injection.

The installation of the 2nd NBI also requires substantial floor space in the NSTX test cell, and a major task of the NSTX upgrade outage involves removing and relocating several diagnostics and associated racks to make room for the 2nd NBI. As shown in figure 21, once the 2nd NBI is installed next to the present NBI, most of the available floor space within the test cell will be occupied by NSTX Upgrade and NBI systems. It should also be noted that the 2nd NBI to be used on NSTX Upgrade was used during the D–T experiments on TFTR and was contaminated with tritium. The decontamination of this beam line was successfully completed in 2010 in preparation for usage on NSTX Upgrade, and reassembly of the 2nd NBI was initiated in 2011.

2.3. Non-inductive current formation and sustainment

A critical element of ST research in support of steady-state operation is to increase the 65–70% non-inductive fraction sustained in NSTX [65, 66, 79] to full non-inductive sustainment. Future ST-FNSF facilities are projected to rely heavily on NBICD to drive as much as 50% of the plasma current with the remainder provided by bootstrap current. NBICD is also presently envisioned to provide the heating and current drive for non-inductive plasma current ramp-up. Reduced collisionality in NSTX Upgrade will help increase the NBICD efficiency to increase the non-inductive fraction, but additional current drive is still required. NSTX Upgrade will rely heavily on the 2nd NBI system discussed in section 2.2.3 (also injecting in the co-plasma-current direction) to increase the externally applied non-inductive current drive. An
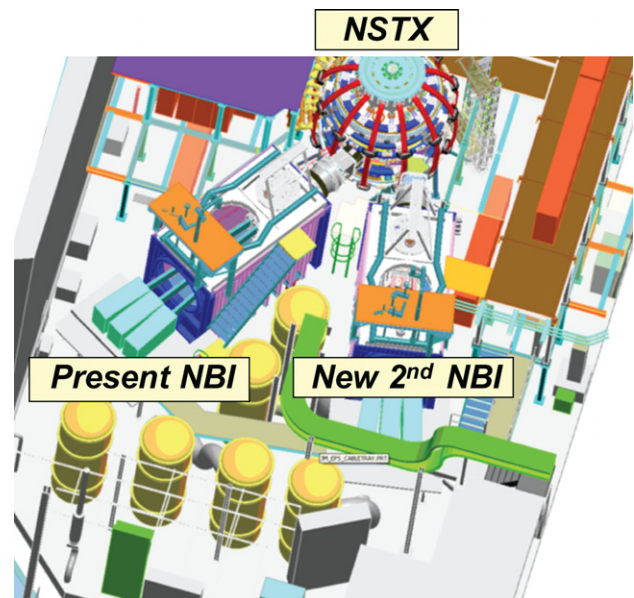
Figure 21. Drawing of top-down view of layout of NSTX test cell after installation of new 2nd NBI.

overview of non-inductive sustainment calculations for NSTX Upgrade is provided in section 2.3.1, and a comprehensive analysis of NSTX Upgrade equilibrium scenarios using free-boundary TRANSP calculations is provided in [55].
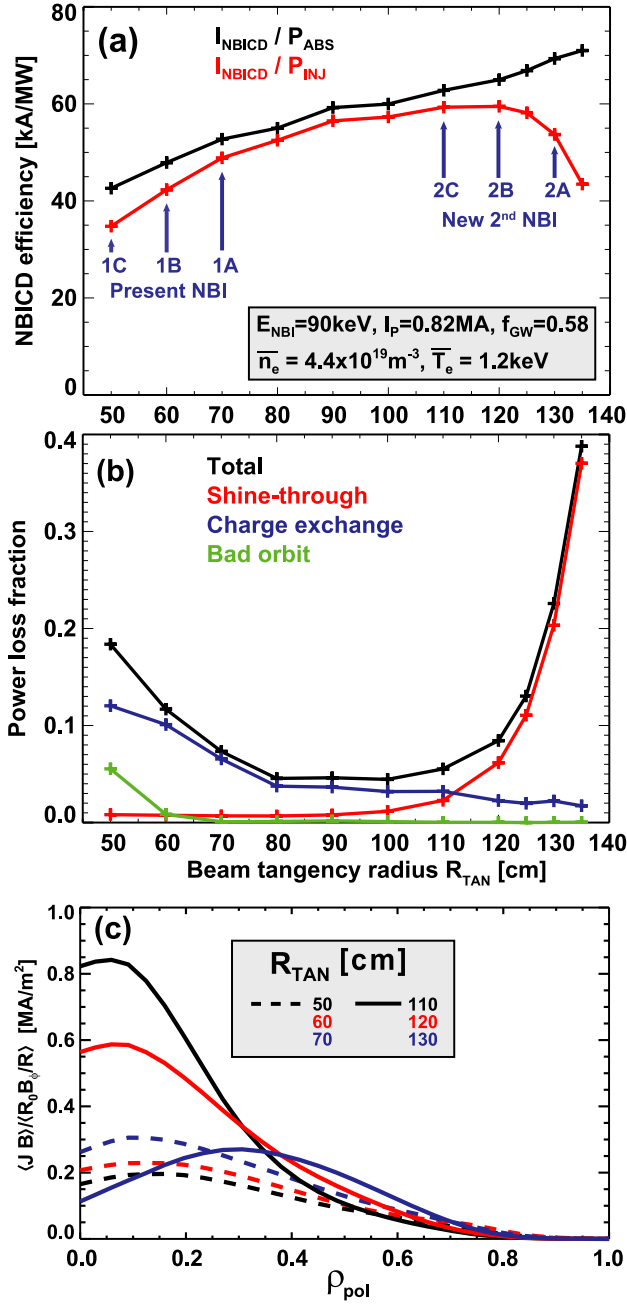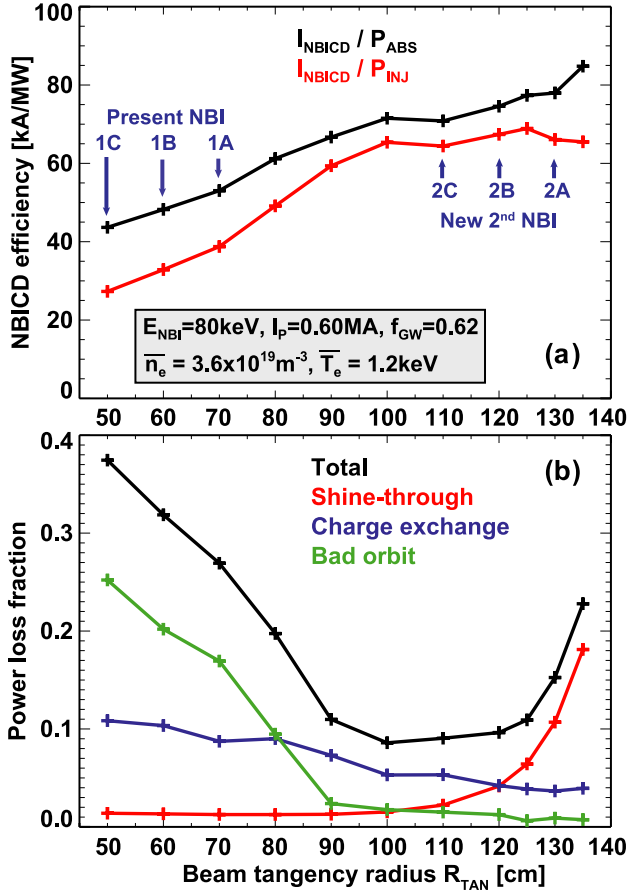
Figure 22. (*a*) NBICD efficiency (kA MW^{-1}) and (*b*) power loss fractions (total, shine-through, charge exchange and bad orbit) as a function of beam tangency radius R_{TAN}, (*c*) NBICD parallel current density profiles versus minor radius for the tangency radii of the present (dashed) and new 2nd NBI (solid) for an $A = 1.45$, $I_P = 0.82$ MA, $B_T = 0.55$ T NSTX target plasma with a 13 cm outer gap.

2.3.1. Plasma sustainment with NBI heating and current drive. The 2nd NBI of NSTX Upgrade not only serves to increase the auxiliary heating power to access reduced ν^*, but also has increased tangency radius of injection R_{tan}. The increased tangency radius of injection increases the NBICD efficiency by depositing fast-ions on-average more parallel to the magnetic field since $v_{\parallel}/v = (R_{TAN}/R)|B_{\phi}/B|$ [110], but also depends on details of the target plasma and NBI deposition profile. Figure 22 shows TRANSP calculations of the NBICD

efficiency versus R_{TAN} for a representative NSTX target plasma with $A = 1.45$, $\kappa = 2.45$, $I_P = 0.82$ MA, $B_T = 0.55$ T, line-average density $= 4.4 \times 10^{19}$ m^{-3}, Greenwald density fraction $= 0.6$, line-average $T_e = 1.2$ keV and outboard plasma-limiter gap of 13 cm. This reference plasma condition is included in these studies to ensure that the new 2nd NBI will also be effective at heating and driving current for NSTX-like field, current, collisionality, and gap values in support of NSTX Upgrade physics studies that may wish to access plasma parameters similar to those of the original NSTX (except aspect ratio).

Figure 22(*a*) shows that the absorbed current drive efficiency I_{NBICD}/P_{ABS} increases by a factor of 1.65 as the tangency radius is increased from that of the least tangential source ($R_{TAN} = 50$ cm) of the present NBI to the most tangential source ($R_{TAN} = 130$ cm) of the new 2nd NBI. The NBI power loss is also a function of tangency radius, and figure 22(*b*) shows that for small R_{TAN}, the more perpendicular injection increases the number of particles that are promptly lost (i.e. bad orbits). Small R_{TAN} also increases the fraction of particles with orbits that spend time in the gap between the plasma and first-wall and this trend increases charge exchange losses. Figure 22(*b*) also shows that large R_{TAN} can lead to increased power losses due to increased shine-through. This is caused by the decrease in NBI path-length intersecting the plasma when R_{TAN} is large, and this results in decreased beam ionization and absorption. Thus, while the largest R_{TAN} has the highest current drive efficiency for power absorbed, the injected power current drive efficiency I_{NBICD}/P_{INJ} is highest for $R_{TAN} = 120$ cm for these equilibrium conditions. Overall, the current drive efficiency for injected power is at least 40% higher for the new 2nd NBI compared with the present NBI.

An additional important capability for optimization of stability and confinement is control of magnetic safety factor profile. Thus, for NBI as the primary external current drive source, variation of the NBICD deposition profile is needed. For the current drive and loss power conditions shown in figures 22(*a*) and (*b*), figure 22(*c*) shows that the NBICD profile depends only weakly on R_{TAN} for the present NBI ($R_{TAN} = 50, 60, 70$ cm). In contrast, for the more tangential injection of the 2nd NBI in the Upgrade, $R_{TAN} = 110, 120, 130$ cm can vary the injected NBICD parallel current density from strongly centrally peaked to peaked off-axis, and this capability can potentially be exploited for improved control of the q profile.

In the NBICD analysis shown in figures 22, 23, and 24, the ion and electron temperature and electron density profiles are simply linearly scaled from the profiles of NSTX shot 116313 which had a high non-inductive current drive fraction of 60–70% that was sustained for multiple current redistribution times. This shot was previously investigated using the TSC [111] code to simulate extension of this high non-inductive fraction scenario to a fully non-inductive scenario [112], and the plasma profiles are shown in [112]. This shot was also used for validating the NBI, bootstrap, and ohmic current drive profile models in TRANSP for NSTX conditions [65]. For shot 116313, the profile peaking factors (peak/volume-average) are $T_i(0)/\langle T_i \rangle = 1.64$, $T_e(0)/\langle T_e \rangle = 1.66$, $n_e(0)/\langle n_e \rangle = 1.56$, $p_{th}(0)/\langle p_{th} \rangle = 2.15$, $p_{tot}(0)/\langle p_{tot} \rangle = 2.96$, and the ratio of volume-average T_i to volume-average T_e is 1.25.

Figure 23. (*a*) NBICD efficiency (kA MW^{-1}) and (*b*) power loss fractions (total, shine-through, charge exchange and bad orbit) as a function of beam tangency radius R_{TAN} for an $A = 1.65$, $I_P = 0.60$ MA, $B_T = 0.9$ T NSTX Upgrade target plasma with a 7.4 cm outer gap.

Generally, these peaking factors are somewhat higher than for the TRANSP simulations of NSTX discharges shown in table 1. The Z_{eff} profile for shot 116313 is near 2 in the core and edge, is near 1.6 at the mid-radius and has a volume-average of 1.8. Toroidal rotation is not included in the TRANSP simulations shown in figures 22–24. All TRANSP calculations shown here assume no anomalous diffusion of fast-ions is present, i.e. the slowing-down is classical. Previous NSTX studies have shown that the anomalous fast-ion diffusion can range from being small in the absence of core MHD and Alfvénic instabilities to causing a substantial reduction in fast-ion stored energy and neutron rate and redistributing the beam-driven current [65, 66, 113, 114]. The effects of anomalous fast-ion diffusion on NSTX Upgrade NBICD is discussed in more detail in [55].

It should be noted that the shine-through loss of the largest R_{TAN} source can be a sensitive function of the line-average density and especially the outboard plasma-limiter gap. For example, figure 23 shows that for a representative NSTX Upgrade plasma with $A = 1.65$, $\kappa = 2.6$, $I_P = 0.6$ MA, $B_T = 0.9$ T, line-average density $= 3.6 \times 10^{19}$ m^{-3}, Greenwald density fraction $= 0.6$, line-average $T_e = 1.2$ keV and reduced outboard plasma-limiter gap of 7.4 cm, the $R_{TAN} = 130$ cm shine-through loss power fraction decreases from 20% to 10% and the injected power CD efficiency
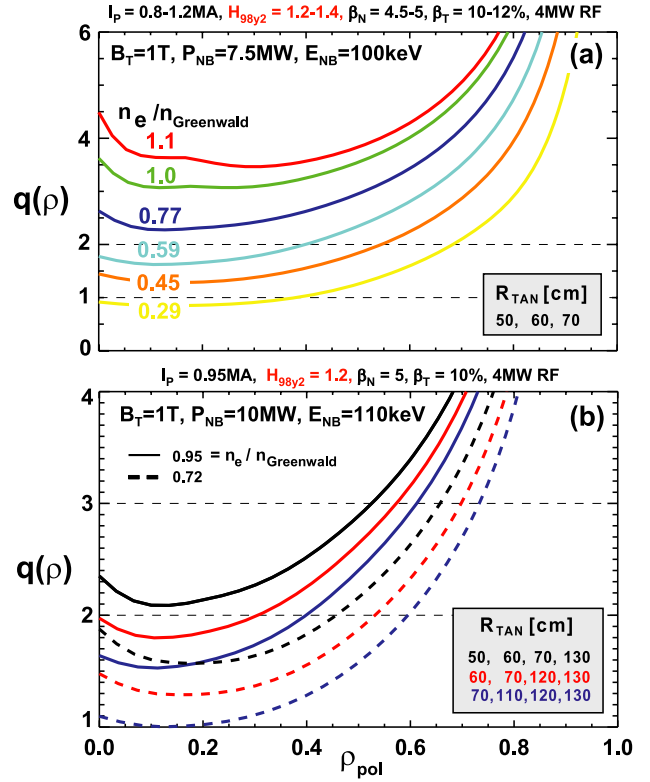
Figure 24. (*a*) Comparison of parallel current density profiles for existing (dashed) and 2nd (solid) NBI sources and q profile controllability versus density for (*b*) existing and (*c*) additional NBI sources for NSTX Upgrade target plasmas with $A = 1.65$–1.7, $\kappa = 2.6$–2.7, and outer gap $= 7.5$ cm.

becomes the same as the $R_{TAN} = 110$ and 120 cm efficiencies. This decrease in shine-through even for lower line-average density implies the decreased outer gap is playing an important role in increasing the absorption efficiency. For these equilibrium conditions, figure 23(*b*) shows that the bad-orbit losses increase to 20–25% for the small R_{TAN} values of present NBI configuration presumably due to lower plasma current and despite the higher toroidal field. Further, the injected power current drive efficiency of the new 2nd NBI becomes a factor of two higher than for the present NBI. Thus, a representative range for the overall increase in current drive efficiency for the new 2nd NBI relative to the present NBI is 1.4–2. It is also apparent that the 2nd NBI is much better confined at reduced I_P, and this improved capability will be important for non-inductive ramp-up studies as described in section 2.3.7 Additional information on the NSTX Upgrade scenario dependence on outer gap and NBI source can be found in [55].

Next we consider fully non-inductive equilibrium scenarios for NSTX Upgrade with $A = 1.65$–1.7, $\kappa = 2.6$–2.7 and outer gap $= 7.5$ cm. As shown in figure 24(*a*), using only the existing NBI with the CS upgrade, full-power NBI (7.5 MW) + 4 MW of high-harmonic fast-wave (HHFW) heating is needed to support 100% non-inductive operation, and the only means of q control is q_{min} variation through the plasma density (i.e. CD efficiency). In particular, since the NBICD efficiency varies as T_e/n_e, increased density at fixed confinement multiplier and β quickly reduces the NBICD

which lowers the total plasma current which increases q and the bootstrap fraction which in turn elevates q_{min}. It should be noted that the $n_e^{0.4}$ dependence of the ITER H-mode confinement scaling tends to increase the projected thermal confinement at higher density which increases the bootstrap current and partially offsets the loss of NBICD at higher density. Nevertheless, such scenarios require $H_{98} = 1.2$–1.4 and would be limited to 1.6 s duration by NBI ion dump operating limits as described in section 2.2.3. $H_{98} = 1.3$–1.7 has been achieved transiently in NSTX, but sustaining $H_{98} = 1.15$–1.2 is only now beginning to be achieved with Li conditioning [115] in ELM-free conditions in NSTX with a goal of extending this enhanced confinement to small-ELM regimes. With the addition of the 2nd NBI of the Upgrade, figure 24(*b*) shows that higher NBI power (10 MW versus 7.5 MW) can reduce the required confinement to $H_{98} = 1.2$ for 100% non-inductive scenarios and also enables control of q_{min} with $\Delta q_{min} = 0.6$ by varying the NBI source mix at fixed density. Further, scenarios with $n_e/n_{Greenwald} = 0.7$–1 exist with q_{min} varying from 1 to above 2 with important implications for stability and transport research. All of the above scenarios operate above the $n = 1$ no-wall stability limit and require stabilization of the resistive wall mode (RWM) as is common for advanced scenarios on NSTX [42].

Developing a scenario based on simple linear scalings of fixed profile shapes taken from an experiment may be sufficient for computing NBI and bootstrap currents and current-drive fractions, but such scaling can lead to other difficulties in transport analysis and interpretation. In particular, in some high density scenarios, the computed ion thermal diffusivity (χ_i) can become lower than the neoclassical value (χ_{i-nc}) and can even become negative. This typically happens near the plasma edge where the ion-electron collisional heating of electrons is strongest due to the lower plasma temperature near the edge. The simulations shown in figure 24(*b*) all have $\chi_i/\chi_{i-nc} > 1$, and only near the edge ($\rho_{pol} > 0.8$) is $\chi_i/\chi_{i-nc} \approx 1$ for the $f_{GW} = 0.95$ scenarios. However, for the scenarios using only the existing NBI heating shown in figure 24(*a*), $\chi_i/\chi_{i-nc} \approx 1$ for $f_{GW} \approx 0.8$, but χ_i can become negative for $f_{GW} \geqslant 0.85$ for $\rho_{pol} > 0.7$.

To avoid unphysical ion thermal diffusivity profiles, and to utilize an ion thermal transport model more directly related to neoclassical transport [16], more recent TRANSP simulations [55] constrain the ion thermal diffusivity to be a multiple of the neoclassical diffusivity thereby removing the possibility of a negative χ_i. Such TRANSP calculations have been carried out for 100% non-inductive current drive using all six NBI sources at 1 MA and 1 T and by optimizing the outer gap to optimize the current drive profile. As shown in figure 25(*a*), 100% non-inductive current drive (indicated by the white line) is possible for a wide range of normalized density values with confinement multiplier $H_{98} = 1$–1.05 at $A = 1.73$, $\kappa = 2.7$ and outer gap $= 10$ cm. As shown in figure 25(*b*), q_{min} can be varied from values near 1 (indicated by the white line) to above 3 by varying the normalized density. Further, the q_{min} values can be increased well above 2 by operating at high normalized density with important implications for RWM stability and for avoiding $m/n = 2/1$ neoclassical tearing modes.

Figure 26 shows several profiles for the $H_{98} = 1.03$, $f_{GW} = 0.72$ TRANSP equilibrium simulation in figure 25.
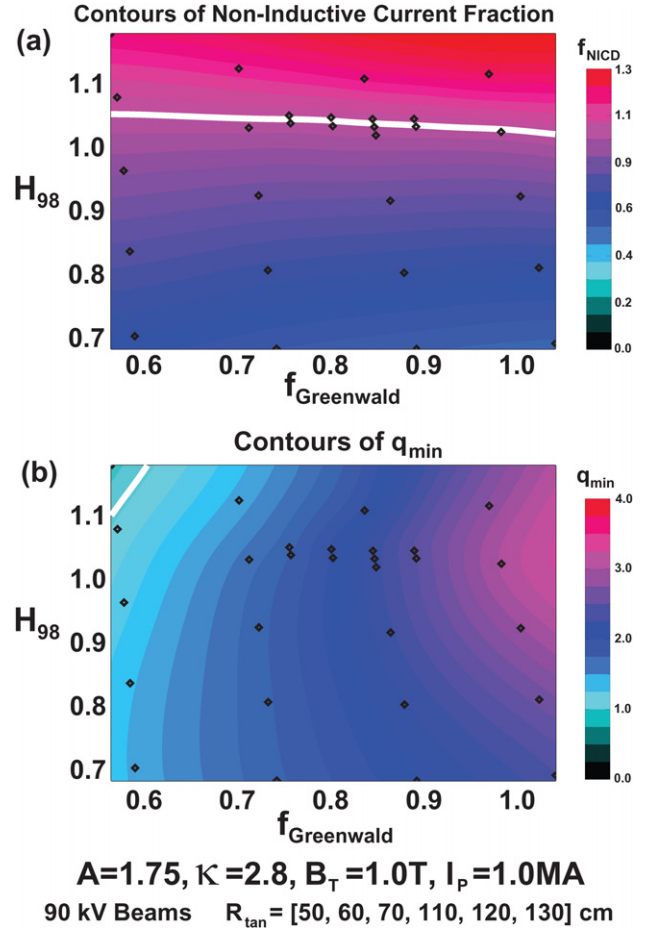
Figure 25. Contours of (*a*) non-inductive current fraction and (*b*) minimum safety factor q_{min} versus $f_{Greenwald}$ and ITER H-mode confinement multiplier H_{98} for 1 MA plasmas with 12 MW of NBI heating.

This scenario has 100% non-inductive current fraction at $I_P = 0.975$ MA and has parameters most similar to the NSTX-U 100% NICD scenarios in table 1. As shown in figure 26(*a*), the central ion temperature $T_i(0)$ is projected to be over 2 keV and $T_e(0) = 1.4$–1.5 keV. In these simulations, the T_e and n_e profiles are scaled from an NSTX plasma (shot 142301) with aspect ratio $A \geqslant 1.7$ [55, 56] prototypical of NSTX Upgrade. The impurity species is C^{6+} and Z_{eff} is chosen to be a spatially constant value of 2.0. The chosen Z_{eff} profile together with the n_e profile in figure 26(*b*) determine the deuterium density profile n_D. The T_i profile is determined by constraining the ion thermal diffusivity profile χ_i to be a multiple (factor of 2 in this case) of the TRANSP NCLASS [116] neoclassical thermal diffusivity χ_{i-nc} as shown in figure 26(*c*). The T_e profile is scaled to match the overall global confinement constraint, in this case $H_{98} \approx 1$. As is evident from figure 26(*c*), the electron thermal diffusivity χ_e is comparable to χ_i in the edge/pedestal region $\rho_{pol} \geqslant 0.9$ but is a factor of 2–10× higher than χ_i in the core region consistent with previously reported NSTX thermal diffusivity profile trends [16]. figure 26(*d*) shows the parallel current density profile $J_{||} \equiv \langle \vec{J} \cdot \vec{B} \rangle / \langle B_\phi R_0 / R \rangle$ including the total (black), NBICD (blue), bootstrap current (red), and ohmic/inductive (green) components. Figure 26(*e*) shows that this current density profile results in a q profile with
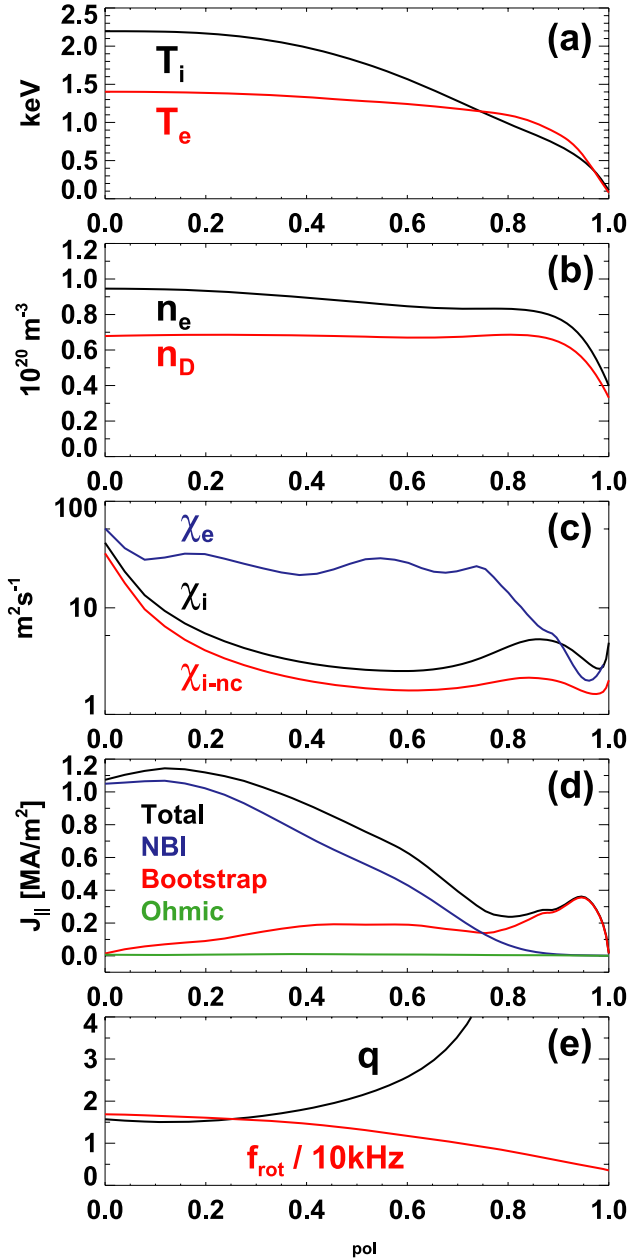
Figure 26. Profiles of (*a*) ion and electron temperature (T_i, T_e), (*b*) electron and deuterium density (n_e, n_D), (*c*) electron and ion thermal diffusivity (χ_e, χ_i), (*d*) parallel current density ($J_{||}$) including inductive/ohmic and non-inductive components and (*e*) effective charge and safety factor (Z_{eff}, q), for a TRANSP simulation of a 100% non-inductive NSTX Upgrade plasma with $I_P = 0.975$ MA and $B_T = 1$ T.

$q_{min} \approx 1.5$. The toroidal rotation angular frequency profile used in this simulation is taken from the NSTX experimental profile and is also shown in figure 26(*e*) and has a central maximum value of 17 kHz. The rotation scalings discussed in section 2.1.3 and table 1 suggest the toroidal rotation could be approximately a factor of two higher in NSTX Upgrade. High rotation values up to 30–40 kHz have previously been reported for NSTX [78, 117], and the impact of possible increased toroidal rotation on NSTX Upgrade scenarios is a topic for future research.

2.3.2. High bootstrap fraction scenarios. Beyond the potential usage of the ST for an FNSF, an important issue for both the AT and ST as potential Demo candidates is efficient current sustainment—in particular the achievement of scenarios with very high bootstrap fraction. As is well known, high bootstrap fraction combined with high β and confinement can substantially reduce the need for external non-inductive current drive and minimize the cost of electricity in fusion power plants [104, 118, 119]. However, the ability to access and control scenarios with simultaneous high confinement, high β, and high bootstrap fraction remains an important goal in tokamak/ST research. High confinement combined with high bootstrap fraction has been achieved with strongly reversed shear 'current hole' scenarios [120] in which an edge transport barrier (H-mode) is combined with an internal transport barrier to achieve $H_{98} = 1.5$–2 including scenarios which do not use the central solenoid [121] and are therefore relevant to STs.

NSTX L-mode plasmas with reversed shear and heated with a combination of NBI and HHFW have produced core electron and ion transport barriers [122] with improved core confinement. However, such scenarios have not yet been combined with H-mode, as inducing H-mode in the presence of an ITB often leads to MHD instabilities (such as double tearing modes) which destroy the core transport barrier. Additional scenario development is needed to achieve combined edge and core transport barriers, and increasing the safety factor by doubling the toroidal field in NSTX Upgrade could potentially reduce MHD instabilities.

Alternatively, enhanced pedestal confinement scenarios [115] in NSTX have achieved the high confinement ($H_{98} = 1.7$) conducive to high bootstrap fraction, and these scenarios will also be further explored in NSTX-U. Further, it is noted that if the ST-specific confinement scaling predictions are realized at full toroidal field in NSTX-U, this alone may be sufficient to achieve high confinement and bootstrap fraction. In particular, as shown in the right-most orange columns of table 1, if the NBI power is reduced to 2 MW (to minimize NBI-CD while still driving toroidal rotation and $E \times B$ shear to suppress ion turbulence) and is combined with 2 MW of HHFW heating, high bootstrap fractions of 89–97% are projected to be possible for a range of Greenwald fractions = 0.5–1 using this simple 0D analysis. Such scenarios would have high $H_{98} \approx 2$ and high $\beta_N > 5$ but low (relative to ST Demo requirements) $\beta_t \approx 10\%$ due to high $q^* \approx 7$. Given that such scenarios are far from those realized thus far on NSTX or MAST, substantial scenario modelling and experimental development will be needed to access very high f_{BS}. The $f_{GW} = 0.77$–1.0 equilibria of figure 24(*a*) with $H_{98} = 1.3$–1.4 (1.5–1.6 without HHFW), $I_P = 0.9$–1 MA, and $f_{BS} = 0.8$–0.9 provide example TRANSP calculations of such scenarios. Further, it should be noted that if one assumes an ITER-like confinement scaling and operates with $H_{98} \approx 1.1$ and $f_{Greenwald} = 1$, i.e. in the upper right corner figure 25(*b*), fully non-inductive scenarios are predicted to be achievable with $f_{BS} > 75$–80% [55]. If such scenarios were achieved in NSTX Upgrade, they would provide a good starting point for attempting to extend ST operation to $f_{BS} = 80$–95%.

2.3.3. High-harmonic fast-wave heating in NBI H-mode scenarios. HHFW can be an effective electron heating method for ST plasmas as evident from the fact that the highest central electron temperatures in NSTX have been achieved using HHFW. In particular, $T_e(0)$ up to 5.2 keV has been achieved in deuterium and $T_e(0)$ up to 6.2 keV in helium RF-heated L-mode plasmas [123]. With respect to HHFW heating and current drive in NBI-heated H-mode plasmas, it should be noted that the central electron temperature has been increased by as much as 60% (to $T_e(0) \approx 1.9$ keV) using 1.8 MW of HHFW in $P_{NBI} = 2$ MW NBI-heated H-mode plasmas [123]. Lithium wall conditioning was an important element in achieving these results by reducing the plasma density in front of the antenna which reduces surface wave excitation losses [123, 124]. Approximately 2/3 of the injected HHFW power was coupled to the core plasma using heating $(0–\pi)$ phasing of the antenna straps. Thus, coupling 4 MW to the plasma core will require operating at an antenna power of 6 MW which is near the antenna voltage standoff limits. Operating at high HHFW power also requires a relatively small plasma-antenna gap (3–5 cm) to provide sufficient antenna loading, and improved RF limiters will be needed in NSTX Upgrade to dissipate increased limiter heating from higher HHFW and NBI power and increased pulse-length.

While heating an NBI H-mode plasma with HHFW does appear technically feasible, HHFW current drive is expected to have low efficiency in NSTX Upgrade NBI H-mode plasmas (except possibly close to the magnetic axis) [125]. Specifically, the HHFW current drive efficiency is: $I_{CD}(kA)/P_{RF}(MW) \approx 1.5T_e(keV)/n_e(10^{20} m^{-3})$ obtained from previous NSTX measurements and simulations [125, 126] is relatively low due to strong electron trapping effects and results in small current drive = 2–20 kA for 4 MW of HHFW heating for the scenarios in table 1. Absorption of HHFW power by NBI fast-ions [127] further reduces HHFW current drive efficiency, as does the excitation of surface waves with current drive phasing [124]. Thus, it is expected that the only substantial additional bulk current drive in predominantly NBI-heated H-modes in NSTX Upgrade will come from the new 2nd NBI.

2.3.4. Particle control. As shown in figures 24 and 25, the electron density is a strong determinant of the expected NBICD efficiency, the non-inductive current fraction, and the expected value of minimum q. Thus, density control will be important for optimizing and controlling high non-inductive current-drive fraction scenarios (and other scenarios) in NSTX. Lithium coatings of the internal PFCs have been shown to pump hydrogenic species, improve confinement, and suppress ELMs in NSTX plasmas [99, 128]. Recently, control of the deuterium ion inventory to equivalent Greenwald fraction (ignoring impurities) as low as 0.3 has been achieved and sustained for up to 1.4 s (limited by magnet heating) using Li coatings in NSTX. However, with strong lithiumization and in the absence of ELMs, carbon impurity accumulation can occur which increases the total (D^+ and C^{6+}) $Z_{eff} \leqslant 4$ corresponding to a Greenwald fraction of up to 0.8.

The combination of lithium coatings with ELMs triggered by externally applied $n = 3$ non-axisymmetric field pulses [99, 129] has successfully reduced the carbon accumulation and lowered the Z_{eff} to 3 or below corresponding to a minimum Greenwald fraction of 0.5–0.7. This range of achievable minimum Greenwald fraction is acceptable for optimizing the NBICD of NSTX Upgrade scenarios for pulse durations of perhaps 2–3 s, but it is unclear if lithiumization combined with triggered ELMs will extrapolate to 5 s pulses and higher heating powers of NSTX Upgrade. Measurements of plasma confinement and beta limits and short-pulse assessments of heat-flux mitigation techniques could be performed with only 2–3 s of particle control duration in NSTX Upgrade. However, if insufficient particle control leads to MHD instabilities and/or density limit disruptions after 2 s, several of the scenarios in table 1 would be adversely affected. In particular, the long-pulse scenario would not exist, the 'Max I_P' scenario would have only 1 s of I_P flat-top and would not achieve current profile equilibration, and the scenarios that assume ST confinement would have current flat-tops of only 1–2 current redistribution times and would not achieve current profile equilibration.

A liquid lithium divertor (LLD) [130–133] has been tested in NSTX with a goal of assessing the ability of thicker layers of liquid lithium to extend the deuterium pumping duration relative to thin layers of solid lithium, and conceptual designs for divertor cryo-pumping systems will also be pursued for NSTX Upgrade. Such divertor particle pumping systems are not presently included in the scope of the NSTX Upgrade Project and would therefore likely be implemented following completion and initial usage of the new CS and second NBI. If particle control is achieved in NSTX Upgrade using lithium coatings, a LLD, paced ELMs, and/or cryo-pumping, improved fuelling control will likely be needed. For improved fuelling control, supersonic gas injection (SGI) [134] can provide efficient and controllable edge fuelling, central fuelling with deuterium pellets [135–138] is an option, and compact toroid (CT) injection has been proposed for NSTX [139] as a means of core particle fuelling and momentum injection with application to NSTX Upgrade, ITER, and other next-step facilities.

2.3.5. Overview of non-inductive current formation and ramp-up. To achieve low aspect ratio and small device size, future ST-FNSF facilities are anticipated to operate without a central solenoid, making non-inductive ramp-up (with reliance on NBI heating and CD) a critical element of ST research. Present NSTX research is pursuing non-inductive formation of plasma current using CHI [140] to form a closed-flux plasma of 0.2–0.3 MA to be heated and sustained by high-harmonic fast-waves in a high bootstrap-current-fraction H-mode plasma. Promising HHFW heating and current drive results have recently been obtained [141] in low-current ($I_P = 300$ kA) ohmic target plasmas being developed as plasma current ramp-up targets for NBI. In these plasmas, an HHFW-induced H-mode with a central electron temperature of up to 3 keV was achieved with 65% non-inductive current drive ($f_{BS} = 43\%$, $f_{RFCD} = 22\%$) with 1.4 MW of injected HHFW power. The time evolution and density and temperature profiles for this plasma are shown in figure 27. These results extend previous results [112] by driving similar levels of non-inductive current (≈ 200 kA) with half the injected power (1.4 MW versus 2.8 MW) and are due in part to an upgrade of the HHFW antenna from a single to double-end-fed configuration [123] which enabled HHFW
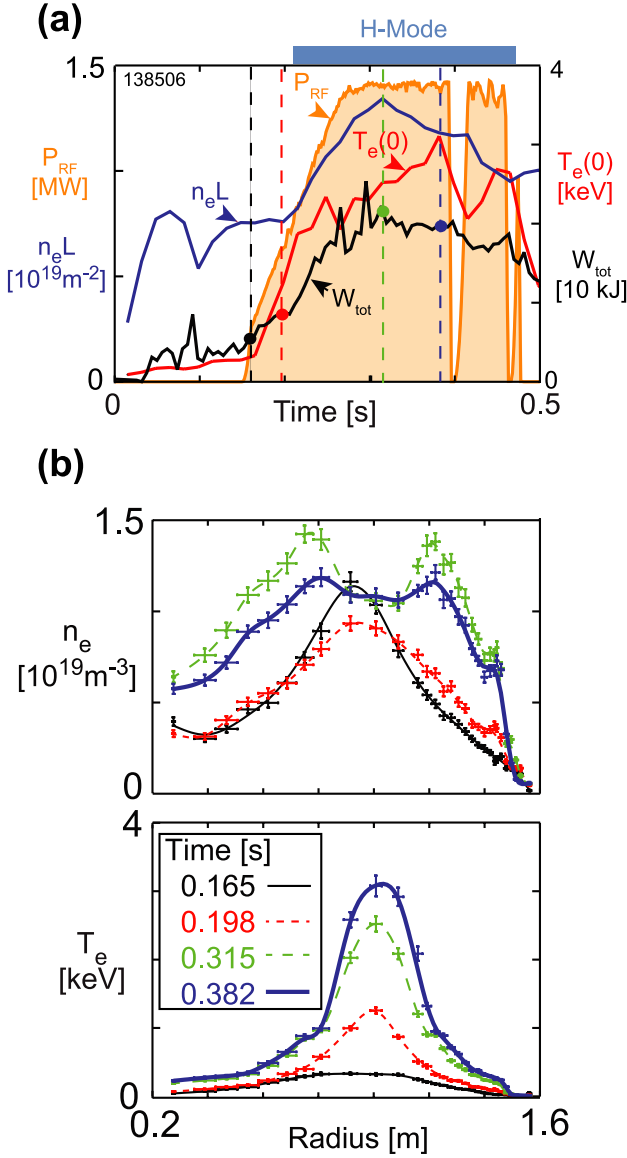
(a)

Figure 27. (*a*) Time evolution of n_eL, $T_e(0)$, W_{tot} and P_{RF} for an $I_P = 300$ kA, $B_T = 0.55$ T HHFW deuterium H-mode (shot 138506) using $k_\phi = -8$ m^{-1} RF heating, (*b*) n_e and T_e profiles show the development of an H-mode pedestal as the RF power is ramped up followed by an increase of $T_e(0)$ up to 3 keV at $t = 0.382$ s.

coupling to be maintained through the L–H transition and during ELMs. Further, these results project to $\geqslant 100\%$ non-inductive current drive at 300–400 kA with 3–4 MW of injected HHFW power and support a major research goal of NSTX Upgrade which is to assess whether plasmas formed with helicity injection (see section 2.3.6) and heated with HHFW (and possibly ECH/EBW [142, 143]) can form a suitable target for current ramp-up using NBI heating and current drive as described in section 2.3.7.

2.3.6. CHI plasma formation. CHI on NSTX is implemented by injecting current from an external circuit through a plasma arc formed along a combined poloidal and toroidal magnetic field that connects the lower inner and outer divertor plates. NSTX uses the lower divertor plates as the injector electrodes
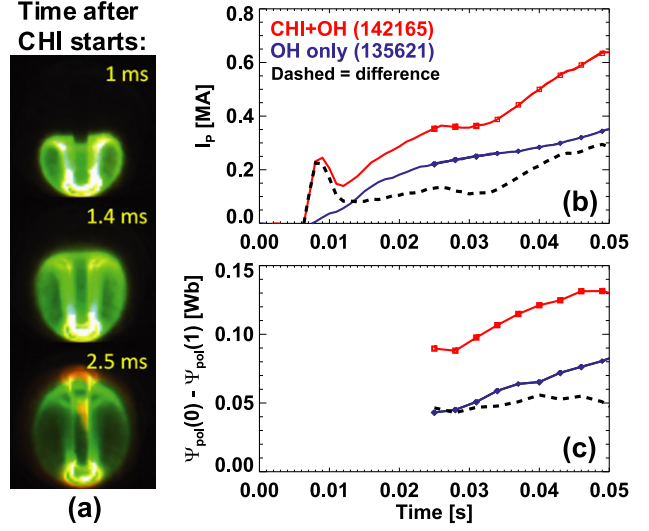
Figure 28. (*a*) Evolution of CHI plasma boundary light shortly after plasma formation, (*b*) plasma current savings and (*c*) poloidal flux savings from CHI coupled to induction in NSTX start-up plasmas.

with the upper divertor plates acting (and referred to) as the absorber. At sufficiently high poloidal CHI injector current, the plasma current self-force accelerates the plasma away from the injector region into the vacuum chamber and towards the absorber region. Figure 28(*a*) shows the rapid growth of the CHI plasma emerging from the lower divertor and filling the NSTX vacuum chamber in less than 3 ms. As shown in figure 28(*b*), CHI has been successfully coupled to high-confinement inductively-driven plasmas [144, 145] with an early current savings of 150–200 kA relative to OH-only start-up. As shown in figure 28(*c*), this corresponds to plasma poloidal flux formation by CHI of 50 mWb. The plasmas compared in figure 28 are chosen to have a similar shape and l_i evolution to illustrate the current and flux savings from CHI.

The initial PF connecting the inner and outer divertor plates in the injector region is produced using the lower divertor coils as shown in figure 30(*a*). To produce a CHI start-up plasma that is accelerated away from the injector into the main NSTX vacuum chamber, the injector current I_{inj} must exceed the 'bubble burst' threshold current [140] I_{bb}:

$$I_{inj} \geqslant I_{bb} = 2\psi_{inj}^2/(\mu_0^2 d^2 I_{TF}). \qquad (1)$$

Here ψ_{inj} is the poloidal flux at the injector insulating gap, I_{TF} is the total current in the toroidal field coil and d is the width of injector flux footprint on the electrodes. It can also be shown that the toroidal current generated for a given amount of injector current has a limiting value equal to the ratio of the toroidal flux enclosed by the ST limiter boundary Φ_T to the injector poloidal flux:

$$I_P/I_{inj} \leqslant M \equiv \Phi_T/\psi_{inj}. \qquad (2)$$

Experiments from HIT-II [146] have shown that the scaling relations in equations (1) and (2) are generally consistent with the experimental results. Figure 29 shows the results of a scan in HIT-II in which the injector flux and current (green triangles) and toroidal field B_T (blue diamonds) are all increased to increase the plasma current (red squares).
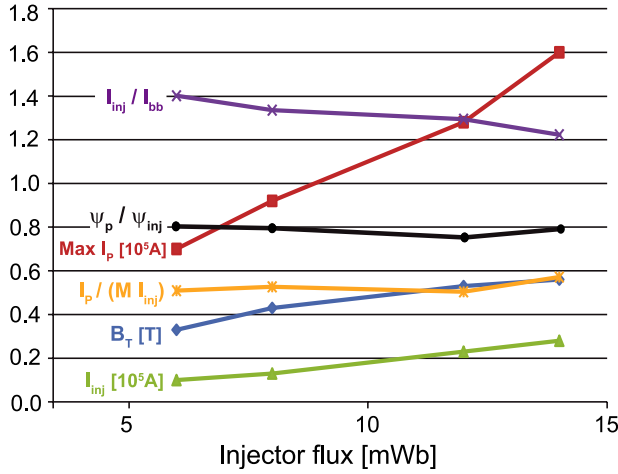
Figure 29. Parameters from HIT-II transient CHI start-up experiments plotted as a function of injector poloidal flux.

Figure 29 shows that the maximum toroidal plasma current achieved in the scan was 160 kA which corresponds to 100 kA of closed-flux current based on the measured toroidal current at the time of zero injector current. The ratio I_{inj}/I_{bb} (purple multiplication signs) is observed to be in the range 1.4–1.2 (i.e. $\geqslant 1$ as required), and the flux amplification [147] which is the ratio of closed poloidal flux to injector flux $= \psi_p/\psi_{inj}$ (black circles) is approximately 0.8. In the calculation of I_{bb}, the flux footprint width $d = 11$ cm is 20% higher than the minimum value in HIT-II of 9 cm [148] and is a function of device CHI injector geometry. The ratio $I_P/M I_{inj}$ (orange stars) is approximately 0.5 and is consistent with the inequality in equation (2). For reference and comparison, NSTX transient CHI discharges have achieved $I_P/M I_{inj}$ ratios as high as 0.7–1 [149].

To extend the scaling results obtained in HIT-II and NSTX, TSC simulations have been performed and show reasonable agreement with the relations above. The simulations also show the potential for substantial current generation in NSTX-U [150]. One reason for this can be seen in figure 30(*a*), which shows the location of the injector coil in relation to the CHI injector gap across which the voltage is applied. This improved current generation potential in NSTX-U is due in part to the improved location of the CHI injector flux coil (lower PF1C coil), which is positioned much closer to the CHI insulating gap. As shown in figure 30(*a*), the injector coil in NSTX is farther away from the insulating gap, resulting in a 2.5 times smaller flux generated by this coil that connects the inner and outer divertor plates. Quantitatively, the available injector flux in NSTX-U is projected to be approximately 200 mWb compared with less than 80 mWb in NSTX.

In addition to the improved positioning of the lower divertor PF coils in NSTX-U for CHI, figure 30(*b*) shows that the location of the absorber coil (upper PF1C coil) is better positioned in NSTX-U. This coil is used to generate a buffer flux to keep the expanding CHI discharge from contacting the upper absorber gap, as such a condition (known as an absorber arc) can short-circuit the insulating gap and cause the injected current to flow through this gap instead of through the main plasma. The closer positioning of the PF1C coil to the absorber gap enables the flux generated by this coil to be more efficiently
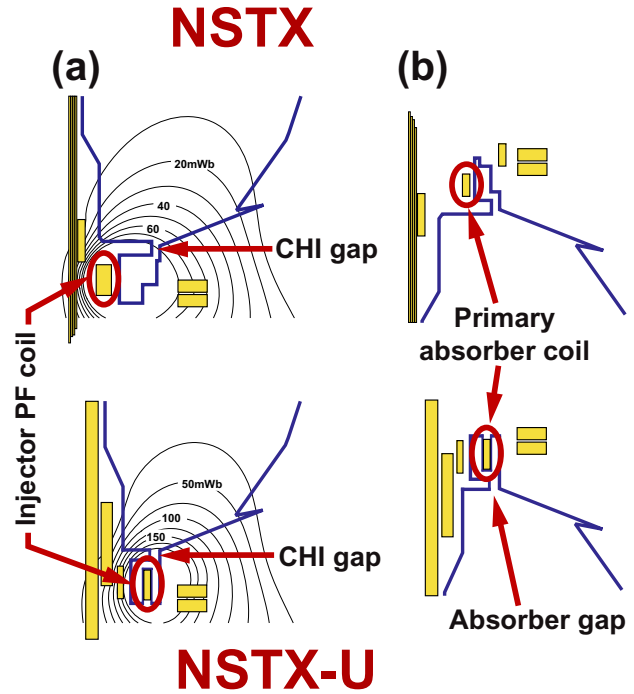
Figure 30. (*a*) Poloidal flux contours in the injector region of NSTX (top) and NSTX-U (bottom) and (*b*) field-nulling and divertor coils in the absorber region for CHI experiments.

utilized to suppress absorber arcs. Importantly, the kA-turn capability of the absorber coil in NSTX-U is three times that in NSTX (318 kA-turn versus 100 kA-turn in NSTX) and the current slew rate is also substantially higher (40 kA-turn ms^{-1} in NSTX-U versus 5 kA-turns ms^{-1} in NSTX). The faster slew rates are needed to rapidly turn off the lower divertor PF coils after the CHI plasma formation process is complete and to track the rapid upward motion of the higher-I_P CHI plasma expected in NSTX-U.

Overall, CHI current formation scales favourably with the available injector flux and the enclosed toroidal flux, and CHI is projected to be capable of generating 300–600 kA of closed-flux current in NSTX Upgrade by operating at 1T based on scaling the results of figures 28 and 29 and TSC simulations [150]. Using the HIT-II, NSTX, and TSC results as a starting point, relatively simple scalings can be used to project to NSTX-U and next-step STs, and the results of such scalings are shown in table 3. In general, HIT-II results are used where NSTX results are unavailable. In these scalings it is assumed that the start-up internal inductance l_i is the same as the NSTX value of 0.35, the flux footprint d scales as the minor radius a relative to the NSTX value, and the injector flux ψ_{inj} scales as $R I_P$. Further, and consistent with the HIT-II results, it is assumed the injector current I_{inj} is 1.2 times the bubble burst current I_{bb} and that the start-up plasma closed poloidal flux ψ_p achieved is 80% of the injector flux ψ_{inj}. Lastly, the current multiplication I_P/I_{inj} is held below the limiting value $M \equiv \Phi_T/\psi_{inj}$ based on the results from NSTX. The projected electrode current densities of up to 63 kA m^{-2} in ST-FNSF are significantly lower than those achieved successfully on HIT-II [146] (300 kA m^{-2}) which appears favourable, but the optimal electrode design and the required CHI voltage for FNSF/Pilot

Table 3. Achieved parameters for CHI plasma formation in NSTX and projections to NSTX-U, ST-FNSF and ST Pilot Plant.

Parameters	NSTX	NSTX-U	ST-FNSF	ST Pilot Plant
Aspect ratio: A	1.30	1.50	1.50	1.70
Elongation: κ	2.6	2.8	3.1	3.3
Major radius: R_0 (m)	0.86	0.93	1.2	2.2
Minor radius: a (m)	0.66	0.62	0.80	1.29
Toroidal field at R_0: B_T (T)	0.55	1	2.2	2.4
TF rod current: I_{TF} (MA)	2.4	4.7	13.2	26.4
Toroidal flux: Φ_T (Wb)	2.5	3.9	15.8	45.7
Reference maximum sustained plasma current: I_{PS} (MA)	1	2	10	18
Start-up plasma normalized internal inductance: l_i	0.35	0.35	0.35	0.35
Injector flux footprint: d (m)	0.6	0.56	0.73	1.17
Injector flux for projecting start-up current: ψ_{inj} (Wb)	0.047	0.10	0.66	2.18
Bubble-burst current: I_{bb} (kA)	3.3	9.0	79	165
Injector current: I_{inj} (kA)	4.0	10.8	95	198
Start-up plasma flux: ψ_p (Wb)	0.04	0.08	0.53	1.74
Start-up plasma current achieved or projected: I_P (MA)	0.20	0.40	2.00	3.60
Current multiplication: I_P/I_{inj}	50	37	21	18
Multiplication limit: Φ_T/ψ_{inj}	53	38	24	21
Injector current density (kA m^{-2})	4.9	12	63	39

applications require additional research and development. In summary, these CHI scalings project to 0.4 MA of start-up current in NSTX-U, 2 MA in ST-FNSF and 3.6 MA in an ST Pilot Plant, and these values correspond to 20% of the nominal maximum plasma current for each device. The applicability of CHI start-up to a nuclear environment and the possible need for rapidly varying PFs that must penetrate through substantial nearby conducting structure (such as blankets, shields, or a single-turn TF conductor) will be treated in future work.

As described in section 2.3.7, 0.4 MA is sufficient plasma current in NSTX-U to confine the fast-ions of the new 2nd NBI. However, additional heating of the CHI target plasma by HHFW may be needed to increase the electron temperature to increase the L/R decay time of the plasma current [150] to provide sufficient time for the NBI ions to slow down to heat the plasma and to drive NBI current. Simulations are underway to assess the needed auxiliary electron heating for CHI-produced plasmas, and studies of this issue will be pursued in NSTX Upgrade to inform the requirements for the heating and non-inductive ramp-up of CHI-produced plasmas in next-step STs.

Lastly, it should be noted that initial CHI experiments in NSTX focused on driving steady-state current [151, 152], but with this technique there was little evidence for the formation of closed poloidal flux, the DC power supply power required was large (20 kA × 500 V = 10 MW for 200 kA of plasma current), and coupling to ohmic or NBI-heated plasmas was difficult due to absorber arcs. Further, adding steady-state CHI current drive to other forms of current drive (such as to an inductively driven LSN plasma) did not drive significant additional current. This result may have been related to the need for (and apparent lack of) $n = 1$ MHD-driven flux-surface opening at the plasma boundary to achieve 3D-reconnection-driven CHI current drive [153, 154]. In contrast, the transient CHI plasma formation described here involves primarily inductive current drive and axisymmetric reconnection driven by the decay of the open-field-line injector current and the PF coil current variation as simulated with the axisymmetric TSC code. Transient CHI has exhibited formation of closed poloidal flux plasma current [155] with good coupling to ohmic current drive and NBI H-mode, and extrapolates favourably to next-step STs.

For these reasons, it is likely that NSTX Upgrade will continue to focus primarily on transient/axisymmetric CHI plasma current formation rather than steady-state/3D-reconnection-driven CHI current sustainment.

2.3.7. Non-inductive current ramp-up. Moving to the consideration of non-inductive current ramp-up for NSTX-U, a very important benefit of more tangential NBI is the ability to heat and drive current in low-current target plasmas. As shown in figure 31(*a*), the injected current drive efficiency of the more tangential 2nd NBI (60–65 kA MW^{-1}) is a factor of 3–4 times higher than the present NBI (15–20 kA MA^{-1}) for low $I_p = 0.4$ MA target plasmas. As shown in figure 31(*b*), this is because of the much lower bad-orbit losses (due to more parallel injection) of the new NBI sources at low plasma current. As is also evident from figures 31(*a*) and (*b*), the tangency radii of the 2nd NBI are close to the optimal values (by design) for maximizing the NBICD by minimizing the power loss at low plasma current. This prediction of good absorption and current drive efficiency at low I_P opens the possibility of non-inductive ramp-up studies in NSTX Upgrade to prototype non-solenoidal ramp-up in an ST-FNSF.

Free-boundary TSC simulations have been carried out to further assess solenoid-free current-ramp for NSTX Upgrade using early HHFW heating to pre-heat a low-I_P target to high non-inductive fraction followed by NBI heating and current drive. The TSC simulations of non-solenoidal ramp-up described here will be coupled to TSC simulations of CHI start-up [150] in future work. Figure 32(*a*) shows the simulated evolution of the auxiliary heating from HHFW (green) and NBI (red) used in TSC. Figure 32(*b*) shows the plasma current components in these simulations. TSC does not explicitly deal with the fast-ion component of the stored energy, and uses fixed profile shapes and efficiencies for the NBI CD chosen to be similar to those shown in figure 22. In these TSC calculations, a limited, $I_P = 150$ kA, low density L-mode target plasma with $T_e(0) = 0.5$ keV is provided as an initial condition to simulate the conditions of an HHFW-heated CHI plasma that remains to be developed in future experiments on NSTX Upgrade.
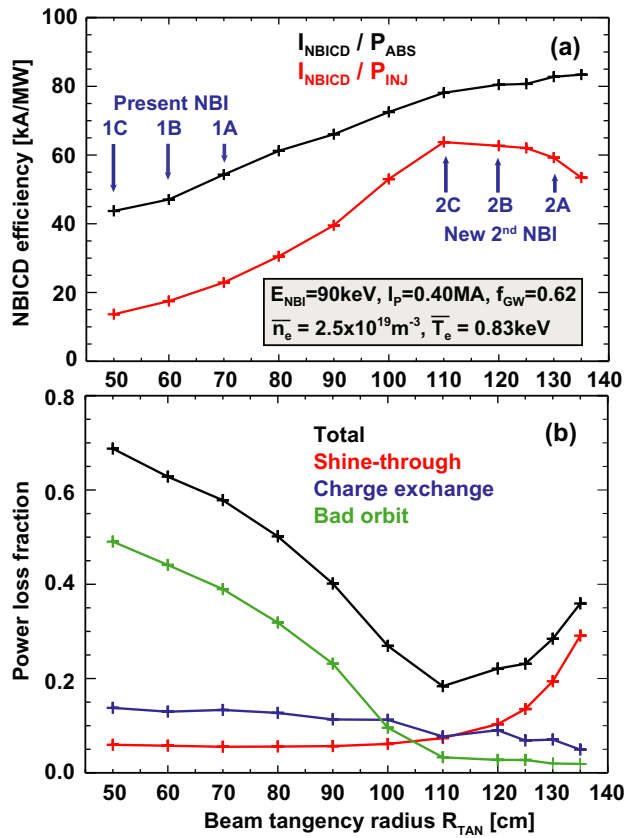
Figure 31. (*a*) NBICD efficiency (kA MW^{-1}) and (*b*) power loss fractions (total, shine-through, charge exchange, and bad orbit) as a function of beam tangency radius R_{TAN} for an $A = 1.65$, $I_P = 0.40$ MA, $B_T = 0.9$ T NSTX Upgrade target plasma with a 7.4 cm outer gap.
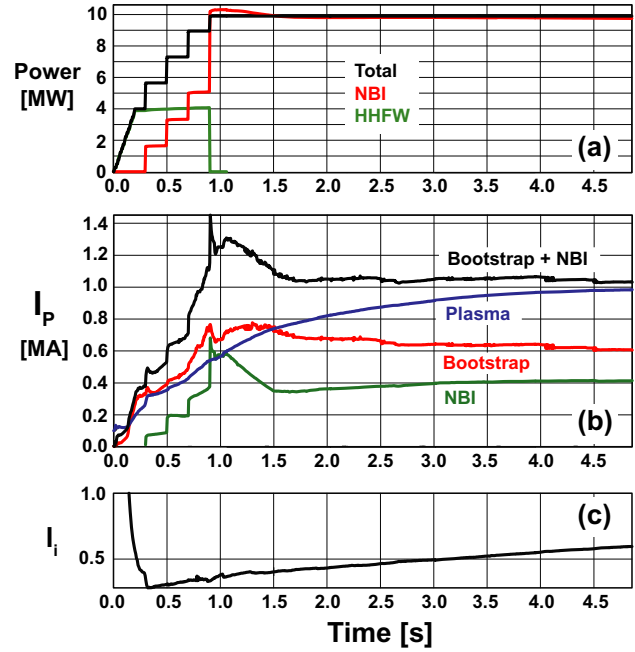

Figure 32. Evolution of (*a*) heating powers, (*b*) plasma current components and (*c*) internal inductance from TSC simulations of plasma-current ramp-up to $I_P = 1$ MA without using the ohmic solenoid.

As described in section 2.3.6, closed-flux plasma currents of 150–200 kA have already been produced with CHI start-up, HHFW has successfully heated inductive plasmas initiated with CHI [123], and HHFW has heated 300 kA ohmic target plasmas to 3 keV as shown in figure 27.

Figure 32(*a*) shows the HHFW power is ramped linearly to 4 MW over 200 ms, and this increases the projected bootstrap current to 300–350 kA as shown in figure 32(*b*) and consistent with extrapolations from the data in figure 27. For times after 0.2 s, the bootstrap + NBI current exceeds the equilibrium plasma current and the plasma current is over-driven. The plasma current evolution in these simulations is slower than the evolution of the non-inductive current since the changing plasma current leads to a change in magnetic flux inside the conducting plasma loop. According to Faraday's law this flux change induces an electromotive force that drives current in the opposite direction to the non-inductively driven current. Since the plasma current is equal to the sum of inductive and non-inductive currents, the (negative) inductively driven current is equal to the difference between the plasma current (blue) and the non-inductive bootstrap + NBI current (black) shown in figure 32(*b*).

Once the plasma current exceeds 300–350 kA, the new 2nd NBI will be absorbed at the 70–80% level, and the simulated NBI power is increased in three 1.65 MW increments to 5MW as shown in figure 32(*a*). This further increases

the bootstrap current and drives 250–300 kA of NBI current which increases the plasma current to 500–550 kA. At this time ($t = 0.85$ s), the HHFW is turned off and replaced with an additional 5MW of NBI power simulating usage of the original NSTX NBI. This increase in NBI power increases the bootstrap + NBI non-inductive current drive to 1.2–1.3 MA, and this current drive decreases to 1–1.1 MA by $t = 1.5$ s as the density increases for fixed Greenwald fraction and increasing plasma current. As shown in figure 32(*b*), the bootstrap and NBI currents reach steady values of 0.6 MA and 0.4 MA, respectively, for $t > 2.5$ s, and the plasma current asymptotically approaches 1 MA by $t = 4.5$ s. During this time, the internal inductance slowly rises from 0.35 to 0.6 by $t = 4.9$ s as shown in figure 32(*c*) and the shot-average $\kappa \approx 3$ (not shown).

The stability, confinement, and temperature information for the TSC simulations in figure 32 are shown in figure 33. Figure 33(*a*) shows the thermal β_P rises to approximately 3 by $t = 1$ s and then decays to 1–1.5 by $t = 4.5$ s consistent with the bootstrap-current fraction decreasing from 120% to 60% over the same period. Figure 33(*b*) shows the thermal β_N remains below 2.5 for the entire duration of the simulation. Figure 33(*c*) shows the normalized density value increases to 0.65 by $t = 0.2$ s, decreases, and then is nearly constant at 0.5 after $t = 1$ s. Based on the scalings of the fast-ion stored energy and results from table 1, the fast-ion stored energy fraction is approximately 50% for such plasmas, so the estimated total $\beta_N \approx 5$. The Coppi–Tang L-mode transport model [156] is used in the initial L-mode phase, and this transport model is augmented with a reduced thermal diffusivity in the pedestal region to simulate an H-mode and give the profile shape observed in the high bootstrap-fraction phase of the H-mode. In the simulations, the H-mode phase begins at $t = 0.12$ s, and

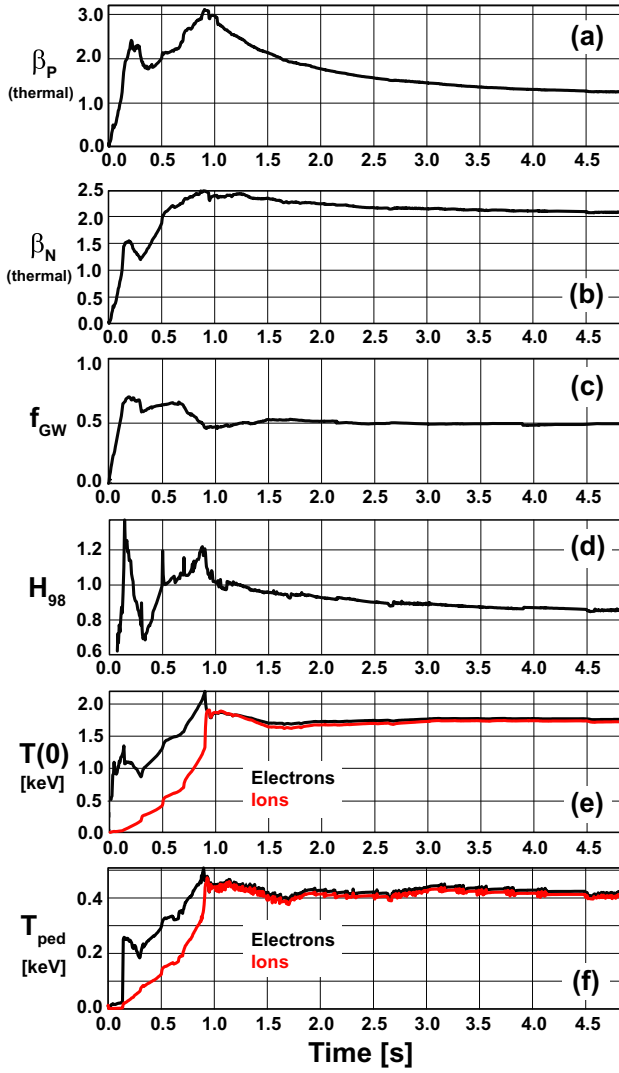**Figure 33.** Evolution of (*a*) poloidal beta (thermal component), (*b*) normalized beta (thermal component), (*c*) Greenwald fraction, (*d*) H_{98}, (*e*) central electron and ion temperatures and (*f*) H-mode pedestal electron and ion temperatures from TSC simulations of plasma-current ramp-up to $I_P = 1$ MA without using the ohmic solenoid. The H-mode is triggered at $t = 0.12$ s in the simulations.

in both the L and H-mode phases, the density profile shape is prescribed and has a peaking factor of approximately 1.1 (see figure 34). The Z_{eff} value of 3.5 is also prescribed and is constant in time and space.

Using these assumptions, figure 33(*d*) shows the H_{98} evolution. While there are some oscillations in the H_{98} value between 0.7 and 1.3 in the first 1 s of the simulation, the H_{98} has a slowly varying value decreasing from 1 to 0.85 after $t = 1$ s, and on-average is at or below 1. The resulting central and pedestal temperatures are shown in figures 33(*e*) and (*f*), and have values of 1.7 keV and 0.4 keV, respectively, after $t = 1$ s. As shown in figures 33 and 34, T_e is significantly higher than T_i during the HHFW heating phase, and the temperatures become similar during the NBI heating phase is also observed in NSTX experiments. One important difference between the NSTX experiments and the TSC simulations is that in the experiments, χ_e is generally greater than χ_i, and χ_i is approximately neoclassical, whereas the Coppi–Tang
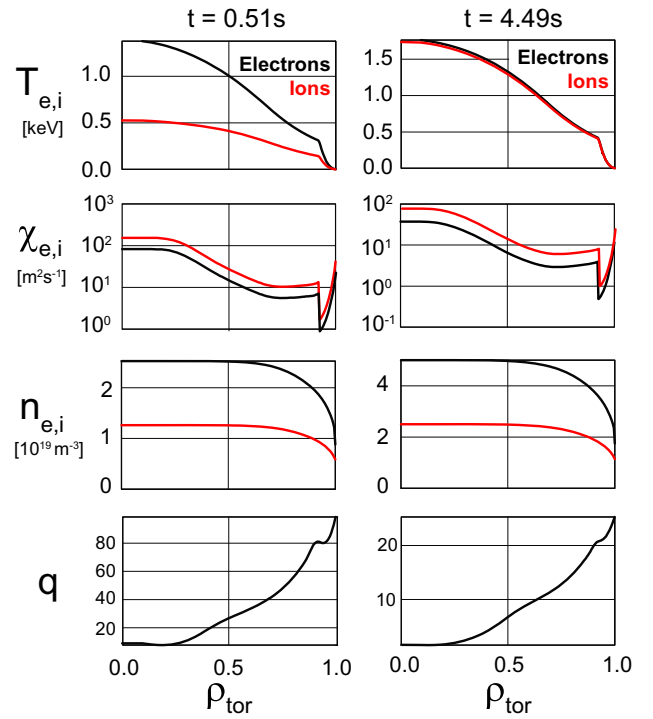
Figure 34. Profiles of the electron and ion temperatures, thermal diffusivities, and densities, and q profiles from TSC simulations of plasma-current ramp-up without using the ohmic solenoid. The profiles are plotted for two times in the simulations: early in the ramp-up ($t = 0.51$ s, $I_P = 0.35$ MA), and later in time ($t = 4.5$ s) when the plasma current ($I_P = 1$ MA) is nearly equal to the NBI+bootstrap overdrive current.

model (with H-mode added) predicts $\chi_i > \chi_e$ as shown in figure 34. The impact of the transport model on the TSC ramp-up simulations is a topic for future research. Lastly, figure 34 also shows the q profiles early and late in the non-inductive ramp-up simulations. The initial q profile has weakly reversed shear in the plasma core, and the later q profile is monotonic with weak shear in the plasma core. At $t = 4.5$ s, the central q has a value of 1.3–1.4 and is slowly decreasing. Based on these simulations, by operating at 1 T and combining CHI current formation of 300–400 kA with NBI current ramp-up using the 2nd more tangential NBI, NSTX Upgrade appears well equipped to study non-inductive current formation and ramp-up as needed for an ST-FNSF.

2.4. Disruption forces

2.4.1. Overview. Just as the equilibrium electromagnetic forces on the structure will increase by up to a factor of 4 in NSTX Upgrade, the forces during plasma disruptions are expected to increase by a similar factor. The projections for NSTX Upgrade rely heavily on the previous characterization of vertical displacement events (VDEs) and plasma current quenches (CQs) from NSTX [157]. Based on NSTX data and scalings, 3D electromagnetic models of the vacuum vessel and passive conducting structures of NSTX have been utilized to predict the induced currents, fields, and forces for 2 MA, 1 T plasma disruptions in NSTX Upgrade [158].

Table 4. Disruption scenarios used for stress analysis for NSTX-Upgrade.

Category	Scenario index	Disruption scenario description	Initial position index	Final position index	VDE drift time (ms)	I_p quench time (ms)	I_p quench rate (GA s^{-1})	Halo fraction f_h
1	1	Centered disruption, fast quench	1	1		1	2	0
1	10	Centered disruption, medium quench	1	1		4	0.5	0
2	2	Initiated shifted to CS, fast quench, no halo	2	2		1	2	0
2	6	Inward drift to CS, very slow quench, halo	1	2	10	100	0.02	0.2
2	11	Inward drift to CS, fast quench, halo	1	2	10	1	2	0.2
2	12	Inward drift to CS, medium quench, halo	1	2	10	4	0.5	0.2
2	19	Inward drift to CS, fast quench, no halo	1	2	10	1	2	0
2	20	Inward drift to CS, medium quench, no halo	1	2	10	4	0.5	0
2	21	Inward drift to CS, slow quench, no halo	1	2	10	40	0.05	0
3	3	Initiated shifted down to inboard, fast quench, no halo	3	3		1	2	0
3	7	Vertical drift to inboard, very slow quench, halo	1	3	10	100	0.02	0.35
3	13	Vertical drift to inboard, fast quench, halo	1	3	10	1	2	0.35
3	14	Vertical drift to inboard, medium quench, halo	1	3	10	4	0.5	0.35
3	22	Vertical drift to inboard, fast quench, no halo	1	3	10	1	2	0
3	23	Vertical drift to inboard, medium quench, no halo	1	3	10	4	0.5	0
3	24	Vertical drift to inboard, slow quench, no halo	1	3	10	40	0.05	0
4	4	Initiated shifted down to middle, fast quench, no halo	4	4		1	2	0
4	8	Vertical drift to middle, very slow quench, halo	1	4	10	100	0.02	0.35
4	15	Vertical drift to middle, fast quench, halo	1	4	10	1	2	0.35
4	16	Vertical drift to middle, medium quench, halo	1	4	10	4	0.5	0.35
4	25	Vertical drift to middle, fast quench, no halo	1	4	10	1	2	0
4	26	Vertical drift to middle, medium quench, no halo	1	4	10	4	0.5	0
4	27	Vertical drift to middle, slow quench, no halo	1	4	10	40	0.05	0
5	5	Initiated shifted down to outboard, fast quench, no halo	5	5		1	2	0
5	9	Vertical drift to outboard, very slow quench, halo	1	5	10	100	0.02	0.35
5	17	Vertical drift to outboard, fast quench, halo	1	5	10	1	2	0.35
5	18	Vertical drift to outboard, medium quench, halo	1	5	10	4	0.5	0.35
5	28	Vertical drift to outboard, fast quench, no halo	1	5	10	1	2	0
5	29	Vertical drift to outboard, medium quench, no halo	1	5	10	4	0.5	0
5	30	Vertical drift to outboard, slow quench, no halo	1	5	10	40	0.05	0

The disruption modelling utilizes a range of disruption scenarios and time-scales based on NSTX data and experience. Table 4 summarizes the five types of disruption categories analysed, namely: radially centred (black/grey), inward drift to CS (purple), VDE to inboard divertor (green), VDE to middle/outer divertor (blue) and VDE to outboard to passive plates (yellow). Each of these disruption categories has additional variations of VDE drift time, CQ time, and halo current magnitude to span the range of typical NSTX disruption characteristics but scaled and analysed for 2MA disruptions in NSTX Upgrade. The circles in figure 35(*a*) indicate the positions and sizes of the disrupting plasma current channels for each of the five disruption categories of table 4. The plasma current density is assumed to be spatially uniform inside each circle, and the total current in each circle is varied linearly in time depending on the details of each scenario. Circles that represent current channels that have drifted to the location shown have square symbols at the centre of each circle and two square symbols on the limiter boundary. The symbols on the limiter boundary indicate the assumed locations for halo current strikes for halo currents driven during the plasma CQ. Figure 35(*b*) shows the time evolution of disrupting plasma currents for a representative VDE to the inboard divertor with medium quench rate and including halo currents. In this model,

the vertically centred current (black circle in figure 35(*a*)) is ramped from 2 to 0 MA (blue curve in figure 35(*b*)) while the vertically displaced current (green circle in figure 35(*a*)) is ramped from 0 to 2 MA (red curve in figure 35(*b*)) during the same interval. Ramping the currents in this way simulates the downward vertical motion of plasma over a typical drift period of 10 ms. After the drift phase, the vertically displaced current is ramped from 2 to 0 MA for a range of CQ durations, in this case 4ms for the scenario shown. During the CQ, the halo current is typically small at the beginning of the quench, reaches a maximum value approximately half way through the quench and becomes small again near the end of the quench [159]. This evolution is modelled as a triangular current waveform as shown by the green curve in figure 35(*b*), and the maximum value of the halo current is set by the assumed halo current fraction relative to the pre-quench current. In this case the halo current fraction $f_{halo} = 35\%$, so the maximum $I_{halo} = 0.7$ MA.

For each of the NSTX Upgrade structures analysed for disruption loads, the plasma-induced inductively-driven voltages from inward or vertical plasma motion and from the CQ are treated as axisymmetric, i.e. any 3D distortions of the plasma current channel are ignored. However, these 2D applied voltages can induce 3D currents in the conducting
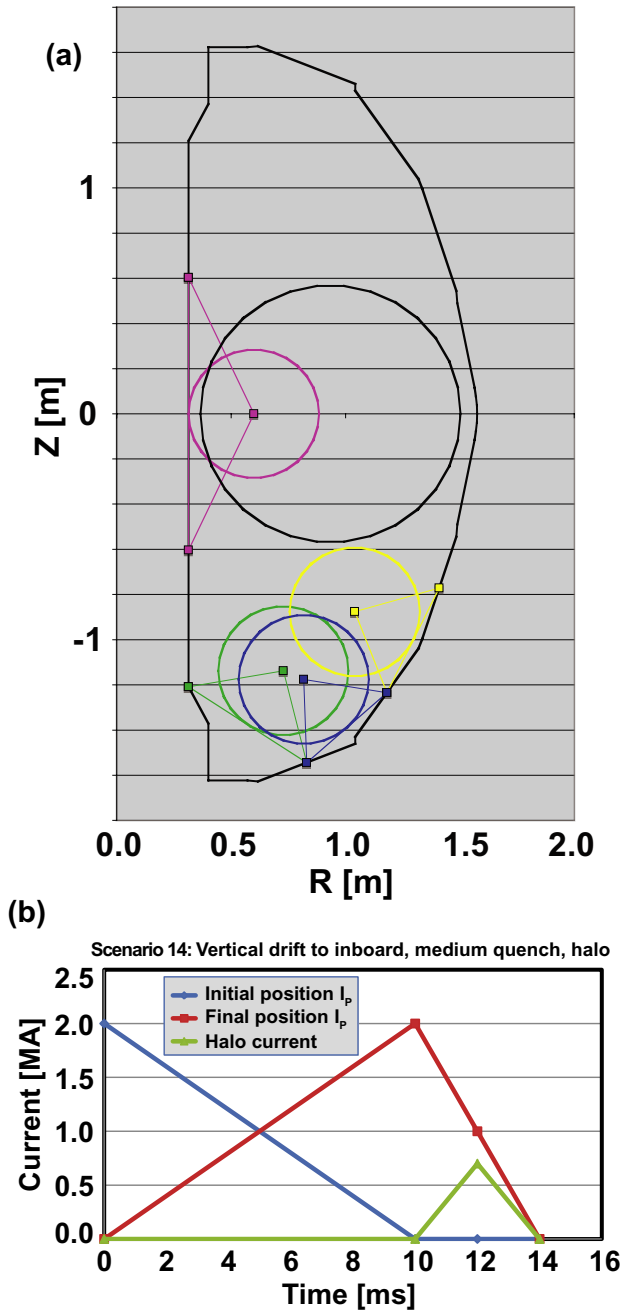
Figure 35. (*a*) Locations and sizes of disrupting plasmas (circles) and halo current entry and exit points (box symbols) on the limiter boundary used in stress analyses, and (*b*) time evolution of plasma current at initial position (blue) and final position (red) and halo current (green) for a representative VDE to the inboard divertor: scenario 14 in table 4.

The combined currents from plasma motion, CQ and halo currents are then used to compute the total currents and forces on the conducting structures, and the NSTX Upgrade components are then designed/modified (if needed) to withstand these loads. Overall, the disruption analysis indicates that forces on the vessel are generally reduced by shielding from the passive conducting plates, and that the Lorentz forces on the passive plates from the quenching of a VDE displaced plasma sitting near the plates dominates over halo current effects. Further, the CS casing and divertor conducting structures are sufficiently strong to withstand axisymmetric loads from plasma motion and CQ, but halo currents in the CS introduce lateral forces and displacements that must be supported. Additional details for these most important disruption effects are provided below, i.e. the forces on the passive plates from VDE drift and CQ and the effects of halo currents on the CS casing.

2.4.2. VDE and CQ analysis for passive plates. As described above, an important consideration for NSTX Upgrade disruption VDE motion and CQ is the stress applied to the passive plates. Of particular concern is the possibility of radial plate displacements and permanent deformation (and possibly tile cracking) caused by Lorentz forces resulting from toroidal currents circulating in the plate crossed with the (coil plus plasma) poloidal magnetic field. Since the passive plates play an important role in vertical stability and RWM stabilization in NSTX and NSTX Upgrade, using higher strength but more resistive plate material (such as stainless steel) is likely not an acceptable option.

Using the simplified plasma vertical displacement model for NSTX Upgrade [158] from table 4 and figure 35, figure 36(*a*) shows the lower passive plate current density induced by the downward vertical drift of a 2 MA plasma with a drift duration of 10 ms. These simulations using Opera and ANSYS analysis software find that VDE drift durations in this range maximize the induced circulating currents and radial forces on the passive plates. Figure 36(*b*) shows that the peak plate deflection is approximately 1 mm as indicated by the orange and red contours near the top and bottom of the passive plate at the plate toroidal mid-point between the plate supports. The corresponding peak membrane plus bending stress is 60 MPa which is a factor of 3 below the yield stress. This stress level found at the mid-point between the plate supports is acceptable for NSTX Upgrade. However, the stresses near the bolt heads attaching the plates to the supports are above allowable limits, and at a minimum, enhancements such as higher strength bolts and/or larger bolt-head slots and washers will be required to withstand the increased disruption loads of NSTX Upgrade.

If plate attachment enhancements were found to be insufficient or infeasible, or if it is desired in the future to increase the maximum plasma current to above 2 MA in NSTX Upgrade, one possible means of reducing the peak stress and radial displacement during disruptions is to use thicker passive plates. For fixed applied load, the plate displacement scales as the inverse of the thickness cubed, so doubling the CuCrZr plate thickness from 0.5 to 1 inch could substantially reduce the plate deflection under disruption loads. However, the increased conductance of the thicker plate could increase the induced
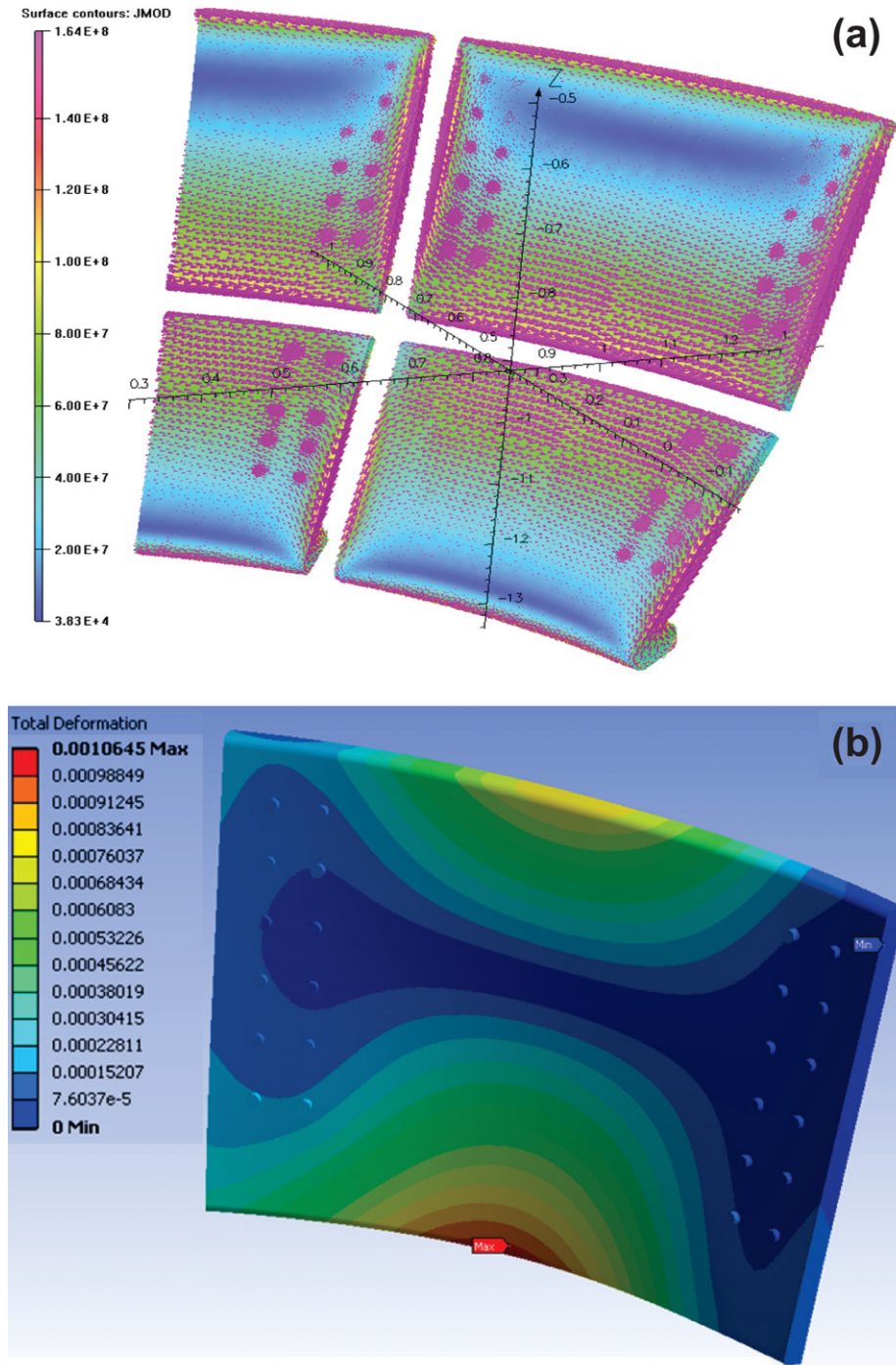
structures including the passive conducting plates, divertor plates, vacuum vessel and CS casing. Additionally, halo currents are modelled as a current source with the current entry and exit points as shown in figure 35(*a*) with a prescribed toroidal peaking factor of 2 and halo current fractions chosen based on NSTX data. Specifically, $f_{halo} = 0.2$ for inboard/CS disruptions and 0.35 for VDE disruptions. This product of peaking factor and f_{halo} is consistent with the upper-bound observed in available NSTX data.

Figure 36. (*a*) Passive plate current density (A m^{-2}) and (*b*) primary passive plate deflection (m) during a simulated downward VDE.

current, which could reduce the effectiveness of thicker plates, and would also increase the penetration time of fields normal to the passive plates.

In addition to the 3D modelling, the LRDFIT[8] axisymmetric-equivalent circuit model of the coils and passive conducting regions has been developed, benchmarked, and extensively used for NSTX and is used here to assess the impact of thicker plates. Figure 37 shows the LRDFIT-reconstructed plasma and plate current evolution for a representative VDE

disruption in NSTX. As seen in figure 37(*a*) for a downward VDE, the chosen plasma drifts from nearly vertically centred to being limited on the lower divertor plate in 5–10 ms which is comparable to the drift duration of the simulated case of figure 36. As shown in figure 37(*b*), during this drift phase, the plasma cross-section is reduced while the plasma current is maintained. As is evident from figures 37(*c*) and (*d*), the net toroidal plate current induced by the plasma motion is negative as the plate currents act to oppose the downward vertical plasma motion. Then, as the CQ occurs over the subsequent 2–3 ms, the net toroidal plate current induced by

---
[8] http://w3.pppl.gov/~jmenard/software/lrdfit/lrdfit-index.htm
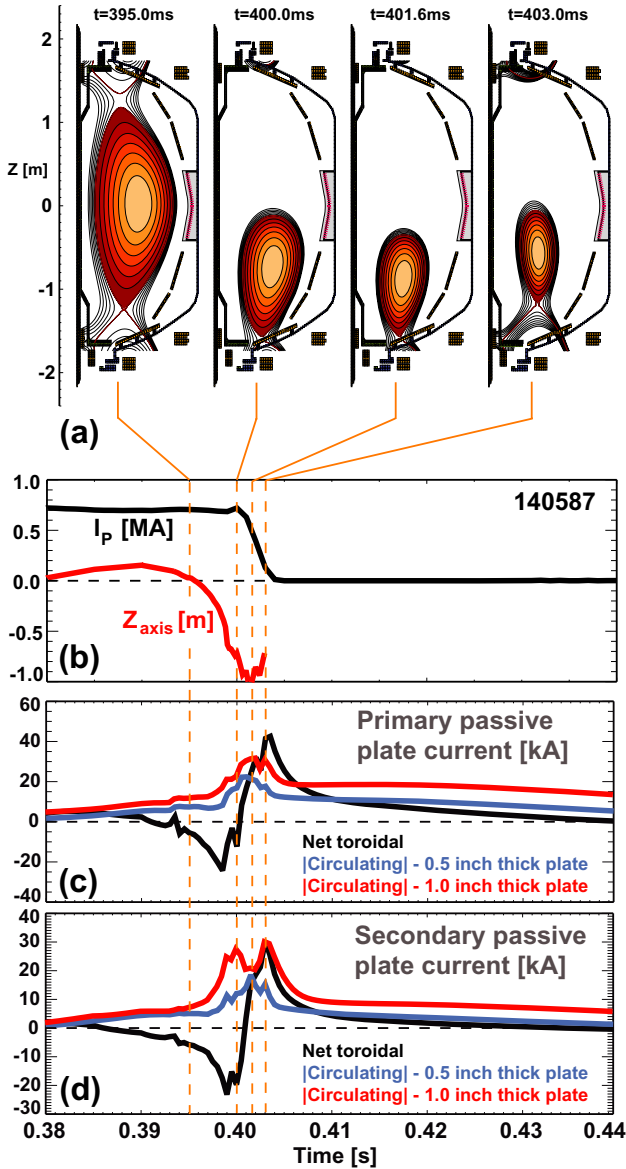
Figure 37. (*a*) Plasma position and shape evolution, (*b*) plasma current and magnetic axis position, (*c*) primary passive plate currents and (*d*) secondary passive plate currents during a vertical displacement event (VDE) and CQ in NSTX.

the quench is reversed and becomes positive in response to the loss of positive plasma current and poloidal magnetic energy.

An important aspect of the NSTX passive structure design is that the stainless steel supports connecting the plates to the vessel wall are several orders of magnitude more resistive than the CuCrZr passive plates, and therefore the net toroidal current is effectively unchanged by increasing the plate thickness. For this reason, figures 37(*c*) and (*d*) only plot the net toroidal current for the present 0.5 inch thick passive plates, since the currents are nearly identical for the two plate thicknesses. In contrast, the circulating current magnitudes do increase with plate thickness since the plate resistance is reduced. The maximum circulating currents in figures 37(*c*) and (*d*) are approximately 1.5 times higher for the 1.0 inch thick plates versus the present 0.5 inch plates. Also, after the end of the CQ, the circulating currents in the thicker plates are approximately

a factor of 2 times higher and decay away more slowly due to the lower plate resistance and longer L/R time. It is noted however that these increased currents occur after the CQ, so there is little impact of these currents on the plasma current flat-top phase. Further, modelling of the plasma current ramp-up finds that these currents are sufficiently small that they would not significantly impact normal plasma operations.

In the analysis described above and shown in figures 37 and 38, the circulating current is defined as $I_{circ} = \frac{1}{2}\Sigma_j|I_j - I_{avg}|$ where I_j is the toroidal current in conducting element i of a conducting region, each conducting element cross-sectional area is identical in a given region, and I_{avg} is the average value of I_j. Thus, if the current density in a region is constant, I_j will be also, and $I_{circ} = 0$. Correspondingly, if the net toroidal current is zero, $I_{avg} = 0$, and I_{circ} is equivalent to the total positive toroidal current flowing in the region.

To further analyse the distribution of current in the passive plates, figure 38 plots the plate toroidal current density for the shot in figure 37 at $t = 403$ ms at the time of peak net toroidal current and Lorentz pressure which is just after the time of peak circulating current magnitude. As shown in figures 38(*a*) and (*b*) the maximum current density occurs near the top end of each plate where the net toroidal and circulating components are additive in the positive (co-plasma current) direction, while the negative current density occurs on the bottom of each plate with a magnitude typically less than the peak positive value. At this time during the disruption evolution, figures 38(*a*) and (*b*) show that some of the negative current density is carried on the back each plate, and similar skin effects are observed in the Opera electromagnetic simulations of figure 36(*a*). These results highlight the importance of using models that include finite conductor thickness to accurately assess VDE induced currents in passive conducting structures, in particular for the fastest disruptions with the shallowest skin-depths. Further, figures 38(*b*) shows that the peak positive current density of the thicker plate is 15–22% lower than for the thinner plate. This reduction likely contributes to the peak circulating current magnitude in the thicker plate being less than a factor of two higher than in the thinner plate.

The peak plate toroidal current density during the disruption evolution of figure 37 is ≈ 33 MA m^{-2} which scaled (by a factor of 1.6) to the worst-case net toroidal current for 0.7 MA NSTX plasmas [157] and then scaled (by a factor of 3) to 2 MA plasmas projects to 160 MA m^{-2} in NSTX Upgrade. This value is in good quantitative agreement with 3D predictions of the peak plate current density of 120–160 MA m^{-2} for the simulated plasma vertical drift scenario shown in figure 36(*a*). This analysis indicates that a doubling of plate thickness would result in an increase in plate circulating current by a factor of 1.5–2 and result in an estimated net 4–5 fold reduction in plate displacement, i.e. plate displacement comparable to present NSTX values and therefore capable of handling 2 MA disruptions with an expectation of no plate damage over the lifetime of the Upgrade.

In summary, the passive plate analysis indicates that higher strength bolts and larger bolt-head slots and washers can withstand the increased loading of NSTX Upgrade 2 MA disruptions, and this remains true when the effects of halo currents are also included. Another option is to use thicker
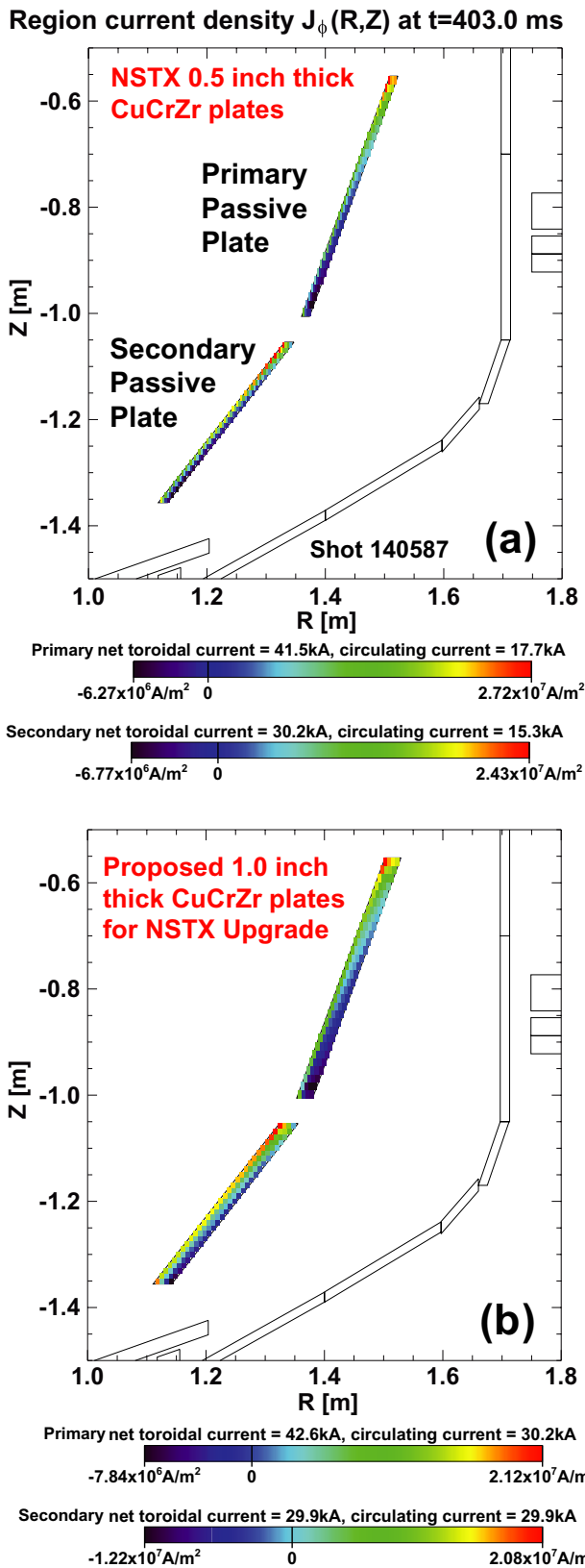
Figure 38. Toroidal current density in the primary and secondary passive plates at the time of peak net toroidal current and near the time of peak circulating current for (*a*) the present NSTX passive plates and (*b*) thicker passive plates being assessed for NSTX Upgrade for the shot shown in figure 37.

passive plate material to reduce plate deflection, and this may be required if operation at higher plasma current (>2 MA) is to be pursued in NSTX Upgrade. However, the fabrication of new passive plates is of higher cost than modifying the existing plates, and would also require modifications to the PFCs attached to the existing passive plates (or possibly new PFCs). Since modifying the existing passive plates appears sufficient to withstand 2MA disruptions in NSTX Upgrade, the present plan is to enhance the plate attachments rather than fabricate new thicker plates.

2.4.3. Halo current analysis for the CS casing. Structural analysis of the CS casing indicates that any induced currents from drift and/or CQ induce primarily compressive or hoop stresses that are well below structural limits. However, the non-axisymmetry of halo currents can potentially induce net lateral forces on the CS that must be countered through the supports attaching the CS to the test-cell floor at the bottom of the machine and by the bellows (or other structure) at the top of the CS. In particular, it is expected that such loads will be highest shortly after a halo current strike (i.e. with the inductive current density distribution) before the halo currents have time to redistribute resistively through the casing.

Vertically centred disruptions in NSTX are most commonly inboard-limited on the CS as a result of some event that causes a rapid loss of some fraction of the plasma current or β such that the radial position control cannot respond sufficiently fast, and the applied vertical field pushes the plasma onto the CS. If the plasma is pushed sufficiently hard against the CS, it also shrinks, increases in aspect ratio, and becomes more circular. The simplified model of this process is represented by category 2 disruptions in table 4 and by the translation from the black to purple plasma boundary and associated current shown in figure 35(*a*). For this vertically centred inboard-limited quenching plasma model, the halo current strike locations are shown by the purple squares in figure 35(*a*) at $Z = \pm 0.6$ m on the CS limiter boundary.

Figure 39(*a*) shows the radial current vectors of the injected current used to simulate the entry and exit of the halo current strike with a toroidal peaking factor of 2 as described in section 2.4.1. For the purpose of identifying the characteristic time-scales of the CS halo current evolution, figures 39(*b*)–(*d*) show the response to a step increase of the halo current from 0 kA to a constant 400 kA at $t = 0$ ms. Figure 39(*b*) shows the current distribution along the CS casing immediately after the model halo current strike and represents the inductive response. Figure 39(*c*) shows the current distribution along the CS casing 10 ms after the halo current strike and represents the resistive response since the current in the casing has stopped evolving and is resistively distributed. Figure 39(*d*) shows the time evolution of the maximum current density (J_{max}) and minimum current density (J_{min}) at the vertical midplane. Both the maximum and minimum J can be well fit by an exponential function that decays to the resistive value with a 1.3 ms time constant, and these simulations illustrate that the current at the midplane relaxes to the resistive distribution with significantly reduced toroidal peaking in approximately 4 ms.

As discussed in section 2.4.1, rather than having a step-wise increase, the halo current begins increasing after the beginning of the CQ, typically reaches maximum value
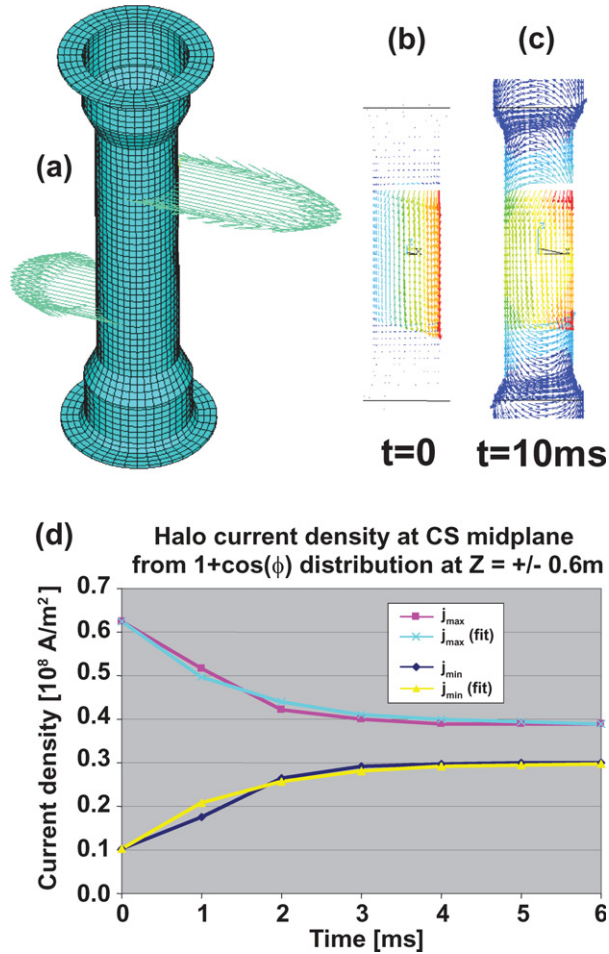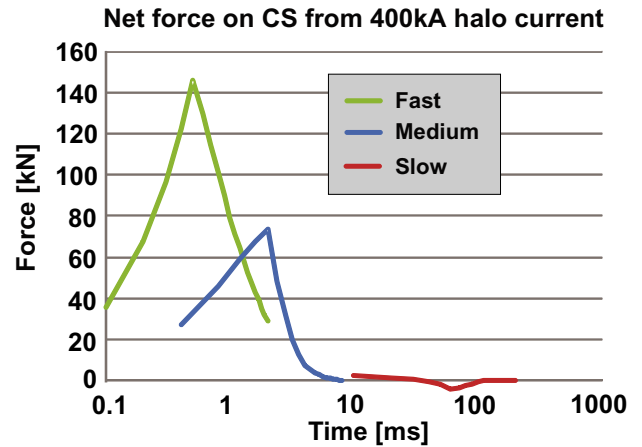
Figure 40. Net force on the CS from halo currents driven by fast, medium, and slow CQs for disruption scenario indices 11, 12 and 6, respectively, in table 4. Note the log scale used on the time axis.

Figure 39. (*a*) Distribution of current injected into CS casing to simulate halo current strike with toroidal peaking factor of 2, (*b*) (inductive) distribution of halo current on CS casing immediately following halo current strike, (*c*) (resistive) distribution of halo current 10 ms after halo strike and (*d*) halo current density at the CS midplane versus time after strike.

roughly half-way through the CQ, and then decreases to a small value near the end of the quench. Figure 40 shows the calculated net force on the CS for fast, medium, and slow CQs and the associated halo currents. As is evident from the figure, the fastest quenches have the highest forces, and is due to the fastest scenario having a quench time-scale (1 ms) faster than the time-scale for resistive redistribution (1.3 ms) of current through the CS casing. This results in increased toroidal peaking of the CS halo current which increases the lateral forces. The pedestal that supports the CS casing and other CS components is designed to withstand these lateral loads. However, the stresses and displacements (0.5–1 mm) of the bellows on the top of the machine are sufficiently large that a set of shims will be required to be installed to restrain the CS lateral motion while accommodating the vertical thermal expansion of the CS.

2.5. RWM stability

The ability to withstand disruptions of the highest performance plasmas of the Upgrade maintains a vital capability, namely the ability to access and study high beta plasmas at the highest

possible plasma temperature and lowest collisionality without risking machine integrity. As described in section 2.2.2, several structure enhancements are included of the Upgrade design to support high β operation at full field and current. As described in section 2.2.3, the 2nd NBI will introduce another large vessel penetration as shown in figure 20(*b*). Since this penetration will no longer have a metal port cover, the area of the conducting wall will be reduced, and this could adversely impact RWM stability [42] during operation above the no-wall stability limit. However, in NSTX, by design, the CuCrZr passive conducting plates provide much of the stabilization of the RWM. To assess the impact of the 2nd NBI port, the VALEN code [160] has been utilized to analyse $n = 1$ RWM stability for NSTX Upgrade. Figure 41(*a*) shows the VALEN model for the passive conducting structure of the Upgrade including both the present and 2nd NBI ports. Figure 41(*b*) shows the calculated $n = 1$ RWM growth rates as a function of β_N and number of NBI ports for a representative 2 MA equilibrium (equilibrium 'R' in figure 6) with $A = 1.7$, $\kappa = 2.6$, $\delta = 0.6$, $l_i = 0.6$, and $q_{min} = 1.9$. As is evident from figure 41(*b*), the addition of the 2nd NBI results in only a small β_N decrement of $\Delta\beta_N = -0.07$ from 5.79 to 5.72 indicating that the 2nd NBI port will have negligible impact on RWM stability limits in NSTX Upgrade.

The $n = 1$ kink with-wall stability limit shown in figure 41(*b*) is for an equilibrium using scaled pressure and parallel current density profiles taken from an MHD-stable NSTX experimental plasma (shot 1163136) operating at $\beta_N = 5.5$ above the no-wall limit and near the with-wall limit [65]. In using these profiles from NSTX for NSTX Upgrade free-boundary equilibrium calculations, the profiles have not been further optimized to increase stability limits. It should be noted that the NSTX Upgrade with-wall limit shown in figure 41(*b*) extrapolates to $\beta_N \approx 5.9$ in the absence of NBI port penetrations. This β_N value is approximately 15% lower than computed in the original NSTX RWM control system design using VALEN [161] (also ignoring port penetrations) for lower aspect ratio NSTX plasmas. Previous numerical studies have shown that both no-wall and with-wall stability limits are projected to decrease 10–20% as the aspect ratio is increased from $A = 1.45$ to $A = 1.7$ [51, 95]. Thus, the

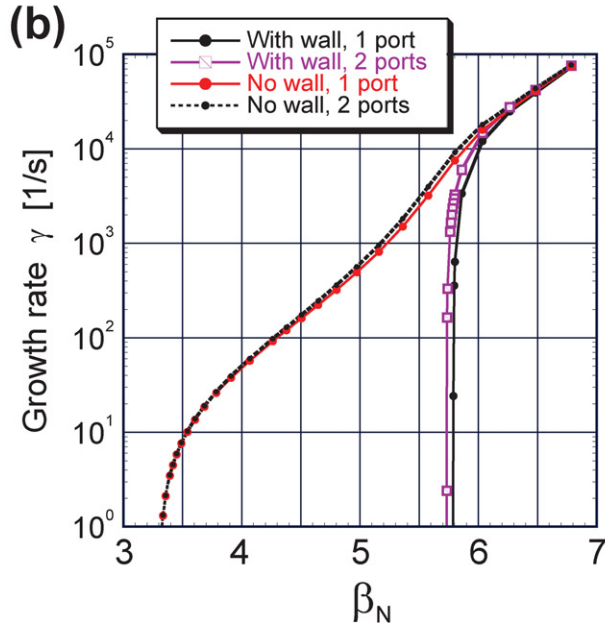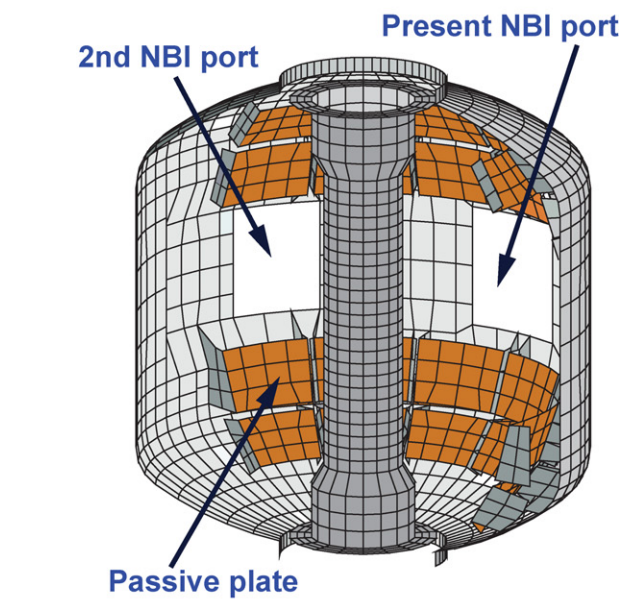## VALEN model of NSTX Upgrade passive conducting structure

(a)

(b)

Figure 41. (*a*) VALEN model of the NSTX Upgrade passive conductive structure including the vessel cut-outs for the present and 2nd NBI ports and (*b*) predicted $n = 1$ RWM growth rate versus β_N for one and two vessel penetrations for NBI ports.

decrease in kink stability limits from NSTX to NSTX Upgrade can be attributed in large part to increased aspect ratio.

2.6. Divertor power handling

2.6.1. Overview. While the compactness of the ST is beneficial for achieving high neutron wall loading for FNS, the ST divertor heat fluxes can also be high and challenge PFC power handling capabilities. The width of the heat-flux profile in the SOL is a critical parameter in projecting the peak divertor heat flux, since the peak heat flux varies inversely
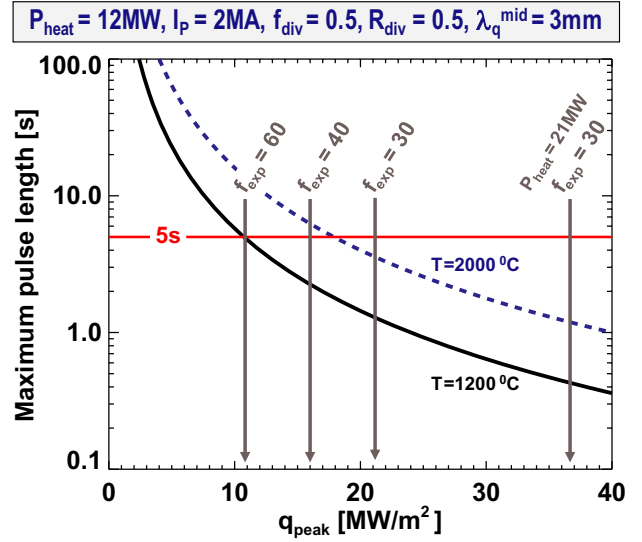
Figure 42. Projected NSTX Upgrade pulse-length limits versus peak divertor heat flux for two divertor carbon PFC temperature values.

with this width. Multi-machine databases and scalings exhibit a wide variation in predicted outboard midplane SOL heat-flux width λ_q and this variation represents a substantial uncertainty in projecting to future devices including ITER [162]. Recent dedicated multi-machine studies in the US [163–165] have explored the λ_q scaling further and find a strong inverse dependence on plasma current but a weak dependence on magnetic field and power into the SOL. Using this midplane heat-flux width parameter, the peak heat flux to the divertor target plate can be derived from power conservation and can be expressed as [166]:

$$Q_{\text{out}}^{\text{peak}} = \frac{P_{\text{heat}}^{\text{SOL}}(1 - f_{\text{rad}}) f_{\text{div}} \sin(\theta_{\text{plate}})}{2\pi R_{\text{strike}} f_{\text{exp}} \lambda_q}, \tag{3}$$

where $P_{\text{heat}}^{\text{SOL}}$ is the heating power to the SOL in the absence of radiative losses, f_{rad} is the assumed fraction of radiation, f_{div} is the fraction of SOL power to divertor leg in question, θ_{plate} is the poloidal angle of inclination between the divertor plate and divertor magnetic field lines, R_{strike} is the major radius of the divertor strike-point and f_{exp} is the poloidal flux expansion $= |\nabla\psi|_{\text{midplane}}/|\nabla\psi|_{\text{strike}}$.

Of particular importance for NSTX Upgrade are high current (2 MA) plasmas which are projected to have SOL heat-flux widths as narrow as 3 mm if the $\lambda_q \propto I_P^{-1.6}$ scaling observed in NSTX is also observed in NSTX Upgrade. As shown in figure 42, the peak heat flux must be limited to 10 MW m^{-2} to enable 5 s operation with the inertially/radiatively cooled ATJ graphite PFCs planned for the initial operation of NSTX Upgrade. Recent assessments of the divertor heat-flux scaling in NSTX project to peak divertor heat fluxes over 20 MW m^{-2} in the Upgrade even assuming high poloidal flux expansions of 30 [165]. As indicated in figure 42, utilizing upper/lower power splitting (i.e. $f_{\text{div}} = 0.5$) but not accounting for any radiation/detachment (i.e. $f_{\text{rad}} = 0.0$), divertor plate inclination (i.e. $\theta_{\text{plate}} = 90°$), or strike-point sweeping (i.e. R_{strike} is held constant at 0.5 m), poloidal flux expansions of 60 are required to achieve peak heat flux near

10 MW m^{-2} for P_{heat} = 12 MW in 2 MA plasmas. Increased radiation, inclination, or sweeping could reduce the required flux expansion or increase the allowable power or pulse length. Also, the λ_q scaling with plasma current is closer to $1/I_P$ in Alcator C-Mod [163] and DIII-D [164], so if a similar scaling was observed in NSTX Upgrade at high I_P, this would reduce the projected peak heat flux by a factor of 1.5 for 2 MA plasmas.

It is important to note that the analysis here focuses only on the outboard divertor leg, since previous NSTX experiments with LSN plasmas find an outboard to inboard power split ratio of approximately 3:1 [167] which is higher than observed at conventional aspect ratio (1.3:1) [168]. Further, measurements at both conventional [168] and low aspect ratio [167, 169, 170] indicate that the ratio of outboard to inboard peak heat flux is typically 3:1 to 4:1 for LSN discharges and up to 9:1 for DND low-A discharges [169, 170]. The low inboard peak heat flux in the NSTX is attributed to the inboard divertor leg typically being detached [171] while the outer leg can be either attached or (partially) detached [172, 173].

Retaining the divertor assumptions described above, i.e. f_{div} = 0.5, f_{rad} = 0.0, θ_{plate} = 90°, R_{strike} = 0.5 m, and λ_q = 0.9 cm/$I_P^{1.6}$ (MA), table 1 shows the projected peak heat flux and pulse duration allowed before reaching a divertor graphite PFC surface temperature of 1200 °C assuming that the total heating power is applied during the entire discharge (i.e. ramp-up and flat-top). This surface temperature limit is consistent with avoiding/minimizing self-sputtering and radiation-enhanced sublimation [174] for an estimated typical separatrix electron temperature $T_{e\text{-sep}}$ of 85 eV in NSTX Upgrade assuming the power into the SOL is increased up to a factor of three (6 MW to 19 MW), assuming $T_{e\text{-sep}} \propto P_{SOL}^{2/7}$ [166], and that the average $T_{e\text{-sep}}$ in NSTX is 60 eV [172, 175]. As is evident from table 1, the 100% non-inductive, long-pulse and high f_{BS} scenarios operating near 1 MA are projected to remain well below 1200 °C surface temperature using a flux expansion of 22 typical of high-triangularity double-null plasmas. In contrast, the max-I_P = 2 MA scenarios require high-flux expansions of 40–60 to achieve the respective scenario pulse-length goals while staying at or below the PFC surface temperature limit if no other heat-flux mitigation techniques are utilized. At the highest heating powers approaching 20 MW expected to be achievable in NSTX Upgrade (red columns in table 1), the pulse duration (ramp-up + flat-top) at full power could be as short as 1.3 s even if high flux expansion of 62 is utilized. Pulse durations much longer than this are not feasible for this scenario in any case, since as shown in figure 19, the NBI pulse duration for 15 MW total NBI power will be limited to 1.6 s.

Another important divertor issue is the effect of transient heat loads from ELMs [162, 176–180] and disruptions [181–185]. Recent high-speed IR camera measurements in NSTX during type-III ELM activity [186] in I_P = 0.8 MA, P_{NBI} = 4 MW plasmas find peak heat-flux values can transiently increase up to an order of magnitude. In these discharges, a low elongation κ = 1.8–2 shape with large strike-point radius R_{strike} = 0.7–0.8 m and low flux expansion = 2–6 was used to increase the peak heat flux to enable time-resolved measurements (0.16–0.63 ms time resolution) of divertor surface temperature and inferred heat flux during and between individual ELMs. During individual ELMs,

peak-heat flux values of 40–70 MW m^{-2} (occasionally up to 100 MW m^{-2}), e-folding lengths of 3–4 cm, and time-scale of 0.6 ms were observed compared with 4–6 MW m^{-2} peak heat flux and 1–1.5 cm e-folding length for the inter-ELM period. The ELM energy loss from the pedestal region corresponds to 3–5% of the total stored energy (W_{TOT} = 120 kJ) and causes divertor surface temperature increases of 50–150 °C near the outer strike-point. Since the peak inter-ELM heat flux could increase as much as a factor of 5–10 at higher I_P and heating power in NSTX Upgrade, and since the plasma stored energy is anticipated to increase to the MJ range, an increase in the flux expansion by an order of magnitude to 20–60 may be required to mitigate not only the inter-ELM heat flux, but also to limit the PFC surface temperature excursions during ELM events. Further analysis of the projected effects of ELMs and disruptions on NSTX Upgrade divertor operation (including possible lithium-based divertor systems [187, 188]) is a topic for future research.

2.6.2. Snowflake divertor. As discussed in section 2.6.1, high-flux expansion could play a critical role in the achievement of acceptable divertor heat fluxes during and between ELMs at high current and heating power in NSTX Upgrade. Very high-flux expansions of 40–60 have recently been demonstrated in NSTX utilizing a 'snowflake' [189] divertor as shown in figure 43(*a*). In order to support this and other future high-flux-expansion divertors such as the 'Super-X' [190] (possible with additional in-vessel PF coils not part of the present Upgrade), additional divertor PF coils have been incorporated into the Upgrade CS design as shown in figure 13. In particular, a third divertor PF coil (PF1C) will be added to the CS as shown in figure 43(*b*) to support the snowflake and to improve control of flux expansion and strike-point location generally.

The snowflake divertor does have the additional challenge of control of multiple nearby x-points, and the configuration may also be more sensitive to changes in the plasma profiles and/or boundary magnetic topology. For example, for the highest heat flux high-I_P = 2 MA scenarios of NSTX-U that will likely require long-pulse sustainment of the snowflake configuration, the time-evolving OH solenoid current will introduce a time-varying leakage flux in the divertor region. Figure 44(*a*) shows the snowflake poloidal flux contours in the divertor region for the reference snowflake configuration of figure 43(*b*) for three different OH solenoid current states, i.e. the minimum, zero, and maximum OH current utilizing all the divertor PF coils to produce the equilibrium. In this equilibrium calculation the strike-point and x-point locations, the inner and outer gap, and the boundary squareness can be held nearly fixed and the flux expansion is computed to vary less than 5% over the full range of OH currents.

To illustrate the effect of not utilizing all the divertor PF coils, figure 44(*b*) shows the same OH current scan without including the PF1BL coil (i.e. I_{PF1BL} = 0). For inductive operation with high I_P, I_{OH} will start positive and swing through zero to negative values at the end of the I_P flat-top as shown in figure 11. As seen in figure 44(*b*) for positive I_{OH}, the outer-most strike-point of the snowflake increases in major radius as the x-points approach each other forming a nearly pure snowflake configuration [189] (i.e. overlapping x-points).
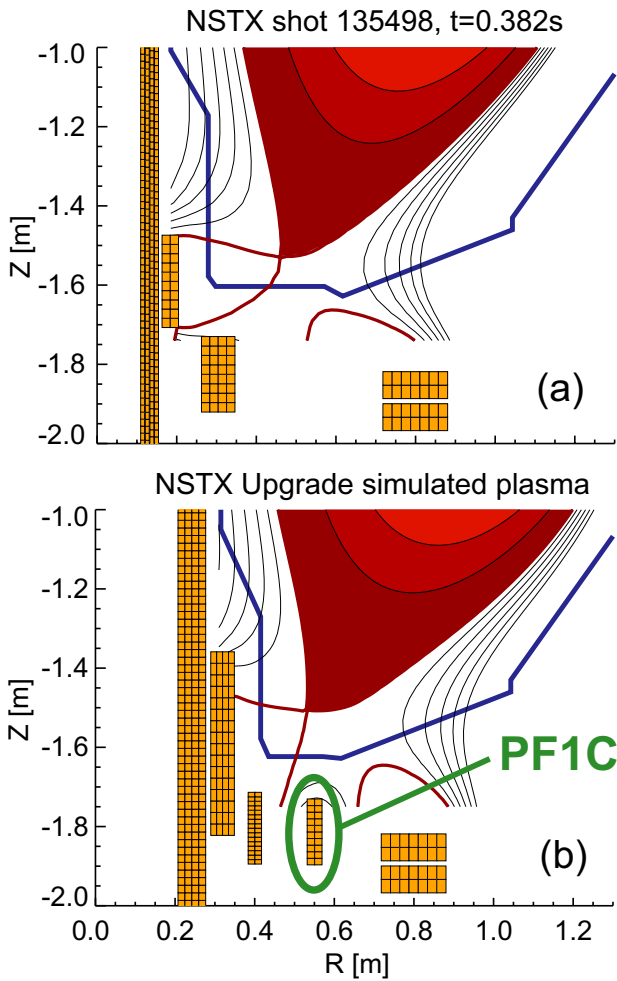
Figure 43. (*a*) Snowflake divertor in NSTX and (*b*) NSTX Upgrade.

Figure 44. (*a*) Overlay of boundaries in NSTX Upgrade as a function of ohmic heating solenoid current I_{OH} utilizing all divertor PF coils, (*b*) overlay of snowflake boundaries versus I_{OH} but with constraint of zero PF1B current.

This configuration reduces the wetted area for incident heat flux and has flux expansion 2–3 times lower than the reference configuration of figure 44(*a*). However, as the OH current passes through zero and becomes negative in the I_P flat-top, the reference snowflake configuration is largely recovered. Nevertheless, it is clear that having all three PF1A,B,C divertor coils is important for maintaining the snowflake configuration for a range of equilibrium states.

Importantly, the snowflake divertor (SFD) has recently demonstrated large (factor of 3 or more) reductions in peak heat flux and also up to a 50% reduction in carbon impurity production [191, 192]. Figure 45 shows an example of divertor heat-flux reduction using a snowflake divertor in a 0.9 MA flat-top plasma with $\kappa = 2.4$, $\beta_N = 4.5$, $\beta_T = 16\%$ and $P_{NBI} = 4$ MW [192]. The black curve in figure 45 shows the divertor heat flux prior to snowflake formation in a standard NSTX high-triangularity lower-single-null configuration with outboard strike-point radius near $R = 0.3$–0.35 m. At this time in the discharge, the peak heat flux is 4–7 MW m^{-2}. The transition from standard LSN divertor to SFD occurs between $t = 0.35$ s and 0.55 s, and the SFD was fully formed by $t = 0.60$–0.65 s. The red ($t = 0.57$ s) and blue ($t = 0.7$ s) curves in figure 45 show the divertor heat flux is reduced by a factor of 2–3 shortly after the SFD is fully formed. Analysis indicates that most of this heat-flux reduction is due
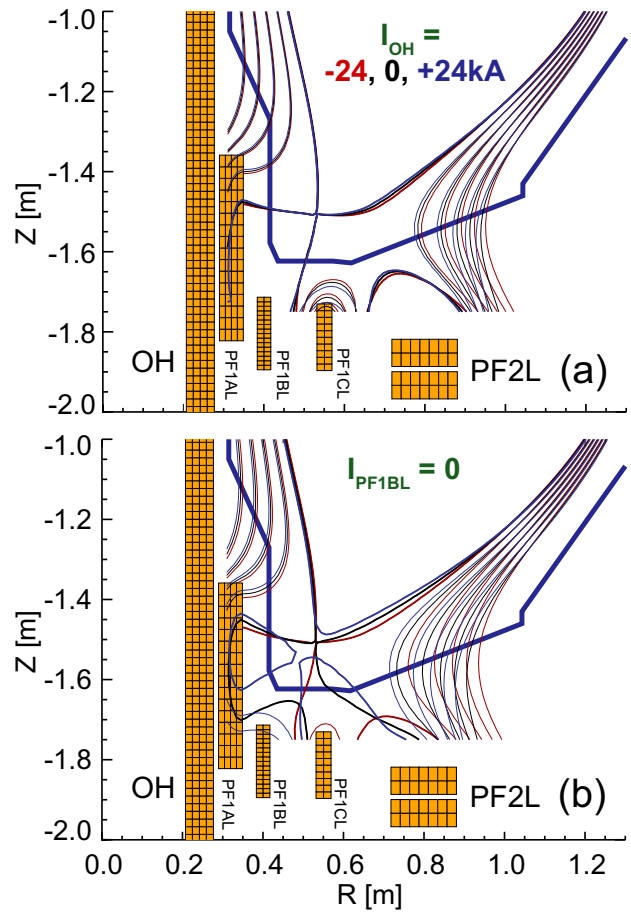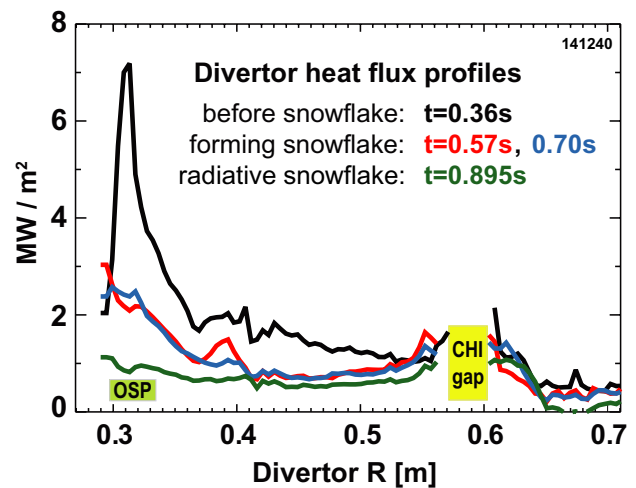

Figure 45. Peak heat flux in a standard divertor configuration in NSTX (black) compared with the snowflake divertor configuration (red and blue), and a partially detached 'radiative' snowflake (green) obtained at different times in the same discharge.

to increased wetted area from high-flux expansion of the SFD [192] rather than from strong changes in the SOL transport and/or radiation properties. At this time in the discharge, the SFD heat-flux profiles still exhibit some peaking in the

separatrix region near $R = 0.30$–0.35 m and in the low flux expansion region near $R = 0.55$–0.65 m. This variation of heat flux with flux expansion is consistent with previous results from NSTX [165] in which the peak divertor heat flux is found to vary inversely with flux expansion with only small changes in the up-stream SOL power width.

Still later in the discharge at $t = 0.895$ s, the green curve in figure 45 shows a further reduction in peak heat flux to values of 0.5–1 MW m^{-2}. At this time and beginning shortly after the formation of the SFD, the divertor radiated power is observed to increase, and spectroscopic measurements indicate that partial detachment is likely occurring after $t = 650$–700 ms and results from increased divertor radiation and cooling from intrinsic C impurities [192]. Increased divertor radiation and partial detachment [193] has been achieved previously in NSTX [172] for standard divertor configurations using either extrinsic D_2 or CD_4 puffing. Thus, the results of figure 45 indicate it is likely possible to combine the effects of increased wetted area (from increased flux expansion) and partial detachment (from either intrinsic or extrinsic impurities) to significantly reduce the peak divertor heat flux beyond what can be achieved with either method alone.

Overall, the snowflake divertor projects favourably to mitigating the stationary-plasma (and possibly ELM transient) high divertor heat fluxes in NSTX Upgrade and for supporting flat-top durations up to 5 s at a plasma current of 2 MA. Combining snowflake operation with a partially detached divertor appears particularly attractive, and would increase the heat-flux margin for operation at high current and power. Strike-point sweeping is another option that could provide additional heat-flux margin and is a topic for future analysis and research. Larger normalized strike-point radius (R_{strike}/R_0) and the effects of very large parallel connection length will also be extensively investigated in MAST Upgrade which is designed specifically to incorporate a cryo-pumped 'Super-X' divertor [190]. NSTX Upgrade (and MAST Upgrade) with increased current, field, and power will not only substantially extend and improve the understanding of the scaling of SOL heat-flux width with plasma parameters, but will also contribute to the development of novel means of mitigating high heat fluxes during both stationary and transient plasma conditions for FNSF and for Demo.

3. Summary

Scoping studies for a range of ST energy confinement assumptions have been performed for NSTX Upgrade with a goal of determining the performance requirements to achieve a factor of 3–6 reduction in collisionality, support tests of 100% non-inductive current ramp-up and sustainment, and assess confinement, stability, and heat-flux scaling and mitigation at increased magnetic field and plasma current while also providing sufficient flat-top duration for profile equilibration. The scoping studies indicate that a factor of two increase in plasma current, toroidal field, and NBI auxiliary heating power, a factor of 3 increase in ohmic solenoid flux, and a quintupling of the flat-top duration are sufficient to achieve the Upgrade goals. These performance objectives can be achieved with the combination of a new CS and a 2nd more tangentially injecting NBI. Importantly, the decrease in collisionality

accessible with these upgrades is projected to reduce the electron thermal diffusivity from micro-tearing modes, and doubling the toroidal field is projected to reduce the drive for GAE-induced transport by reducing $v_{\text{fast-ion}}/v_{\text{Alfvén}}$ towards 1 in lower density scenarios as shown in table 1. Variations such as these are expected to greatly aid the determination of the parametric dependencies and relative importance of the instabilities responsible for anomalous electron energy transport.

Systematic free-boundary equilibrium calculations have been performed to assess the PF coil current requirements to support the higher plasma current and access to high beta, and substantial engineering analysis and design has been performed for the structural reinforcements needed to handle the increased electromagnetic loads. In addition to the ex-vessel structural enhancements, the new CS incorporates numerous design improvements, including more robust flexible TF connections from the inner to outer TF legs, and a bottom-fed coaxial lead for the OH coil designed to substantially reduce the present NSTX $n = 1$ error field induced by an OH-TF electromagnetic interaction.

The 2nd neutral beam injector included in the Upgrade is designed to inject much more tangentially than the present NBI, and this injection geometry is predicted to increase the NBI CD efficiency by up to a factor of 2 enabling 100% non-inductive current drive at the 1 MA level and control of the core safety factor profile. Importantly, the 2nd NBI is also computed to have 2 times higher fast-ion confinement (due to reduced bad-orbit loss) at low plasma current as needed for non-inductive ramp-up studies. Also in support of non-inductive current ramp-up studies, the new CS incorporates additional PF coils in the divertor to increase coaxial helicity injection (CHI) injector flux by a factor of 2.5, increase the absorber coil current a factor or 3, and increase the absorber coil slew rate by a factor of 8. The higher TF and enhanced CS PF coil and CHI capability combined with the 2nd NBI are projected to be capable of non-inductive start-up of at least 300 kA and ramp-up to the 1 MA level. The more tangential NBI requires a significant modification to the NSTX vacuum vessel through the addition of a radially offset port cap. Further, the 2nd NBI requires considerable test-cell floor space and relocation of numerous diagnostics and associated racks and equipment.

Just as the equilibrium electromagnetic forces are expected to increase by up to a factor of four, disruption loads are anticipated to increase by a similar factor. The disruption forces from induced currents in the passive conducting plates are sufficiently high that additional plate re-enforcements at the plate attachment points are required. Halo current forces on the passive plates can also be withstood with the same plate attachment enhancements. If thicker plates are someday utilized to access $I_P > 2$ MA, the plate circulating current (but not the net toroidal current) is predicted to increase due to decreased plate resistance. However, despite the increased plate circulating current, it is expected that the plate displacement/deformation could be significantly reduced by the increased passive plate thickness. Halo currents on the centrestack would apply a lateral load that requires improved support structure on the bottom of the CS and shims at the top of the CS. With respect to the achievable beta in the Upgrade,

the structural enhancements support operation at high β_N up to 8 at full current and field at low l_i. The addition of a 2nd NBI port and associated reduction in conducting wall area is computed to produce only a small reduction on the ideal-wall limit.

Finally, the divertor heat-flux width is observed to scale inversely with plasma current in NSTX and could lead to very high heat fluxes in the NSTX Upgrade divertor at maximum current and heating power. The high-flux-expansion 'snowflake' divertor has demonstrated considerable heat-flux reduction in NSTX, and the incorporation of additional PF coils in the new CS enables operation with upper and lower snowflake divertors. Up/down power splitting using upper and lower snowflake divertors is projected to reduce the peak divertor heat flux to $10\,\mathrm{MW\,m}^{-2}$ and inertially maintain divertor tile temperature below sublimation damage limits for 5 s pulses at full current and high heating power. Divertor radiation/detachment and possibly strike-point sweeping are additional methods that could be utilized for mitigation of high heat flux.

In summary, the new capabilities of the NSTX Upgrade are anticipated to greatly enhance ST research in support of assessing the ST as a potential Fusion Nuclear Science Facility (FNSF). The NSTX Upgrade project is presently scheduled to be completed in 2014.

Acknowledgments

References

[1] Peng Y.-K.M. and Strickler D.J. 1986 *Nucl. Fusion* **26** 769
[2] Peng Y.-K.M., Galambos J.D. and Shipe P.C. 1992 *Fusion Technol.* **21** 1729
[3] Peng Y.-K.M. *et al* 2005 *Plasma Phys. Control. Fusion* **47** B263
[4] Peng Y.-K.M. *et al* 2009 *Fusion Sci. Technol.* **56** 957 www.new.ans.org/pubs/journals/fst/a_9034
[5] Kaye S.M. *et al* 1999 *Fusion Technol.* **36** 16 www.new.ans.org/pubs/journals/fst/a_88
[6] Ono M. *et al* 2000 *Nucl. Fusion* **40** 557
[7] Kaye S.M. *et al* 2007 *Nucl. Fusion* **47** 499
[8] Valovic M. *et al* 2009 *Nucl. Fusion* **49** 075016
[9] Valovic M. *et al* 2011 *Nucl. Fusion* **51** 073045
[10] Luce T.C., Petty C.C. and Cordey J.G. 2008 *Plasma Phys. Control. Fusion* **50** 043001
[11] ITER Physics Expert Groups on Confinement and Transport and Confinement Modelling and Database and ITER Physics Basis Editors 1999 *Nucl. Fusion* **39** 2175
[12] Doyle E.J. *et al* 2007 *Nucl. Fusion* **47** S18
[13] Petty C.C. *et al* 2004 *Phys. Plasmas* **11** 2514
[14] Mcdonald D.C. *et al* 2004 *Plasma Phys. Control. Fusion* **46** A215
[15] Takizuka T., Urano H., Takenaga H. and Oyama N. 2006 *Plasma Phys. Control. Fusion* **48** 799
[16] Kaye S.M. *et al* 2007 *Phys. Rev. Lett.* **98** 175002
[17] Mazzucato E. *et al* 2008 *Phys. Rev. Lett.* **101** 075001
[18] Mazzucato E. *et al* 2009 *Nucl. Fusion* **49** 055001
[19] Smith D.R. *et al* 2009 *Phys. Rev. Lett.* **102** 225005
[20] Yuh H.Y. *et al* 2011 *Phys. Rev. Lett.* **106** 055003
[21] Ren Y. *et al* 2011 *Phys. Rev. Lett.* **106** 165005
[22] Gorelenkov N. *et al* 2003 *Nucl. Fusion* **43** 228
[23] Stutman D. *et al* 2009 *Phys. Rev. Lett.* **102** 115002
[24] Gorelenkov N.N. *et al* 2010 *Nucl. Fusion* **50** 084012
[25] Wong K.L. *et al* 2007 *Phys. Rev. Lett.* **99** 135003
[26] Wong K.L. *et al* 2008 *Phys. Plasmas* **15** 056108
[27] Smith D.R., Guttenfelder W, LeBlanc B. and Mikkelsen D. 2011 *Plasma Phys. Control. Fusion* **53** 035013
[28] Guttenfelder W. *et al* 2011 *Phys. Rev. Lett.* **106** 155004
[29] Guttenfelder W. *et al* 2012 *Phys. Plasmas* **19** 022506
[30] Guttenfelder W. *et al* 2012 *Phys. Plasmas* **19** 056119
[31] Ren Y. *et al* 2012 *Phys. Plasmas* **19** 056125
[32] Joiner N., Applegate D., Cowley S.C., Dorland W. and Roach C.M. 2006 *Plasma Phys. Control. Fusion* **48** 685
[33] Joiner N., Hirose A. and Dorland W. 2010 *Phys. Plasmas* **17** 072104
[34] Jenko F., Dorland W. and Hammett G.W. 2001 *Phys. Plasmas* **8** 4096
[35] Kinsey J.E., Waltz R.E. and Candy J. 2005 *Phys. Plasmas* **12** 062302
[36] Kinsey J.E., Waltz R.E. and Candy J. 2007 *Phys. Plasmas* **14** 102306
[37] Waltz R.E. 2010 *Phys. Plasmas* **17** 072501
[38] Roach C.M. *et al* 2009 *Plasma Phys. Control. Fusion* **51** 124020
[39] Guttenfelder W. and Candy J. 2011 *Phys. Plasmas* **18** 022506
[40] Zhu W. *et al* 2006 *Phys. Rev. Lett.* **96** 225002
[41] Park J.K., Boozer A.H. and Menard J.E. 2009 *Phys. Rev. Lett.* **102** 065002
[42] Sabbagh S.A. *et al* 2010 *Nucl. Fusion* **50** 025020
[43] Berkery J.W. *et al* 2011 *Phys. Rev. Lett.* **106** 075004
[44] Menard J.E. *et al* 2010 *Nucl. Fusion* **50** 045008
[45] Gerhardt S.P. *et al* 2010 *Plasma Phys. Control. Fusion* **52** 104003
[46] Maingi R. *et al* 2011 *Nucl. Fusion* **51** 063036
[47] Sauter O., Angioni C. and Lin-Liu Y.R. 1999 *Phys. Plasmas* **6** 2834
[48] Troyon F., Gruber R., Saurenmann H., Semenzato S. and Succi S. 1984 *Plasma Phys. Control. Fusion* **26** 209
[49] Troyon F. and Gruber R. 1985 *Phys. Lett.* A **110** 29
[50] Strait E. 1994 *Phys. Plasmas* **1** 1415
[51] Menard J.E. *et al* 2004 *Phys. Plasmas* **11** 639
[52] Greenwald M. *et al* 1988 *Nucl. Fusion* **28** 2199
[53] Greenwald M. 2002 *Plasma Phys. Control. Fusion* **44** R27
[54] Goldston R.J., McCune D.C. and Towner H.H. 1981 *J. Comput. Phys.* **43** 61
[55] Gerhardt S.P., Andre R. and Menard J.E. 2011 Exploration of the equilibrium operating space for NSTX-Upgrade *Nucl. Fusion* submitted
[56] Gerhardt S.P. *et al* 2011 *Nucl. Fusion* **51** 073031
[57] Gruber O. *et al* 2001 *Nucl. Fusion* **41** 1369
[58] Ongena J. *et al* 2004 *Nucl. Fusion* **44** 124
[59] Gates D.A. *et al* 2006 *Phys. Plasmas* **13** 056122
[60] Stix T.H. 1972 *Plasma Phys.* **14** 367
[61] Medley S.S. *et al* 2004 *Nucl. Fusion* **44** 1158
[62] Start D.F.H., Cordey J.G. and Jones E.M. 1980 *Plasma Phys.* **22** 303
[63] Cordey J.G. 1984 *Plasma Phys. Control. Fusion* **26** 123
[64] Fisch N.J. 1987 *Rev. Mod. Phys.* **59** 175
[65] Menard J.E. *et al* 2006 *Phys. Rev. Lett.* **97** 095002
[66] Gerhardt S.P. *et al* 2011 *Nucl. Fusion* **51** 033004
[67] Bickerton R.J., Connor J.W. and Taylor J.B. 1971 *Nature Phys. Sci.* **229** 110
[68] Zarnstorff M.C. *et al* 1988 *Phys. Rev. Lett.* **60** 1306
[69] Wilson H.R. 1992 *Nucl. Fusion* **32** 257
[70] Kaye S.M. *et al* 2006 *Nucl. Fusion* **46** 848
[71] Kotschenreuther M. *et al* 2000 *Nucl. Fusion* **40** 677
[72] Hahm T.S. and Burrell K.H. 1995 *Phys. Plasmas* **2** 1648
[73] Waltz R.E. and Miller R.L. 1999 *Phys. Plasmas* **6** 4265
[74] Kaye S.M. *et al* 2009 *Nucl. Fusion* **49** 045010
[75] Peeters A.G., Angioni C. and Strintzi D. 2007 *Phys. Rev. Lett.* **98** 265003
[76] Mikkelsen D.R. 1989 *Phys. Fluids* B **1** 333

[77] Lloyd B. *et al* 1991 *Nucl. Fusion* **31** 2031
[78] Menard J.E. *et al* 2005 *Nucl. Fusion* **45** 539
[79] Gates D.A. *et al* 2006 *Nucl. Fusion* **46** S22
[80] Ejima S. *et al* 1982 *Nucl. Fusion* **22** 1313
[81] Menard J.E. *et al* 2001 *Nucl. Fusion* **41** 1197
[82] Wesley J *et al* 1991 *Proc. 13th Int. Conf. on Plasma Physics and Controlled Nuclear Fusion Research (Washington DC, 1990)* vol 3 (Vienna: IAEA) p 421
[83] Ramakrishnan S. *et al* 2011 Power system for NSTX Upgrade *Proc. of the 24th IEEE/NPSS Symp. on Fusion Engineering (Chicago, IL, 26–30 June 2011)* http://dx.doi.org/10.1109/SOFE.2011.6052347
[84] Ferron J.R. *et al* 1998 *Nucl. Fusion* **38** 1055
[85] Gates D.A. *et al* 2006 *Nucl. Fusion* **46** 17
[86] Humphreys D.A. *et al* 2009 *Nucl. Fusion* **49** 115003
[87] Kolemen E. *et al* 2010 *Nucl. Fusion* **50** 105010
[88] Kolemen E. *et al* 2011 *Nucl. Fusion* **51** 113024
[89] Laval G., Pellat R. and Soule J.S. 1974 *Phys. Fluids* **17** 835
[90] Haas F.A. 1975 *Nucl. Fusion* **15** 407
[91] Lazarus E.A., Lister J.B. and Neilson G.H. 1990 *Nucl. Fusion* **30** 111
[92] Ward D.J., Bondeson A. and Hofmann F. 1993 *Nucl. Fusion* **33** 821
[93] Ward D.J. and Hofmann F. 1994 *Nucl. Fusion* **34** 401
[94] Roberto M. 1992 *Nucl. Fusion* **32** 1666
[95] Menard J.E., Jardin S.C., Kaye S.M., Kessel C.E. and Manickam J. 1997 *Nucl. Fusion* **37** 595
[96] Angioni C. *et al* 2003 *Phys. Rev. Lett.* **90** 205003
[97] Angioni C. *et al* 2007 *Nucl. Fusion* **47** 1326
[98] Hirshman S.P. and Sigmar D.J. 1981 *Nucl. Fusion* **21** 1079
[99] Bell M.G. *et al* 2009 *Plasma Phys. Control. Fusion* **51** 124054
[100] Zhang H. *et al* 2011 *Fusion Sci. Technol.* **60** 664 www.new.ans.org/pubs/journals/fst/a_12460
[101] Zolfaghari A., Willard T. and Smith M. 2011 Coupled multiphysics analysis of the TF coil structure in the NSTX Upgrade *Proc. of the 24th IEEE/NPSS Symp. on Fusion Engineering (Chicago, IL, 26–30 June 2011)* pp 1–5
[102] Zolfaghari A., Titus P., Chrzanowski J., Salehzadeh A. and Dahlgren F. 2011 *Fusion Sci. Technol.* **60** 658 www.new.ans.org/pubs/journals/fst/a_12459
[103] Menard J.E. *et al* 2011 *Nucl. Fusion* **51** 103014
[104] Najmabadi F. and The ARIES Team 2003 *Fusion Eng. Des.* **65** 143
[105] Stevenson T. *et al* 2002 A neutral beam injector upgrade for NSTX *PPPL Report* 3651 www.pppl.gov/pub_report/2002/PPPL-3651.pdf
[106] Dahlgren F. *et al* 1993 TPX/TFTR neutral beam energy absorbers *Proc. 15th IEEE/NPSS Symp. on Fusion Engineering (Hyannis, MA, 11–15 October 1993)* vol 1, pp 455–61
[107] Tresemer K. *et al* 2011 *Fusion Sci. Technol.* **60** 303 www.new.ans.org/pubs/journals/fst/a_12370
[108] Stork D *et al* 2010 *Proc. 23rd Int. Conf. on Fusion Energy 2010 (Daejeon, Korea, 2010)* (Vienna: IAEA) CD-ROM file ICC/P5-06 and http://www-pub.iaea.org/mtcd/meetings/PDFplus/2010/cn180/cn180_papers/icc_p5-06.pdf
[109] Barrett T.R. *et al* 2011 *Fusion Eng. Des.* **86** 789
[110] Mikkelsen D.R. *et al* 1997 *Phys. Plasmas* **4** 3667
[111] Jardin S.C., Pomphrey N. and Delucia J. 1986 *J. Comput. Phys.* **66** 481
[112] Kessel C.E. *et al* 2006 *Phys. Plasmas* **13** 056108
[113] Fredrickson E.D. *et al* 2003 *Phys. Plasmas* **10** 2852
[114] Fredrickson E.D. *et al* 2006 *Phys. Plasmas* **13** 056109
[115] Maingi R. *et al* 2010 *Phys. Rev. Lett.* **105** 135004
[116] Houlberg W.A., Shaing K.C., Hirshman S.P. and Zarnstorff M.C. 1997 *Phys. Plasmas* **4** 3230
[117] Sabbagh S.A. *et al* 2006 *Nucl. Fusion* **46** 635
[118] Najmabadi F. and The ARIES Team 1998 *Fusion Eng. Des.* **41** 365
[119] Najmabadi F. *et al* 2006 *Fusion Eng. Des.* **80** 3

[120] Fujita T. *et al* 2001 *Phys. Rev. Lett.* **87** 085001
[121] Shiraiwa S. *et al* 2004 *Phys. Rev. Lett.* **92** 035001
[122] Yuh H.Y. *et al* 2009 *Phys. Plasmas* **16** 056120
[123] Taylor G. *et al* 2010 *Phys. Plasmas* **17** 056114
[124] Taylor G. *et al* 2011 HHFW heating and current drive studies of NSTX H-mode plasmas *PPPL Report* 4634
[125] Phillips C.K. *et al* 2009 *Nucl. Fusion* **49** 075015
[126] Hosea J. *et al* 2008 *Phys. Plasmas* **15** 056104
[127] Liu D. *et al* 2010 *Plasma Phys. Control. Fusion* **52** 025006
[128] Kugel H.W. *et al* 2009 *J. Nucl. Mater.* **390–391** 1000
[129] Canik J.M. *et al* 2010 *Phys. Rev. Lett.* **104** 045001
[130] Kugel H.W. *et al* 2009 *Fusion Eng. Des.* **84** 1125
[131] Ellis R. *et al* 2009 Mechanical design of the NSTX Liquid Lithium Divertor *Proc. of the 23rd IEEE/NPSS Symp. on Fusion Engineering (San Diego, CA, 1–5 June 2009)* pp 1–4 and http://www.pppl.gov/pub_report/2009/PPPL-4456.pdf
[132] Nygren R.E. *et al* 2009 *Fusion Eng. Des.* **84** 1438
[133] Allain J.P. and Brooks J.N. 2011 *Nucl. Fusion* **51** 023002
[134] Soukhanovskii V.A. *et al* 2007 High pressure supersonic gas jet fueling on NSTX *22nd IEEE Symp. on Fusion Engineering (Albuquerque, NM, 17–21 June 2007)* pp 1–4
[135] Sengoku S. *et al* 1985 *Nucl. Fusion* **25** 1475
[136] Kaufmann M. *et al* 1988 *Nucl. Fusion* **28** 827
[137] Ribeiro C. *et al* 2001 *Fusion Eng. Des.* **58–59** 319
[138] Baylor L. *et al* 2007 *Nucl. Fusion* **47** 1598
[139] Raman R. 2008 *Fusion Eng. Des.* **83** 1368
[140] Jarboe T.R. 1989 *Fusion Technol.* **15** 7
[141] Taylor G. *et al* 2012 *Phys. Plasmas* **19** 042501
[142] Taylor G. *et al* 2004 *Phys. Plasmas* **11** 4733
[143] Diem S.J. *et al* 2009 *Nucl. Fusion* **49** 095027
[144] Raman R. *et al* 2010 *Phys. Rev. Lett.* **104** 095003
[145] Nelson B.A. *et al* 2011 *Nucl. Fusion* **51** 063008
[146] Raman R. *et al* 2005 *Nucl. Fusion* **45** L15
[147] Tang X.Z. and Boozer A.H. 2005 *Phys. Plasmas* **12** 042113
[148] Raman R. *et al* 2007 *Phys. Plasmas* **14** 022504
[149] Raman R. *et al* 2010 *Phys. Rev. Lett.* **104** 1
[150] Raman R., Jardin S.C., Menard J. and Jarboe T.R. 2011 *Nucl. Fusion* **51** 113018
[151] Raman R. *et al* 2001 *Plasma Phys. Control. Fusion* **43** 305
[152] Raman R. *et al* 2001 *Nucl. Fusion* **41** 1081
[153] Nelson B. *et al* 1994 *Phys. Rev. Lett.* **72** 3666
[154] Nelson B.A. *et al* 1995 *Phys. Plasmas* **2** 2337
[155] Raman R. *et al* 2006 *Phys. Rev. Lett.* **97** 175002
[156] Jardin S., Bell M. and Pomphrey N. 1993 *Nucl. Fusion* **33** 371
[157] Gerhardt S.P., Menard J.E. and The NSTX Team 2009 *Nucl. Fusion* **49** 025005
[158] Titus P., Avasaralla S. and Hatcher R. 2011 *Fusion Eng. Des.* **86** 1784
[159] Gerhardt S.P. *et al* 2011 *Rev. Sci. Instrum.* **82** 103502
[160] Bialek J., Boozer A.H., Mauel M.E. and Navratil G.A. 2001 *Phys. Plasmas* **8** 2170
[161] Sabbagh S.A. *et al* 2004 *Nucl. Fusion* **44** 560
[162] Loarte A. *et al* 2007 *Nucl. Fusion* **47** S203
[163] Labombard B. *et al* 2011 *Phys. Plasmas* **18** 056104
[164] Lasnier C.J. *et al* 2011 *J. Nucl. Mater.* **415** S353
[165] Gray T.K. *et al* 2011 *J. Nucl. Mater.* **415** S360
[166] Stangeby P.C. 2000 *The Plasma Boundary of Magnetic Fusion Devices* (Bristol: Institute of Physics Publishing)
[167] Maingi R. *et al* 2003 *Nucl. Fusion* **43** 969
[168] Leonard A. *et al* 1995 *J. Nucl. Mater.* **220–222** 325
[169] Ahn J.-W. and Counsell G. 2001 *J. Nucl. Mater.* **290–293** 820
[170] Paul S., Maingi R., Soukhanovskii V., Kaye S. and Kugel H. 2005 *J. Nucl. Mater.* **337–339** 251
[171] Soukhanovskii V.A. *et al* 2005 *J. Nucl. Mater.* **337-339** 475
[172] Soukhanovskii V.A. *et al* 2009 *Nucl. Fusion* **49** 095025
[173] Soukhanovskii V.A. *et al* 2009 *Phys. Plasmas* **16** 022501
[174] Brooks J. 1990 *J. Nucl. Mater.* **170** 164
[175] Kelly F., Maingi R., Maqueda R., Menard J. and Paul S. 2009 *J. Nucl. Mater.* **390–391** 436

38

[176] Itami K. *et al* 1995 *J. Nucl. Mater.* **220–222** 203–7
[177] Leonard A.W. *et al* 1997 *J. Nucl. Mater.* **241–243** 628
[178] Leonard A. *et al* 1999 *J. Nucl. Mater.* **266–269** 109
[179] Herrmann A. *et al* 2003 *J. Nucl. Mater.* **313–316** 759
[180] Federici G., Loarte A. and Strohmayer G. 2003 *Plasma Phys. Control. Fusion* **45** 1523
[181] Riccardo V., Andrew P., Ingesson L.C. and Maddaluno G. 2002 *Plasma Phys. Control. Fusion* **44** 919
[182] Riccardo V., Loarte A. and Contributors T.J.E. 2005 *Nucl. Fusion* **45** 1427
[183] Hollmann E. *et al* 2005 *Nucl. Fusion* **45** 1046
[184] Granetz R. *et al* 2006 *Nucl. Fusion* **46** 1001
[185] Arnoux G., Loarte A., Riccardo V., Fundamenski W. and Huber A. 2009 *Nucl. Fusion* **49** 085038

[186] Ahn J.-W., Maingi R., Mastrovito D. and Roquemore A.L. 2010 *Rev. Sci. Instrum.* **81** 023501
[187] Abdou M. 2001 *Fusion Eng. Des.* **54** 181
[188] Sizyuk V. and Hassanein A. 2011 *J. Nucl. Mater.* **415** S881
[189] Ryutov D.D. 2007 *Phys. Plasmas* **14** 064502
[190] Valanju P.M., Kotschenreuther M., Mahajan S.M. and Canik J. 2009 *Phys. Plasmas* **16** 056110
[191] Soukhanovskii V.A. *et al* 2011 *Nucl. Fusion* **51** 012001
[192] Soukhanovskii V.A. *et al* 2011 The snowflake divertor: a game-changer for magnetic fusion devices? *38th EPS Conf. on Plasma Physics (Strasbourg, France)* (European Physical Society) Paper O3.109 and http://ocs.ciemat.es/EPS2011PAP/pdf/O3.109.pdf
[193] Petrie T. *et al* 1997 *Nucl. Fusion* **37** 321